THE DYNAMICS OF RINGED
SMALL BODIES

A Thesis Submitted by

Jeremy R. Wood

For the Award of
Doctor of Philosophy

2018

Abstract

In 2013, the startling discovery of a pair of rings around the Centaur 10199 Chariklo opened up a new subfield of astronomy - the study of ringed small bodies. Since that discovery, a ring has been discovered around the dwarf planet 136108 Haumea, and a re-examination of star occultation data for the Centaur 2060 Chiron showed it could have a ring structure of its own.

The reason why the discovery of rings around Chariklo or Chiron is rather shocking is because Centaurs frequently suffer close encounters with the giant planets in the Centaur region, and these close encounters can not only fatally destroy any rings around a Centaur but can also destroy the small body itself.

In this research, we determine the likelihood that any rings around Chariklo or Chiron could have formed before the body entered the Centaur region and survived up to the present day by avoiding ring-destroying close encounters with the giant planets. And in accordance with that, develop and then improve a scale to measure the severity of a close encounter between a ringed small body and a planet.

We determine the severity of a close encounter by finding the minimum distance obtained between the small body and the planet during the encounter, d_{min}, and comparing it to the critical distances of the Roche limit, tidal disruption distance, the Hill radius and "ring limit". The values of these critical distances comprise our close encounter severity scale.

The ring limit is defined as the close encounter distance between a planet and a ringed small body in a hyperbolic or parabolic orbit about the planet for which the effect on the ring is just noticeable in the three-body planar problem. The effect is considered just noticeable if the close encounter changes the orbital eccentricity of the orbit of any ring particle by 0.01. In the first version of our scale, the ring limit is set equal to a constant value of 10 tidal disruption distances for each planet, and the effect of the velocity at infinity, v_∞, of the orbit of the small body about the planet is ignored.

The method of backwards numerical integration of clones is used to determine the time intervals from now backwards in time within which Chariklo and Chiron have been injected into the Centaur region. The results show that Chariklo likely entered the Centaur region during the last 20 Myr and Chiron within the last 8.5 Myr from somewhere in the Trans-Neptunian region. We record d_{min} for all close encounters between each clone and each giant planet during these time intervals and use the severity scale to determine the likelihood that the close encounters could have destroyed any rings around each body during its time interval.

From this, it is seen that ring-destroying close encounters are so extremely rare that it is statistically likely that each body's rings could have originated outside the Centaur region assuming that the effects of viscous dispersion are negated by other stabilizing factors such as shepherd satellites and self-gravitating rings.

Furthermore, the results demonstrate that both Chariklo and Chiron have chaotic orbits but Chariklo's orbit exhibits a degree of stable chaos that Chiron's

does not. Their half-lifes are 3 Myr and 0.7 Myr respectively.

The accuracy of our close encounter severity scale is improved by finding the ring limits for simulated close encounters between hypothetical one-ringed small bodies and planets in the 3-body planar problem. The effects of planet mass, small body mass, v_∞, and ring orbital radius are fully accounted for.

When velocity effects are taken into account, we discover that the ring limit forms a curve in $d_{min} - v_\infty$ space, the ring limit has a lower bound of approximately 1.8 tidal disruption distances regardless of the small body mass or ring orbital radius, and that the ring limit equals this lower bound for parabolic orbits only.

Our data is then used to find an analytical solution for a ring limit upper bound curve for Chariklo-planet encounters. We present three different methods for using this curve. To test our results, The ring limits found from all three methods are compared to 27 previously published d_{min} values for Chariklo-planet encounters in the seven-body non-planar problem.

Only one d_{min} value is found to be greater than the ring limit and that all ring limits are within 4.4 tidal disruption distances for each planet. We conclude that these values are more accurate than the crude value of 10 tidal disruption distances used in the first version of our close encounter severity scale.

Future work is discussed and may include simulations of Chariklo, Chiron or Haumea in which the ring particles and possibly satellites are included.

This work is partitioned as follows: Chapter One introduces the topic and states the research questions; Chapters Two, Three and Four are the three papers either published or submitted for publication; and Chapter Five summarizes the overall conclusions.

Certification of Thesis

This Thesis is the work of Jeremy R. Wood except where otherwise acknowledged, with the majority of the authorship of the papers presented as a Thesis by Publication undertaken by the Student. The work is original and has not previously been submitted for any other award, except where acknowledged.

Principal Supervisor: Associate Professor Stephen C. Marsden

Associate Supervisor: Professor Jonathan Horner

Associate Supervisor: Dr. Tobias C. Hinse

Student and supervisors signatures of endorsement are held at the University.

List of Contributions from Publication Co-authors

- **Article I:** Wood, J., Horner, J., Hinse, T. C., and Marsden, S. C., (2017). "The Dynamical History of Chariklo and its Rings" Astronomical Journal, vol. 153, pp. 245- 252. (Top 15% journal; Impact Factor: 4.617 and SNIP: 1.32).
  DOI: https://doi.org/10.3847/1538-3881/aa6981

  The overall contribution of Jeremy Wood was 85% to the concept development, analysis, drafting and revising the final submission; Stephen C. Marsden, Jonathan Horner and Tobias C. Hinse contributed the other 15% to concept development, analysis, editing and providing important technical inputs.

- **Article II:** Wood, J., Horner, J., Hinse, T. C., and Marsden, S. C., (2018). "The Dynamical History of 2060 Chiron and its Proposed Ring System" Astronomical Journal, vol. 155, pp. 2 - 14. (Top 15% journal; Impact Factor: 4.617 and SNIP: 1.32).
  DOI: https://doi.org/10.3847/1538-3881/aa9930
  The overall contribution of Jeremy Wood was 85% to the concept development, analysis, drafting and revising the final submission; Stephen C. Marsden, Jonathan Horner and Tobias C. Hinse contributed the other 15% to concept development, analysis, editing and providing important technical inputs.

- **Article III:** Wood, J., Horner, J., Hinse, T. C., and Marsden, S. C., (2018). "Measuring the Severity of Close Encounters Between Ringed Small Bodies and Planets" has been submitted for publication in the Monthly Notices of the Royal Astronomical Society and is currently under review. (Top 19% journal; Impact Factor: 4.961 and SNIP: 1.08).
  DOI: TBA
  The overall contribution of Jeremy Wood was 94% to the concept development, analysis, drafting and revising the final submission; Stephen C. Marsden, Jonathan Horner and Tobias C. Hinse contributed the other 6% to concept development, analysis, editing and providing important technical inputs.

Acknowledgments

Table of Contents

List of Figures

(Excluding figures included in Chapters 3-5)

List of Tables

(Excluding tables included in Chapters 3-5)

1   Introduction

From antiquity, human beings have been looking upward at the heavens. The first humans saw the Sun and the Moon - two great lights - and stars that formed shapes in the sky. Every day and night these heavenly objects were seen to constantly move across the sky in an east to west motion relative to the horizon.

As this motion occurred, most stars maintained their position relative to other stars, but some stars were seen to wander – alternating between eastward and westward motion relative to other stars. These wanderers were not stars at all but planets.

But stars and planets were not the only objects our ancient ancestors observed. Occasionally these ancient people noticed strange fuzzy objects which appeared in the sky in places where no object had been seen before. They noticed that these surprise guests had tails and were larger than any star. Over time, these objects would fade from view. These were the first human sightings of comets – one type of small body in the Solar system.

In a sense, the science of small bodies of the Solar system began with the very first comet sighting. It would be millennia, however, before the exact nature of comets would be understood, and along the way other types of small bodies would be found.

1.1   A Brief Review of Cosmological Models

Humans had been observing the heavens for centuries before any attempt was made at explaining the motions observed. For example, we know that ancient Babylonians observed planets because of records found on clay tablets. As far as we know, the Babylonians had no model in which the planets orbited a central body.

A cosmological model explains heavenly motions and accurately predict future events. For example, a model could be used to predict the locations of planets on future dates. If the model is good then the planets will appear at the predicted locations on the future dates. If a model is bad then it can either be refined or discarded.

1.1.1   The Geocentric Model

It was the ancient Greeks who first tried to explain the motions they were seeing in the heavens. From the Greeks point of view, everything seemed to revolve around the Earth. Having no computers nor space probes nor even knowledge of gravity we can hardly blame the Greeks for inventing the erroneous geocentric or Earth-centered model.

In this model, Earth was the center of all revolution. To an ancient Greek, orbits did not exist as we know them today. Instead the Sun, Moon, planets and stars were attached to invisible crystalline spheres called deferents which constantly spun around the Earth. But this model proved to be too simplistic

and was unable to explain why planets changed their angular speed in the sky and occasionally drifted westward relative to the stars in loops and zig zags before resuming their more usual eastward motion.

Over the centuries different incarnations of the geocentric model were formulated in an attempt to align all heavenly motion with the model. In an attempt to explain why planets seemed to speed up and slow down in their motion against the stars, Earth was moved off-center of the invisible spheres which contained planets. This centered the motion on a point rather than on Earth, and the changing distance between Earth and the planet explained the change in speed. When the planet was closer to Earth it appeared to move faster in the sky and when farther away appeared to move more slowly. Though if you stood at the center of the planet's invisible sphere it would seem to maintain the same speed. Having Earth off-center was known as an eccentric. The stars had their own sphere centered on Earth since their motion relative to the horizon was uniform.

Greeks even devised a method to explain retrograde motion of planets while still maintaining spheres spinning in the same direction. They did this by placing the planet on a smaller spinning sphere the center of which was fixed to the rim of a constantly spinning much larger sphere. The larger sphere was called the deferent and the smaller sphere the epicycle.

The most successful geocentric model devised was the Ptolemaic model. In this model, the epicycles of Mercury and Venus were fixed to an Earth-Sun line, and the radii of the epicycles of the other planets were forced to remain parallel to it. The center of the motion was a point exactly off-center opposite of Earth and was called the equant.

1.1.2 The Copernican Model

The Ptolemaic model reigned as the accepted model of the universe until the 16th century when Polish astronomer Nicolaus Copernicus revived a little known ancient Greek model known as the heliocentric model. At that time, the heliocentric model was contrary to the teachings of the Church. Believing that Earth orbited the Sun could result in your imprisonment, torture, or even death. No wonder that Copernicus' model was only published just before his death in 1543.

In this model, Earth is replaced as the center of revolution with the Sun. Planets still resided on invisible spheres and still had epicycles though they were smaller than in the Ptolemaic model. Heavenly motions were still explained but in a different way.

The stars did not move at all but resided on a motionless invisible sphere of their own at a distance from the Sun beyond any planet. No forces were involved, and orbits as we know them today still did not exist. Copernicus was also able to determine the relative distance of each planet to the Sun compared to Earth's distance. Today we would refer to the Earth-Sun distance as an astronomical unit or au. The model is known today as the Copernican model.

1.1.3   The Keplerian Model

Through painstaking analysis of planetary positional data taken by Tycho Brahe, Johannes Kepler determined that the orbits of planets were not circles but were in fact ellipses. With the introduction of ellipses, epicycles were no longer necessary. Kepler's model was also heliocentric as the Copernican model had been, but Kepler abandoned the long-held notion that planets resided on invisible spheres. Instead he introduced for the first time in a cosmological model the idea that a force from the Sun was responsible for holding planets in their orbits. He believed this force was magnetic in nature.

Kepler's model could predict planetary positions as much as ten times better than the Ptolemaic model making it the best model up to that time. The properties of planetary orbits in Kepler's model are summarized in what today are called Kepler's three laws of motion released in 1609, 1609 and 1618.

1.1.4   Kepler's First Law

Kepler's first law states that the orbit of each planet is an ellipse with the Sun at one focus. Nothing is at the other focus (Bate et al., 1971; Zeilik, 2002; Bennett et al., 2016; Fraknoi et al., 2016).

An ellipse is the set of points in a plane such that the sum of the distances from each point to two fixed points is a constant. Each fixed point is called a focus. The major axis is a line which runs through both foci and connects the sides of the ellipse. The semi-major axis, a, is half the major axis.

The amount by which an ellipse differs from a circle is called the eccentricity, e, of the ellipse. A circle is a special case of an ellipse for which both foci are located at the same point. A circle has an eccentricity of zero. Given c is the distance from either focus to the geometrical center of the ellipse, the eccentricity is given by:

$$e = \frac{c}{a} \tag{1.1}$$

$0 \leq e < 1$ for any ellipse.

1.1.5   Kepler's Second Law

Kepler's second law states that a line drawn from a planet to the Sun sweeps out equal areas in equal times.

A consequence of this law is that a planet varies its angular speed as it orbits the Sun. A planet moves faster nearer the Sun and slower farther away from the Sun. Thus, at its point farthest from the Sun the planet is moving its slowest and at its point closest to the Sun the planet is moving its fastest. Only in a circular orbit will a planet maintain the same angular speed at all times (Bate et al., 1971; Zeilik, 2002; Bennett et al., 2016; Fraknoi et al., 2016).

Table 1.1: The modern semi-major axes of the orbits of the eight planets taken from NASA's Horizon ephemeris for January 1, 2000. Also shown are the orbital periods calculated using Kepler's 3rd Law and the observed values. Differences between these two are explained by rounding errors.

Planet	a_{modern} (au)	$P_{calculated}$ (years)	$P_{observed}$ (years)
Mercury	0.387098	0.240842	0.240851
Venus	0.723327	0.61518	0.615204
Earth	1.000372	1.000558	1.000597
Mars	1.523678	1.880788	1.880864
Jupiter	5.205109	11.875303	11.870117
Saturn	9.581452	29.65835	29.655306
Uranus	19.229945	84.327082	84.328634
Neptune	30.096971	165.114107	165.08904

1.1.6 Kepler's Third Law

Kepler's third law states that the square of the orbital period of the orbit of a planet, P, is directly proportional to the cube of the orbit's semi-major axis. The orbital period is the time it takes a planet to orbit the Sun one time (Bate et al., 1971; Zeilik, 2002; Bennett et al., 2016; Fraknoi et al., 2016). This law can be stated as

$$P^2 = ka^3 \tag{1.2}$$

Law 3 shows that the larger a planet's semi-major axis the longer it takes to orbit the Sun and the slower its average orbital speed. If P is in years and a is in astronomical units then $k = 1$ for all planets orbiting the Sun. Table 1.1 shows the modern semi-major axes of the orbits of the eight planets. Also shown are the orbital periods calculated using Kepler's 3rd Law and the observed values. The modern semi-major axes were taken from NASA's Horizon ephemeris service for Jan. 1, 2000[1].

1.1.7 The Universality of Kepler's Laws

Though Kepler originally developed his laws for planets orbiting the Sun, today we know that his laws can be applied to any elliptical orbit in the two-body problem for which the orbiting body has negligible mass compared to the primary body. Examples include moons orbiting planets, artificial satellites orbiting a planet, and small bodies orbiting the Sun (Bennett et al., 2016).

---

[1]http://ssd.jpl.nasa.gov/horizons.cgi?s body=1#top (accessed December 31, 2015)

1.1.8 Newton's Universal Law of Gravitation

A better understanding of the physics behind Kepler's laws arrived with the publication of Isaac Newton's Principia. In this work, Newton explains three laws of motion and a Universal Law of Gravitation. Today these four laws are part of what is known as Newtonian Mechanics.

In his book, Newton explains his Universal Law of Gravitation using these words: Every point mass in the universe attracts every other point mass in the universe with a force directly proportional to the product of the masses and inversely proportional to the square of the distance between the masses. This can be expressed as:

$$F = G_c \frac{m_1 m_2}{r^2} \tag{1.3}$$

(Zeilik, 2002; Bennett et al., 2016; Fraknoi et al., 2016) where F is the magnitude of the force on each of the two masses, G_c is the gravitational constant of the universe which is $6.673 \times 10^{-11} \frac{\text{Nm}^2}{\text{kg}^2}$ in SI units, m_1 and m_2 are the point masses, and r is the distance between the two point masses.

The Universal Law obeys Newton's third Law so that each mass feels the same force due to the other but in the opposite direction.

Newton's Universal Law can be used to find the constant k in equation 1.2. Consider the special case of a small body of mass m orbiting the much more massive Sun of mass M_{Sun} in a circular orbit of radius r.

In this case the centripetal force is supplied entirely by the gravitational force between the two masses. This equality is written as

$$m \frac{v^2}{r} = G_c \frac{m M_{sun}}{r^2} \tag{1.4}$$

Since the speed is constant, the velocity vector, $v = \frac{2\pi r}{P}$. This can be combined with Equation (1.4) to yield:

$$P^2 = \frac{4\pi^2}{G_c \left(m + M_{Sun} \right)} r^3 \tag{1.5}$$

For elliptical orbits the result is the same with r replaced with a.

1.1.9 Tidal Forces

A tidal force is the difference in gravitational force of one body on another across the body in question. The evaluation of a tidal force vector, $\vec{F}_{tf}$, at a point on a body equals the subtraction of two vectors: the gravitational force experienced by a point mass at the point in question, $\vec{F}$, and the gravitational force experienced by a point mass at the center of mass of the object, $\vec{F}_{cm}$. This is shown by

$$F_{tf} = \vec{F} - \vec{F}_{cm} \tag{1.6}$$

As one example of a tidal force calculation, consider a point mass m at radial distance r from the center of mass of the small body located at a point on a line between the center of mass of the small body and that of a planet of mass M_p. Assume the small body is not rotating and has no tensile strength. If the distance between the two centers of mass is d then Equation (1.6) is written as

$$F_{tf} = G_c \frac{m_p m}{\left(d - r\right)^2} - G_c \frac{m_p m}{d^2} = G_c m_p m \left[\frac{1}{\left(d - r\right)^2} - \frac{1}{d^2} \right] \qquad (1.7)$$

The Maclaurin expansion of $\dfrac{1}{\left(d-r\right)^2}$ is $\approx \frac{1}{d^2} + \frac{2r}{d^3}$. Substituting this into equation (1.7) yields an approximate form for the tidal force

$$F_{tf} \approx G_c m_p m \left[\frac{1}{d^2} + \frac{2r}{d^3} - \frac{1}{d^2} \right] = \frac{2 G_c m_p m r}{d^3} \qquad (1.8)$$

The tidal force of a planet on a small body can be strong enough to rip the small body apart. This was the fate of comet Shoemaker-Levy 9 in 1994 as it approached Jupiter and was torn into 21 separate pieces which then collided with the planet (e.g. Harris et al., 1994; Gough, 1994; Loders & Fegley, 1998; Jessup et al., 2000).

The distance between a small body held together by its own gravity and a planet within which the small body can be torn apart by tidal forces is called the Roche Limit. For simplicity, consider the case where the small body is a sphere; and the rotation of the small body and tidal force of the small body on the planet are negligible. When the small body is at the Roche limit distance from the planet ($d = R_{roche}$), the gravitational force of the small body on a point mass on the small body's surface just equals the tidal force due to the planet on this point mass. Using equation (1.8) to approximate the tidal force, this condition can be expressed as

$$\frac{2 G_c m_p m r}{R_{roche}^3} = \frac{G_c m_s m}{r^2} \qquad (1.9)$$

Solving for R_{roche} yields the Roche Limit equation

$$R_{roche} = r \left(\frac{2 m_p}{m_s} \right)^{\frac{1}{3}} \qquad (1.10)$$

Equation (1.10) can be rewritten using the densities of the small body and planet ρ_s and ρ_p respectively. Assuming spherical bodies, the result is

$$R_{roche} = R_{pl} \left(\frac{2 \rho_p}{\rho_s} \right)^{\frac{1}{3}} \qquad (1.11)$$

6

where R_{pl} is the physical radius of the planet. For the special case $\rho_s = \rho_p$ the Roche limit is about $1.26R_{pl}$. If the deformation of the small body is taken into account then the result for a tidally locked liquid small body orbiting the planet is (Murray & Dermott, 1999)

$$R_{roche} = 2.44R_{pl}\left(\frac{\rho_p}{\rho_s}\right)^{\frac{1}{3}} \tag{1.12}$$

1.2   The N-Body Problem

1.2.1   Overview of the N-Body Problem

The N-Body problem is the study of the dynamics of N interacting point masses. Only the 2-Body problem can be solved analytically for the general case (Murray & Dermott, 1999; Gurfil et al., 2016). The solution to the general case of the 3-Body and larger N-Body problems can only be approximated numerically using computer algorithms. The set of point masses under study is called a system.

The state of the n_{th} point mass, ψ_n, can be defined as the set of components of its position, $\vec{r}_n$, velocity, $\vec{v}_n$, and acceleration, $\vec{a}_{cn}$, vectors and a value for time, t. The combined states of all point masses which make up the system define the state of the system, Ψ.

$$\psi_n = \left[\vec{r}_{nx}, \vec{r}_{ny}, \vec{r}_{nz}, \vec{v}_{nx}, \vec{v}_{ny}, \vec{v}_{nz}, \vec{a}_{cnx}, \vec{a}_{cny}, \vec{a}_{cnz}, t\right] \tag{1.13}$$

$$\Psi = \left[\left[\vec{r}_{1x}, \vec{r}_{1y}, \vec{r}_{1z}, \vec{v}_{1x}, \vec{v}_{1y}, \vec{v}_{1z}, \vec{a}_{c1x}, \vec{a}_{c1y}, \vec{a}_{c1z}, t\right], ... \tag{1.14}$$

$$\left[\vec{r}_{Nx}, \vec{r}_{Ny}, \vec{r}_{Nz}, \vec{v}_{Nx}, \vec{v}_{Ny}, \vec{v}_{Nz}, \vec{a}_{cNx}, \vec{a}_{cNy}, \vec{a}_{cNz}, t\right]\right]$$

1.2.2   The Solar System N-body Problem

The dynamical behavior of the Solar system or part of the Solar system over some period of time can be approximated by considering only the gravitational forces among the members of the system. In this approximation, the effects of relativity and non-gravitational forces are ignored.

To find the net force acting on a single point mass at any moment in time, the net force acting on that mass due to the gravitational forces from all the other point masses must be calculated using

$$\vec{F}_i = \sum_{j=1}^{N-1} \vec{F}_{ij} \tag{1.15}$$

where $i \neq j$. $\vec{F}_i$ is the net force acting on the i_{th} mass, and $\vec{F}_{ij}$ is the gravitational force vector on m_i due to m_j. The magnitude of each $\vec{F}_{ij}$ is found from

equation (1.3). Once $\vec{F}_i$ is known, the acceleration of the i_{th} mass can be found using Newton's 2nd Law.

As a specific example, consider a system containing only two point masses m_i and m_j with position vectors $\vec{r}_i$ and $\vec{r}_j$ respectively. The displacement vector from m_i to m_j is $\vec{r}_{ij} = \vec{r}_j - \vec{r}_i$.

Newton's Universal Law can be rewritten in vector form to yield $\vec{F}_{ij}$. To do this, the concept of the unit vector can be employed. A unit vector of $\vec{r}_{ij}$ has a magnitude of 1 and points in the same direction as $\vec{r}_{ij}$. A unit vector of $\vec{r}_{ij}$ is defined as

$$\frac{\vec{r}_{ij}}{r_{ij}} = \frac{\vec{r}_j - \vec{r}_i}{r_{ij}} \tag{1.16}$$

multiplying the right side of equation (1.3) by this unit vector yields the vector form of Newton's Universal Law of Gravitation

$$\vec{F}_{ij} = G_c \frac{m_i m_j}{r_{ij}^3}\left(\vec{r}_j - \vec{r}_i\right) \tag{1.17}$$

where $\vec{F}_{ij}$ points from m_i towards m_j. The acceleration vector of the i_{th} mass due to the j_{th} mass, $\vec{a}_{cij}$, is found by solving Newton's 2nd Law for acceleration and applying it to the case of a force from Newton's Universal Law. The result is

$$\vec{a}_{cij} = \frac{\vec{F}_{ij}}{m_i} = G_c \frac{m_j}{r_{ij}^3}\left(\vec{r}_j - \vec{r}_i\right) \tag{1.18}$$

with the direction of $\vec{a}_{cij}$ being the same as that of $\vec{F}_{ij}$.

The total acceleration vector of the i_{th} mass, a_{ci}, can be found by adding all the $\vec{a}_{cij}$ vectors.

$$\vec{a}_{ci} = \sum_{j=1}^{N-1} \vec{a}_{cij} \tag{1.19}$$

with $i \neq j$.

The N-body problem can be simplified by placing certain restrictions on the movements and masses of the interacting point masses. For example, the orbits of all but one of the point masses may be restricted to be circles (the circular restricted problem) or a point mass may be taken to be so massive that its motion is negligible. Some members of the system may even have their masses set to zero. These are typically known as massless test particles.

1.2.3   The 2-Body Problem in the Solar System

In the 2-Body problem in the Solar system the mass of the Sun, M_{Sun}, can be assumed to be so large compared to the masses of other Solar system bodies that its motion is negligible. In the 2-Body problem, the equation of motion for
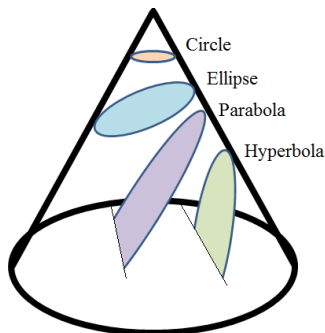
Figure 1.1: The conic sections formed by the intersection between a plane and the surface of a cone .

a body of mass m orbiting the Sun with position vector $\vec{r}$ from the location of the Sun is found by:

$$\vec{a}_c = \frac{d^2\vec{r}}{dt^2} = G_c \frac{M_{Sun}}{r^3}\vec{r} \tag{1.20}$$

The solution of this equation is actually a set of curves known as conic sections. These curves are known as: ellipse (including a circle), parabola and hyperbola. The conic sections are formed by the intersection between a plane and the surface of a cone.

If the plane is parallel to the base of the cone (has a slope of zero) then the intersection forms a circle. If the slope of the plane is between the slope of the cone and zero an ellipse is formed. If the slope of the plane matches the slope of the cone then the intersection forms a parabola. If the slope of the plane is greater than the slope of the cone then the intersection forms a hyperbola. Figure 1.1 shows how each curve is formed (Bate et al., 1971; Murray & Dermott, 1999; Gurfil et al., 2016).

The general solution for all the conic sections is

$$r = \frac{p}{1 + e\cos(\theta - \theta_o)} \tag{1.21}$$

where p is called the semi-latus rectum and e the eccentricity. θ_o is some reference angle formed by the intersection of the major axis and a reference line drawn from the Sun to some point on the curve. The angle $\theta_t = \theta - \theta_o$ is formed by the intersection of r with the major axis. Table 1.2 shows the form of p and the restrictions on e for each conic section.

In the case of an elliptical orbit the angle θ_t is known as the true anomaly. Figure 1.2 shows an example of the angles θ and θ_o for an elliptical orbit using an arbitrary reference line.

Though knowing θ_t does allow the position of the orbiting body to be determined, θ_t varies non-linearly in time. Another approach is to use a quantity which does vary linearly in time and relate that to the position of the body.

Table 1.2: The different conic sections with forms for p and restrictions on e for each curve. d_{min} is the distance of closest approach between the orbiting body and the Sun. A circle is just an ellipse with $e = 0$.

Conic Section	p	e
Ellipse	$a(1 - e^2)$	$0 \leq e < 1$
Parabola	$2d_{min}$	$e = 1$
Hyperbola	$a(1 - e^2)$	$e > 1$

This quantity is known as the Mean anomaly, M. It is directly proportional to the time since perihelion passage, Δt, and a constant of motion called the mean motion n_M defined as

$$n_M = \frac{2\pi}{P} \tag{1.22}$$

n_M is the constant angular speed the orbiting body would have if the orbit was a circle. M is related to n_M and the time since perihelion passage by

$$M = n_M \Delta t \tag{1.23}$$

If the orbit is a circle then M is simply the true anomaly. However, for elliptical orbits, M has no simple geometrical definition but can be related to another angle known as the eccentric anomaly, E. The eccentric anomaly is defined using an elliptical orbit circumscribed in a circle of radius a.

An example is shown in Figure 1.2. The eccentric anomaly is formed by the intersection of the major axis and a radial line of the circumscribing circle which passes through a point on the circumscribing circle which has the same horizontal (x) coordinate and same sign as the vertical (y) coordinate as that of the position vector of the orbiting mass.

The eccentric anomaly is related to the mean anomaly via Kepler's equation

$$E = M + e\sin E \tag{1.24}$$

(Murray & Dermott, 1999; Gurfil et al., 2016)

The orbit of a body in an elliptical orbit about the Sun is completely defined using six quantities known as the osculating orbital parameters which are derived from the 3D position and velocity components of the body in orbit. These are:

- $a =$ the semi-major axis

- $e =$ the eccentricity

- $i =$ the inclination, the angle between the plane of the orbit and some reference plane (often the plane of Earth's orbit about the Sun called the ecliptic plane). Values of i lie in the range $0° \leq i \leq 180°$. If $i > 90°$ the orbit is said to be retrograde.
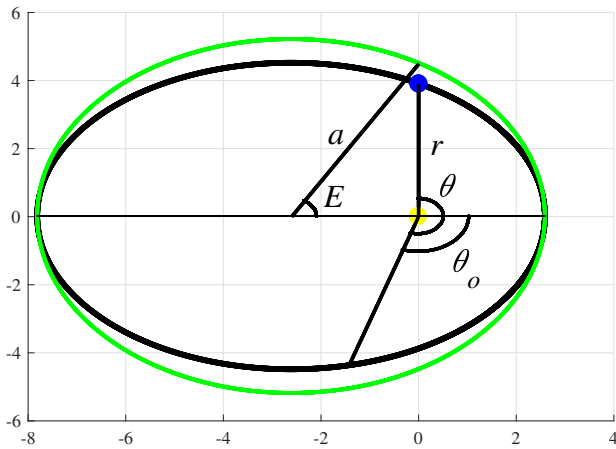
Figure 1.2: An elliptical orbit of a body orbiting the Sun. θ_o is some reference angle formed by the intersection between a reference line drawn from the Sun to some point on the ellipse and the major axis. The angle θ is formed by the intersection between the position vector, r, of the body and the reference line. In the case of an ellipse the angle $\theta_t = \theta - \theta_o$ is known as the true anomaly. Shown in green is a circumscribing circle of radius equal to the semi-major axis of the ellipse, a. The eccentric anomaly, E, for the orbiting body is formed by the intersection between a line drawn from the center of the ellipse to the Sun and a line drawn from the center of the ellipse to a point on the circumscribing circle which has the same horizontal coordinate as the orbiting body. This angle will vary in time as the body orbits the Sun.

- Ω = the longitude of ascending node, an angle in a reference plane measured between some reference line passing through the Sun and a line from the Sun to the point of ascending node, a point where the orbit intersects the reference plane and the body is moving above the reference plane.

- ω = the argument of perihelion, an angle in the plane of the ellipse between a line drawn from the point of perihelion to the Sun and a line drawn from the Sun to the point of ascending node

- M = the Mean anomaly

Often, the argument of perihelion is replaced by another quantity called the longitude of perihelion, $\overline{\omega}$, which is the sum of the longitude of ascending node and the argument of perihelion.

$$\overline{\omega} = \Omega + \omega \qquad (1.25)$$

(Bate et al., 1971; Murray & Dermott, 1999; Gurfil et al., 2016). The eccentric or true anomaly could also be used in place of M. Figure 1.3 shows the longitude of ascending node and the argument of perihelion for the case of a hypothetical planet orbiting the Sun[2]. One other quantity of elliptical motion about the Sun is the mean longitude, λ, defined as the sum of the Mean Anomaly and longitude of perihelion

$$\lambda = M + \overline{\omega} \qquad (1.26)$$

(Murray & Dermott, 1999; Gurfil et al., 2016). The energy of an elliptical orbit for a body of mass m orbiting the Sun is given by

$$E_{ellip} = \frac{-G_c}{2a}\left(m + M_{Sun}\right) \qquad (1.27)$$

(Wie, 1998; Murray & Dermott, 1999).

1.2.4 The Circular Restricted 3-Body Problem

In the circular restricted 3-body problem, the 3-body problem is simplified by forcing two of the bodies m_1 and m_2 to orbit their common center of mass in circular orbits (Marquis, 1799; Poincaré, 1902). The motion of the third body is not restricted. Its mass is considered negligible and so does not affect the orbits of the other two masses.

Consider the case where m_1 and m_2 are a planet and the Sun. In this case the Sun's motion can be ignored. Though the motion of the 3rd body cannot be solved analytically, there are constants of motion.

It is convenient to study the motion of the third body of mass m in the rotating frame of the orbiting planet. In this frame the planet is taken to be at

---

[2]https://en.wikipedia.org/wiki/Orbital_elements (accessed February 10, 2018)
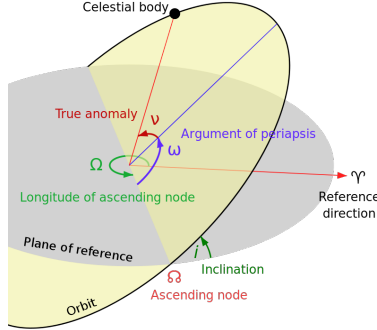
Figure 1.3: The orbit of a planet around the Sun is shown. The gray region is a reference plane. The planet intersects the plane while moving above it at the point of ascending node. The longitude of ascending node, Ω is in the reference plane and is relative to some reference direction. The argument of perihelion, ω, is in the plane of the orbit.

rest while the 3rd body moves due to the gravitational forces of the planet and the Sun; Coriolis force, and Centrifugal force.

The Coriolis force is a deflecting force perpendicular to the velocity of the 3rd body in the rotating frame. It is given by

$$F_{Cor} = -2m\vec{n}_M \times \vec{v}_{rot} \tag{1.28}$$

Here, the vector $\vec{n}_M$ is the angular velocity vector of the planet in its orbit about the Sun which is perpendicular to the planet's orbital plane. Its magnitude is equal to the mean motion. $\vec{v}_{rot}$ is the velocity of the 3rd body in the rotating frame of the planet. The centrifugal force is a force directed radially outward from the center of the planet's orbit. It is given by

$$F_{cent} = mn_M^2 r \tag{1.29}$$

Given a 2D rectangular coordinate system, the following quantity is constant

$$C_J = n_M^2 r^2 + G_c\left(\frac{m_1}{r_1} + \frac{m_2}{r_2}\right) - v_{rot}^2 \tag{1.30}$$

and is known as the Jacobi constant. The units are chosen so that the distance between the Sun and planet is a constant 1 and $G_c(m_1 + m_2) = 1$. v_{rot} is the velocity of the third body in the rotating frame, and r is the magnitude of the position vector of the 3rd body.

The Jacobi constant can be rewritten in terms of osculating orbital quantities. Assuming the orbital eccentricity of the planet is zero, in this form it is called the Tisserand Relation and is given by

$$T_p = \frac{a_p}{a} + 2\cos(i - i_p)\sqrt{\frac{a}{a_p}\left(1 - e^2\right)} \tag{1.31}$$

Here, i and e are the inclination and eccentricity of the small body's elliptical orbit respectively, a_p is the semi-major axis of the planet's elliptical orbit, and i_p the inclination of the planet's elliptical orbit (e.g. Levison, 1996; Murray & Dermott, 1999; Bailey & Malhotra, 2009).

The Tisserand parameter can be used to indicate the severity of potential encounters between the planet and the small body. If $T_P > 3$, then the orbits are non-crossing. In this case, the small body is wholly interior to, or exterior to, the planet's orbit. If $T_P < \sim 2.8$, then the encounter velocity is high enough that the close encounter won't eject the small body from the Solar system in one encounter; but if T_P is in the range $\sim 2.8 < T_P < \sim 3.0$ then the encounter velocity is slow enough so that the small body could be ejected from the Solar system in a single pass. (Levison & Duncan, 1997; Horner et al., 2003).

In the rotating frame there exists five points in the plane of the planet's orbit at which the 3rd body would feel no forces if $v_{rot} = 0$ (or in other words the body would be motionless in the rotating frame of the planet). These points are known as the Lagrangian Equilibrium Points and are shown in Figure 1.4 [3]. Three of the points lie on a line which passes through the Sun and planet. These are the collinear Lagrangian points and are called L_1, L_2 and L_3. L_1 lies in between the planet and the Sun. L_2 lies outside the orbit of the planet and L_3 lies on the opposite side of the Sun as the planet.

The other two are called triangular Lagrangian Equilibrium points and lie at points on the planet's orbit at $60°$ ahead and $60°$ behind the orbiting planet. The leading point is called L_4, and the trailing point L_5 (Murray & Dermott, 1999; Gurfil et al., 2016). A body of negligible mass at any Lagrange point with $v_{rot} = 0$ will have the same mean motion, n_M, as the planet.

The distance between the planet and L_2 approximately defines the radius of a sphere centered on the planet within which the planet's gravity dominates over the Sun's. This sphere is known as the Hill Sphere (Murray & Dermott, 1999; Gurfil et al., 2016). All known satellites of the planets orbit within their planet's respective Hill Sphere. An equation for the radius of the Hill Sphere (or the Hill Radius), R_H, can be derived using the first condition of equilibrium on an object of mass m at L_2 motionless in the rotating frame of the planet.

Let the radius of the planet's orbit be r_p, and the mass of the planet M_p. Since the planet moves in a circular orbit in the lab frame, the centripetal force is supplied by the force of gravity from the Sun. This can be expressed as:

$$\frac{m_p v_p^2}{r_p} = G_c \frac{m_p M_{Sun}}{r_p^2} \tag{1.32}$$

where v_p is the magnitude of the velocity of the planet. Canceling M_p yields

---

[3]https://en.wikipedia.org/wiki/Lagrangian_point (accessed February 8, 2018)

$$\frac{v_p^2}{r_p} = G_c \frac{M_{Sun}}{r_p^2} \tag{1.33}$$

For a circular orbit, v_p is constant and is given by $v_p = n_M r_p$. Substituting in for v_p yields

$$\frac{n_M^2 r_p^2}{r_p} = G_c \frac{M_{Sun}}{r_p^2} \tag{1.34}$$

Which can be solved for the squared mean motion. The result is

$$n_M^2 = G_c \frac{M_{Sun}}{r_p^3} \tag{1.35}$$

Let $\vec{F}_{Sun}$ be the force of gravity of the Sun on the mass m, $\vec{F}_p$ the force of gravity of the planet on the mass m and $\vec{F}_{cent}$ the centrifugal force on the mass m in the rotating frame of the planet. The equation for the first condition of equilibrium for the mass m is then written as

$$\vec{F}_{cent} + \vec{F}_{Sun} + \vec{F}_p = 0 \tag{1.36}$$

$$mn_M^2 \left(r_p + R_H \right) - G_c \frac{mM_{Sun}}{\left(r_p + R_H \right)^2} - G_c \frac{mm_p}{R_H^2} = 0 \tag{1.37}$$

Solving for R_H yields

$$R_H = r_p \left(\frac{M_p}{3M_{Sun}} \right)^{\frac{1}{3}} \tag{1.38}$$

(Hill, 1878). For elliptical orbits with low eccentricity, r_p is approximately the semi-major axis of the planet's orbit, a_p. Replacing r_p with a_p yields

$$R_H = a_p \left(\frac{M_p}{3M_{Sun}} \right)^{\frac{1}{3}} \tag{1.39}$$

Analogously, the Hill Sphere around a small body of mass m_s relative to a planet of mass M_p can be found. This form of the Hill Radius equation is applicable to satellites of planets and small bodies orbiting the Sun having close encounters with planets. The result is

$$R_H = r_s \left(\frac{m_s}{3m_p} \right)^{\frac{1}{3}} \tag{1.40}$$

where r_s is the radius of the circular orbit of the small body about the planet. Equation (1.40) can be used to find the distance, R_{td}, between a small body

15
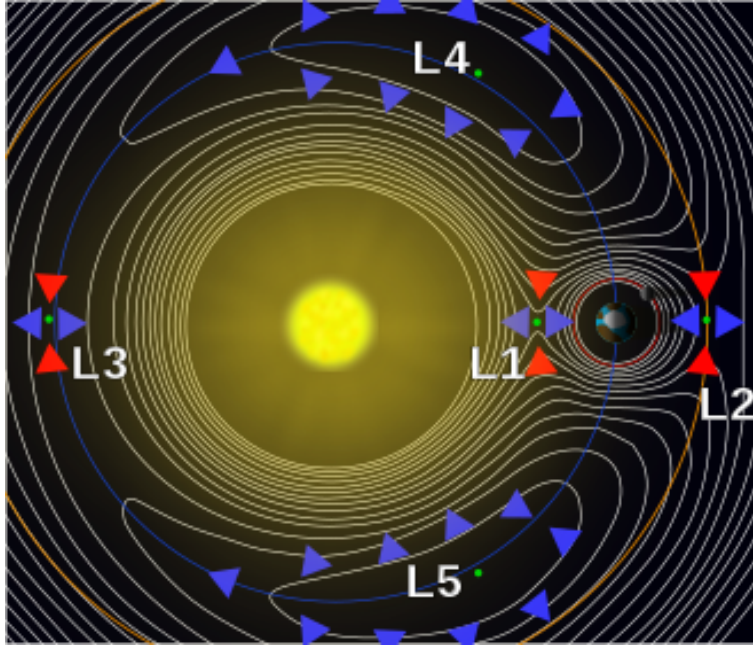
Figure 1.4: The five Lagrange points for a planet in orbit about the Sun in a circular orbit. The Hill sphere around the planet is shown and has a radius R_H. Zero-velocity curves are also shown.

and a planet at which the orbit of a satellite of negligible mass about m_s can be broken apart by tidal forces. Let the orbit of a satellite of negligible mass about m_s be a circle of radius, r. In this case, when the distance between the planet and m_s equals R_{td}, the orbit of the satellite lies just on the rim of the Hill Sphere of m_s relative to the planet. This condition can be expressed as

$$R_H = r = R_{td}\left(\frac{m_s}{3m_p}\right)^{\frac{1}{3}} \tag{1.41}$$

This equation can then be solved for R_{td} to yield:

$$R_{td} = r\left(\frac{3m_p}{m_s}\right)^{\frac{1}{3}} \tag{1.42}$$

R_{td} is known as the tidal disruption distance (Philpott et al., 2010).

1.3   Resonances

In a general sense, two orbits are in resonance with each other when certain orbital parameters exist in or nearly in a ratio of two small integers (or are

16

commensurate with each other). However, this simplistic definition does not define what is meant by "nearly in". A more exact definition is that two orbits in the Solar system are in resonance when at least one angle equal to some linear sum of the mean longitudes of the two bodies, the longitudes of ascending node and longitudes of perihelion, librates in time. Such angles are known as resonance angles. In this section, whenever it is stated that two orbits or two bodies are in resonance with each other when certain orbital parameters are commensurate, it will be understood that the requirement of the more exact definition is also met.

Resonances exist throughout the Solar system and are responsible for various phenomena such as the transport of meteoritic material to Earth (Wisdom, 1982); capture of small bodies during planetary migration (Gomes et al., 2005); and the creation of gaps in the main asteroid belt and Saturn's rings (e.g. Murray & Dermott, 1999; French et al., 2016).

They are very important in the study of both the short and long term dynamical behavior of small bodies. Resonances can stabilize or destabilize small body orbits and affect their dynamical lifetimes.

1.3.1 Mean Motion Resonances

In the 3-body problem (Sun, planet, small body), the orbital parameters of the small body vary over time due to the gravitational perturbations of the planet. If the orbital periods of the planet and small body are commensurate then this is a special condition known as a mean motion resonance (e.g. Murray & Dermott, 1999; Roig et al., 2002; Guzzo, 2006; Ryden , 2016) or MMR.

When this occurs, the conjunctions of the bodies regularly occur at the same positions in their orbits. This leads to regular gravitational tugs on the small body at the same location in its orbit. The situation is similar to a swinging pendulum that is pushed every at every other amplitude.

Mean motion resonances can also occur between planets. For example, the planet Neptune has an orbital period of 164.8 years, and the planet Uranus has an orbital period of 84.0 years. Taking the ratio of these two periods yields

$$\frac{164.8}{84.0} \approx \frac{2}{1} \tag{1.43}$$

So Neptune is said to be nearly in a 2 to 1 mean motion resonance with Uranus. Similarly, Uranus and Saturn are nearly in a three to one resonance and Saturn and Jupiter are nearly in a five to two resonance. For this work, mean motion resonances that lie outside a planet's semi-major axis will be listed with the smaller integer first and called exterior mean motion resonances. Mean motion resonances (or MMR) that lie inside a planet's semi-major axis will be listed with the larger integer first and called interior mean motion resonances. For example, the 1 to 2 mean motion resonance of Neptune lies outside Neptune's orbit, but its 2 to 1 MMR lies within its orbit.

Given integers j_1 and j_2, the notation $j_2 : j_1$ can be used to describe interior MMR when $j_2 > j_1$ and exterior MMR when $j_2 < j_1$. The special case of

$j_2 = j_1$ will be discussed later. Using this notation, 2:1 represents an interior MMR and 1:2 represents an exterior MMR. For a given MMR of a planet, the strength of the resonance is related to the order of the resonance, q_q, given by $q_q = |j_2 - j_1|$ (e.g. Gallardo, 2006). Resonances are generally referred to as first order, second order and so on. Generally speaking, given all other factors being equal, a lower order resonance is stronger than a higher order resonance. For example, a 3 to 2 resonance would be a first order resonance since $3 - 2 = 1$.

The location of mean motion resonances can be found using Newton's form of Kepler's 3rd Law. Given a planet of mass M_p and a small body of negligible mass m orbiting the Sun with orbital periods P_1 and P_2 and semi-major axes a_p and a_{MMR} respectively. If the two bodies are in a mean motion resonance with each other then the integer ratio of the orbital periods can be expressed as

$$\frac{P_1}{P_2} = \frac{j_1}{j_2} \tag{1.44}$$

In the realm where $M_{Sun} \gg M_p$, using Newton's form of Kepler's third law this becomes

$$P^2 = \frac{4\pi^2}{G_c M_{Sun}} a^3 \tag{1.45}$$

squaring the integer ratio in equation (1.44) and setting that equal to the ratio of the square orbital periods expressed using equation (1.45) yields

$$\left(\frac{j_1}{j_2}\right)^2 = \frac{4\pi^2}{G_c M_{Sun}} \frac{G_c M_{Sun}}{4\pi^2} \frac{a_p^3}{a_{MMR}^3} \tag{1.46}$$

$$\left(\frac{j_1}{j_2}\right)^2 = \frac{a_p^3}{a_{MMR}^3} \tag{1.47}$$

which can be solved for a_{MMR}. The result is

$$a_{MMR} = a_p \left(\frac{j_2}{j_1}\right)^{(2/3)} \tag{1.48}$$

While in the mean motion resonance, the osculating orbital elements of the small body's orbit tend to oscillate quasi-periodically in time. As an example, Moons & Morbidelli (1995) found that the semi-major axis, eccentricity and inclination of the orbits of small bodies in the 4:1, 3:1, 5:2, and 7:3 interior MMRs of Jupiter often oscillated quasi-periodically with periods on time scales of 10^3 years.

The vector $\vec{r}_{ij}$ is a displacement vector between the small body and Jupiter. The perturbing force of gravity of Jupiter on the small body is related to r_{ij} via an inverse square law shown in equation (1.17). This displacement vector varies in time as both the planet and small body orbit the Sun. Thus, the force perturbing the orbit of the small body and the acceleration caused by the

perturbation, a_{cij}, also vary in time. The same argument can be made for any other planet in resonance with the small body.

a_{cij} can be expressed as an infinite sum of cosines of resonance angles. This infinite sum is known as the disturbing function, and each term in the infinite sum describes a particular subresonance (Murray & Dermott, 1999; Ellis & Murray, 2000; Laskar & Boué, 2010). Each term in the disturbing function has the general form:

$$a_{cij} \sim e^{j_5} e_p^{j_6} \cos(j_1\lambda + j_2\lambda_p + j_3\Omega - j_4\Omega_p + j_5\overline{\omega} + j_6\overline{\omega}_p) \qquad (1.49)$$

where j_3, j_4, j_5 and j_6 are integers; λ is the mean longitude of the small body; λ_p is the mean longitude of the planet; Ω is the longitude of ascending node of the small body; Ω_p is the longitude of ascending node of the planet; $\overline{\omega}$ is the longitude of perihelion of the small body; and $\overline{\omega}_p$ is the longitude of perihelion of the planet.

When the inclination and eccentricity of the small body are much larger than that of the planet, terms involving Ω_p and $\overline{\omega}_p$ can be ignored.

Futhermore, when the planet and small body exist in a particular subresonance, $j_2 : j_1$, the term in the infinite sum for that subresonance time averages to a non-zero number. Other non-resonant terms time average to zero making a_{cij} dependent mostly on the dominant resonant term.

Two particular subresonances are of interest. These are:

$$a_{cij} \sim \cos(j_2\lambda_p - j_1\lambda - q_q\overline{\omega}) \qquad (1.50)$$

and

$$a_{cij} \sim \cos(j_2\lambda_p - j_1\lambda - q_q\Omega) \qquad (1.51)$$

(e.g. Roig et al., 2002; Masaki et al., 2003; Bailey & Malhotra, 2009; Tiscareno & Malhotra, 2009). A resonance angle associated with a subresonance will be denoted as ϕ. When ϕ oscillates in time (or librates) it means that the longitude (or angle) of the q_{th} conjunction between the small body and the planet changes very slowly or librates about a constant value. This angle librating in time then is the definitive sign that the small body is in a mean motion resonance with the planet (Malhotra, 1994).

While the small body is in a mean motion resonance with a planet, if conjunctions occur when the orbits are closest together, then close encounters between the planet and small body are possible and these tend to destabilize the orbit of the small body (Holman & Wisdom, 1993; Duncan et al., 1995). If a small body in the resonance is not planet-crossing, then another effect which can happen is that the eccentricity of the small body's orbit can be pumped up until it becomes planet crossing (Wisdom, 1982).

Contrarily, if conjunctions occur when the orbits are farthest apart it can prevent close encounters which results in more stable orbits for small bodies in the resonance (Malhotra, 1994). Such is the case for a group of small bodies

known as Plutinos which are in a 2:3 resonance with Neptune (Jewitt & Luu, 1996).

Small bodies may also become temporarily stuck in a resonance, leave it and then return. This is an effect known as resonance sticking (Lykawka & Mukai, 2007; Bailey & Malhotra, 2009).

If ϕ does not librate but instead circulates then it time averages to zero and is not a dominant term in the disturbing function. This means that the small body is not in the $j_2 : j_1$ resonance with the planet (e.g. Murray & Dermott, 1999; Roig et al., 2002; Smirnov & Shevchenko, 2013).

1.3.2 Secular Resonances

Other types of resonances besides mean motion resonances also exist. When the precession rates of two orbits are commensurate, the two orbits are in a state of secular resonance with each other. These commensurate precession rates may be between the precession rates of two longitudes of perihelion, two longitudes of ascending node and other pairs of orbital precession rates.

Secular resonances also perturb the orbits of small bodies but on longer time scales than those of MMR (Froeschle & Morbidelli, 1994; Moons & Morbidelli, 1995; Murray & Dermott, 1999). Some of the notable frequencies of orbital precession associated with the Jovian planets are

g_5 = frequency of precession of the longitude of perihelion of Jupiter

g_6 = frequency of precession of the longitude of perihelion of Saturn

g_7 = frequency of precession of the longitude of perihelion of Uranus

g_8 = frequency of precession of the longitude of perihelion of Neptune

s_5 = frequency of precession of the longitude of ascending node of Jupiter

s_6 = frequency of precession of the longitude of ascending node of Saturn

s_7 = frequency of precession of the longitude of ascending node of Uranus

s_8 = frequency of precession of the longitude of ascending node of Neptune

Values of these are shown in Table 1.3. These are known as the eigenfrequencies of the Solar system for the Jovian planets. The terrestrial planets have similarly defined eigenfrequencies (g_1 to g_4 and s_1 to s_4). If the precession rate of the longitude of perihelion of the orbit of a body is at or near g_5, g_6, g_7 or g_8, then the body is said to be in the ν_5, ν_6, ν_7 or ν_8 resonance respectively. If the precession rate of the longitude of ascending node of the orbit of a body is at or near s_5, s_6, s_7 or s_8, then the body is said to be in the $\nu_{15}, \nu_{16}, \nu_{17}$ or ν_{18} resonance respectively (Williams, 1969; Froeschle & Scholl, 1989).

A special case of a secular resonance occurs when the precession rate of the argument of perihelion of the small body is zero ($\dot{\omega} \approx 0$). This resonance is known as a Kozai-Lidov resonance (Kozai, 1962; Sie et al., 2015; Shevchenko, 2017). In this type of resonance, the component of angular momentum of a small body parallel to the angular momentum of the perturbing body is conserved. This quantity, known as the Kozai integral can be expressed as:

$$I_K = \cos i \sqrt{1 - e^2} \qquad (1.52)$$

where i and e are the inclination and eccentricity of the small body orbit.

Table 1.3: Eigenfrequencies of the Jovian planets. Values are taken from Murray & Dermott (1999)

Name	Value (arcsec/yr)	Period (years)
g_5	$\frac{4.29591''}{\text{year}}$	3.0×10^5
g_6	$\frac{27.77406''}{\text{year}}$	4.7×10^4
g_7	$\frac{2.71931''}{\text{year}}$	4.8×10^5
g_8	$\frac{0.63332''}{\text{year}}$	2.0×10^6
s_5	$\frac{-25.73355''}{\text{year}}$	5.0×10^4
s_6	$\frac{-25.73355''}{\text{year}}$	5.0×10^4
s_7	$\frac{-2.90266''}{\text{year}}$	4.5×10^5
s_8	$\frac{-0.67752''}{\text{year}}$	1.9×10^6

As a consequence of this, any increase in e must be accompanied by a decrease in i and vice versa. These coupled oscillations between e and i are the hallmark of the Kozai resonance.

1.3.3 Resonances and Chaos

Resonances do not exist at only one point in phase space but instead take up a volume in six-dimensional space. This allows for the possibility of overlapping resonances. The orbits of small bodies in the vicinity of overlapping resonances can become highly chaotic.

Chaos is the study of extreme sensitivity to initial conditions (Gleik, 1987). This means that because of chaos, tiny differences in the initial conditions between two different systems can result in very different final states over time.

For example, consider two massless test particles orbiting the Sun in orbits which differ only infinitesimally as shown in Figure 1.5. Test particles are placed into both orbits in positions which differ only minutely in phase space. In diagram B the same two test particles are shown at a later time. The states of the two test particles have diverged.

Thus, there is potentially an initial difference between each position and velocity vector component between the two for a total of up to six component differences (3 position and 3 velocity). These are: $\Delta x_0 = x_{20} - x_{10}$, $\Delta y_0 = y_{20} - y_{10}$, ... $\Delta v_{zo} = v_{2z0} - v_{1z0}$.

If the orbits are chaotic, then these infinitesimal differences will grow exponentially in time. Thus, for any particular vector component initial difference, Δx_0, the difference Δx at a time t can be written in the form

$$\Delta x = \Delta x_0 e_{exp}^{\gamma t} \tag{1.53}$$

Of the six orbital component differences one of them will grow faster than the
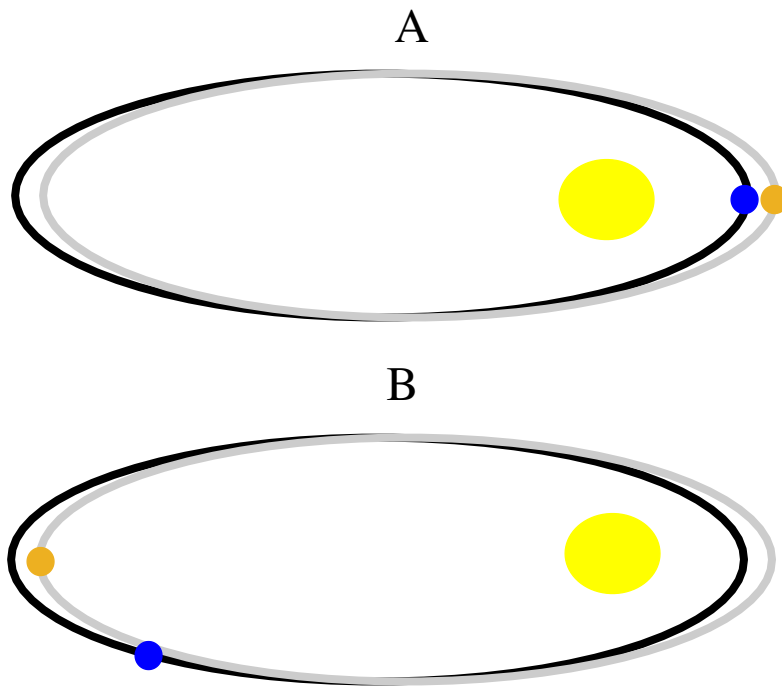
Figure 1.5: In diagram A two orbits with the same eccentricity are shown which differ in semi-major axis by an infinitesimally small amount. Test particles are placed into both orbits in positions which differ only minutely in phase space. In diagram B the same two test particles are shown at a later time. The distance between the two particles in phase space has greatly increased showing that an initially small difference has resulted in a large change.

others and thus have largest exponent, γ_{max}, of the six. This exponent is known as the Lyapunov Characteristic exponent or Maximum Lyapunov Exponent and is given by

$$\gamma_{max} = \lim_{t \to \infty} \frac{1}{t} \int_0^t \frac{\dot{\Delta x}(t')}{\Delta x(t')} dt' \tag{1.54}$$

The associated Lyapunov time, t_{lyp}, is the time it takes the associated component difference to grow by a factor of e_{exp} and is given by

$$t_{lyp} = \frac{1}{\gamma_{max}} \tag{1.55}$$

The value of t_{lyp} is dependent on the integration time (Whipple, 1995). Orbits with shorter Lyapunov times are considered more chaotic than those with longer Lyapunov times. Thus, t_{lyp} can be used to measure the chaoticity of an orbit.

Another quantity used to measure chaos related to the Lyapunov Characteristic exponent is the MEGNO (Mean Exponential Growth of Nearby Orbits) parameter, Y. The time averaged MEGNO parameter, $\langle Y \rangle$, is a dimensionless quantity directly proportional to the Lyapunov Characteristic exponent and time, t, via

$$\langle Y \rangle = t \frac{\gamma_{max}}{2} \tag{1.56}$$

(Cincotta & Simó, 2000; Goździewski et al., 2001; Cincotta et al., 2003; Giordano & Cincotta, 2004; Hinse et al., 2010). In the limit $t \to \infty$ the value of $\langle Y \rangle$ asymptotically approaches 2.0 for quasi-periodic orbits and rapidly diverges far from 2.0 for chaotic orbits. The MEGNO parameter can be calculated by solving the following integral

$$Y = \frac{2}{t} \int_0^t \frac{\dot{\Delta x}(t')}{\Delta x(t')} t' dt' \tag{1.57}$$

The time averaged MEGNO parameter is given by

$$\langle Y \rangle = \frac{1}{t} \int_0^t Y(t') dt' \tag{1.58}$$

MEGNO has been used to study various objects including galaxies (Cincotta & Simó, 2000; Cincotta et al., 2003), irregular Jovian moons (Hinse et al., 2010) and exoplanets (Goździewski et al., 2001).

1.4 Numerical Integrators

A numerical integrator is an algorithm designed to advance a system of N interacting bodies from an initial state, Ψ_0, to a final state, Ψ_f. The final state may be after or before the time of the initial state.

Generally the integration from the initial to the final state does not occur in one step but instead proceeds through a series of intermediate steps. That

is, the integrator advances the initial state to some intermediate state, Ψ_1, and then integrates that state to another intermediate state, Ψ_2 and so on until the integration ends and the final state has been reached. The process of moving from one state to the next is known as integration.

How integration is done varies with the integrator.

1.4.1 Euler's Method

Euler's Method of integration uses a constant time step, Δt, to advance from Ψ_{n-1} to Ψ_n. For one body this can be written as

$$\vec{r}_{1n} = \vec{r}_{1(n-1)} + \vec{v}_{1(n-1)}\Delta t \tag{1.59}$$

$$\vec{v}_{1n} = \vec{v}_{1(n-1)} + \left(\vec{a}_c\right)_{1(n-1)}\Delta t \tag{1.60}$$

The time for the Ψ_n state is found from

$$t_n = t_{n-1} + \Delta t \tag{1.61}$$

The acceleration vectors for the state Ψ_n are found from Equation 1.19.

Errors occur in $\vec{r}_{1n}$, $\vec{v}_{1n}$ and $\vec{a}_{c1n}$ with each integration due to the time interval Δt being non-zero and to the precision of the computer being used. A smaller time step reduces error but requires more time to perform the task. The experimenter must select a time interval, Δt, that is small enough to achieve a desired accuracy and large enough to complete the task within an allotted time.

1.4.2 Other Integrators

Other more efficient integrators reduce the error using more efficient code rather than a smaller time interval. Integrators may also make use of a variable time step to improve accuracy. For example, when a small body has a close encounter with a planet it may cause a large acceleration which greatly increases the error when integrating. But an integrator with a variable time step shrinks the size of the time step when close encounters occur and then enlarges it again after the encounter. The result is reduced error with only a minimal increase in task time.

Other integrators include the MERCURY (Chambers, 1999) collection of integrators, Bulirsh-Stöer (Hairer et al., 1993), SWIFT (Levison & Duncan, 1994), and the REBOUND N-body simulation package which is a suite of integrators including Wisdom-Holman Fast (Rein & Tamayo, 2015), and IAS15 (Rein & Spiegel, 2015). For any integrator, the acceleration of each body for any state of the system can be found from Equation 1.19.

1.4.3 The Bulirsh-Stöer Method

This method improves on the Euler method by partitioning the time step Δt into n steps of size h. The first step in advancing from Ψ_0 to Ψ_1 is the Euler method. For the position this can be written as

$$\vec{r}_{11} = \vec{r}_{10} + v_{10}\Delta t \tag{1.62}$$

But then state Ψ_2 is found by advancing from Ψ_0 to Ψ_2 using a time step of $2h$ and vectors $\vec{a}_c$ and $\vec{v}$ from Ψ_1. For the position this can be written as

$$\vec{r}_{12} = \vec{r}_{10} + v_{11}\left(2\Delta t\right) \tag{1.63}$$

Similarly, intermediate values $\vec{r}_{13}$, $\vec{r}_{14}$ ... $\vec{r}_{1n}$ are found. The final result is found by averaging two different estimates for $\vec{r}_{1n}$: one found by advancing from $\vec{r}_{1(n-2)}$ to $\vec{r}_{1(n)}$ using a stepsize of $2h$ and the other found by advancing from $\vec{r}_{1(n-1)}$ to $\vec{r}_{1n}$ using a stepsize of h.

$$\vec{r}_1(t_0 + \Delta t) = \frac{1}{2}\left[\vec{r}_{1n} + \vec{r}_{1(n-1)} + hv_{1n}\right] \tag{1.64}$$

The method is analogous for velocity.

1.4.4 The Hybrid Integrator of Mercury

Mercury is a suite of five integrators one of which is the Hybrid integrator. The Hybrid integrator makes use of two integrators - a symplectic integrator and a Bulirsh-Stöer integrator. The symplectic integrator uses a constant time step and attempts to maintain a constant energy of the system. It does this by analytically solving the equations of motion which are nearly identical to the ones being considered. This works well if distances between bodies are large, but breaks down for close encounters. In that case, the Bulirsh-Stöer integrator takes over which is slower but much more deft at handling close encounters.

The symplectic integrator works by separating the Hamiltonian into at least two parts $H = H_0 + H_1 + ...$ For example, consider the case where you have the Sun, of mass $m_\odot$ and a set of N gravitationally interacting bodies which includes planets and small bodies. If a mixture of heliocentric coordinates, $r_\odot$, and barycentric velocities is used, then the Hamiltonian separates into three parts with the third part containing the kinetic energy of the bodies. This is written as:

$$H_0 = \sum_{i=1}^{N}\left(\frac{p_i^2}{2m_i} - \frac{G_c m_\odot m_i}{r_{i\odot}}\right) \tag{1.65}$$

$$H_1 = -G_c \sum_{i=1}^{N}\sum_{j=i+1}^{N}\frac{m_i m_j}{r_{ij}} \tag{1.66}$$

$$H_2 = \frac{1}{2m_\odot} \left(\sum_{i=1}^{N} p_i \right)^2 \tag{1.67}$$

where p is momentum, r is position and m is mass. Here, H_0 is just the Hamiltonian for a Keplerian orbit and is solvable analytically. H_1 is the gravitational potential energy between each pair of bodies. Each part can be integrated independently from the others. The error which occurs after each time step varies with $\epsilon \Delta t^{n+1}$ where n is the integrator order, and ϵ is largest value in the set $\{ \frac{H_1}{H_0}, \frac{H_2}{H_0}, ... \}$.

The symplectic integrator works well when distances between bodies are large as ϵ is small in that case. However, when a small body has a close encounter with a planet, the distance between the small body and the planet becomes small which causes H_1 to be large. This causes ϵ to be large resulting in large errors.

Shortening the time step during close encounters is a potential solution to this problem. However, when this is done, energy is no longer constant. Another attempt to solve the problem of close encounters is to simply add H_1 onto H_0 for the duration of the close encounter. But this leads to the same error.

The Hybrid integrator solves this problem by rewriting H_0 and H_1 in terms of a changeover function, K, which is used to determine under what conditions the Bulirsh-Stöer integrator should be used. The reformulated H_0 and H_1 are:

$$H_0 = \sum_{i=1}^{N} \left(\frac{p_i^2}{2m_i} - \frac{G_c m_\odot m_i}{r_{i\odot}} \right) - G_c \sum_{i=1}^{N} \sum_{j=i+1}^{N} \frac{m_i m_j}{r_{ij}} \left[1 - \mathrm{K}(r_{ij}) \right] \tag{1.68}$$

$$H_1 = -G_c \sum_{i=1}^{N} \sum_{j=i+1}^{N} \frac{m_i m_j}{r_{ij}} \mathrm{K}(r_{ij}) \tag{1.69}$$

K is chosen so that K$\rightarrow$ 0 during a close encounter, and K$\rightarrow$ 1 otherwise. If K= 1 the second term in H_0 vanishes, and H_0 is just the Hamiltonian for Keplerian orbit. By a process of trial and error by Chambers (1999), K was found to be related to a quantity y defined by:

$$y = \left(\frac{r_{ij} - 0.1 r_{crit}}{0.9 r_{crit}} \right) \tag{1.70}$$

The critical distance, r_{crit}, is found from the larger of these two: 3 Hill radii and $0.5 \Delta t v_{max}$ where v_{max} is the largest likely orbital velocity of any single body. Figure 1.6 shows K as a function of $\frac{r_{ij}}{r_{crit}}$. The relationship between K and y is:

1.4.5 The IAS15 Integrator

The IAS15 (Implicit integrator with Adaptive time Stepping, 15th order) is one integrator in the REBOUND simulation package. It is capable of handling both conservative and non-conservative forces as well as velocity dependent forces.

$$
K = \begin{cases} 0 & \text{for } y < 0 \\ \frac{y^2}{2y^2 - 2y + 1} & \text{for } 0 < y < 1 \\ 1 & \text{for } y > 1 \end{cases}
$$
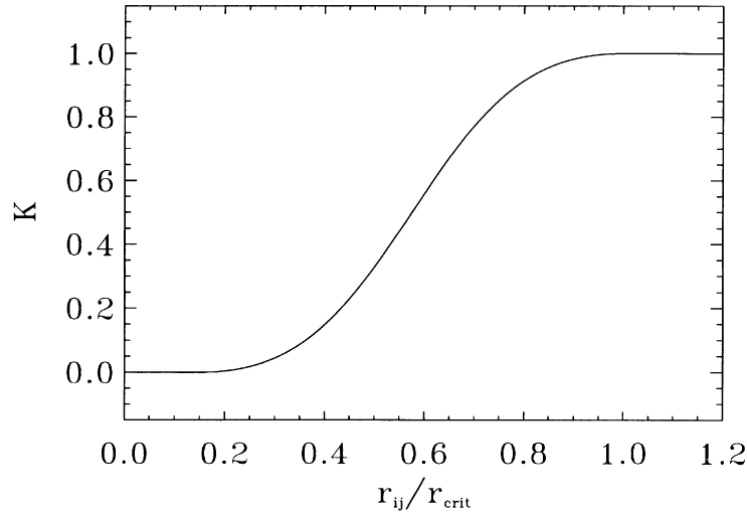
Figure 1.6: The changeover function, K, used to determine when the Bulirsh-Stöer integrator should take over during a close encounter. This changeover occurs when the ratio of the distance between two bodies, r_{ij}, to some critical distance, r_{crit}, approaches zero. Image taken from Chambers (1999).

Though not a symplectic integrator, it still attempts to preserve the system's energy by using a large order to keep the errors in energy of a system below machine precision.

The result is that the conservation properties of IAS15 are as good or better than a symplectic integrator. An integrator is optimized if its error in energy displays a random walk in time $\left(\sim t^{\frac{1}{2}} \text{ or } \sim t^{\frac{3}{2}} \text{ where } t \text{ is time} \right)$. This is known as Brouwer's law and the IAS15 integrator obeys it.

The algorithm attempts to numerically solve the equation

$$
\ddot{x} = f(\dot{x}, x, t) \tag{1.71}
$$

To do this, the function $f(\dot{x}, x, t)$ is approximated using a 7th order polynomial

$$
\ddot{x}(t) \approx \ddot{x}_0 + a_0 t + a_1 t^2 + \ldots + a_6 t^7 \tag{1.72}
$$

This is then rewritten using $h = \frac{t}{dt}$, and $b_k = a_k dt^{k+1}$ to achieve

$$\ddot{x}(t) \approx \ddot{x}_0 + b_0 h + b_1 h^2 + ... + b_6 h^7 \tag{1.73}$$

For the very first iteration, a constant acceleration is assumed which gives predictions of the position and velocity at the end of the iteration. The forces are then used to find the position and velocity and the differences between the predicted and calculated b_k are recorded. The iteration continues until the error is below machine precision.

For the next iteration, the errors found in b_k from the previous iteration can be used to make an even better prediction of the position and velocity at the end of that iteration. If the error does not converge to machine precision after 12 iterations then the time step is considered to be too large, and the time step can then be adapted. The result is an integrator which keeps energy errors below machine precision for at least one billion orbits using only 100 time steps per orbit.

1.4.6 Application of Numerical Integrators

Integrators such as the ones discussed here can be applied to a wide variety of dynamical problems from galactic collisions to dust particles.

One subfield in which numerical integrators are useful which is also the subfield of interest in this work is the area of dynamics of small bodies of the Solar system. Objects in a simulation representing small bodies are often referred to as test particles.

A problem which often arises in this area is the study of the dynamical history or future of a known small body. In this case, the orbital parameters of the body may be known but will always contain uncertainties.

If only a single test particle is integrated then the experimenter can never be sure that the results are accurate due to the uncertainty in the initial conditions. This problem can be combatted by integrating a very large number of massless test particles initially with orbital parameters spread throughout the uncertainties in the known orbital parameters of the body. In this case, the test particles are known as clones of the actual body.

Though massless, the perturbing effects of the gravity of more massive bodies on their orbits can still be studied as the perturbing acceleration depends only on the mass of the perturber, and the lack of mass prevents the test particles from interfering with each other.

Care must be taken when applying this method. With each time step, more error in introduced in the position and velocity of each test particle. This is especially true if test particles have close encounters with massive objects such as planets.

The experimenter must be careful not to draw definitive conclusions from the behavior of just one test particle and not link that behavior to that test particle's initial conditions.

Instead, the behavior of one test particle should be taken only as one possible behavior that the actual object could display. A statistical analysis of all the test particles can be made to determine likely behaviors or fates of the actual body. These statistics are improved as the number of clones is increased.

In the next section, different types of small bodies in the Solar system will be discussed.

1.5 Small Bodies of the Solar System

Small bodies also known as minor planets, exist throughout the Solar system orbiting the Sun from inside Earth's orbit to outside the orbit of Neptune and everywhere in between.

Populations and subpopulations of small bodies are classified based on such properties as their physical or orbital characteristics. The study of small bodies is important for multiple reasons which include to determine the threat small bodies pose to Earth[4] (Hahn & Bailey, 1990; Napier et al., 2015), to indicate the existence of unseen planets (Brown, 2017; Batygin & Morbidelli, 2017) and to give clues about the formation of the Solar system and origin of water on Earth[5] (Horner & Jones, 2010; Altwegg et al., 2015).

1.5.1 Asteroids

Asteroids are objects that are mainly composed of rocky and metallic material that are generally accepted to be debris left over from the formation of the Solar system. The exact composition varies with the asteroid, but in addition to rocky material, asteroids may contain metals and volatiles including organic material (Burbine, 2017).

Most asteroids orbit the Sun between the orbits of Mars and Jupiter. These asteroids with semi-major axes between 2 au and 4.28 au are known as Main-Belt Asteroids or MBAs, and the region in which they orbit is called the Main Asteroid Belt. The Asteroids in this belt never accreted into a planet because of perturbations from Jupiter (Petit et al., 2001).

Over 500,000 objects are listed in the Minor Planet Center database as existing in this region[6]. Daniel Kirkwood discovered regions in the main asteroid belt where there are relatively lower populations of asteroids compared to nearby orbits and that these gaps were related to mean motion orbital resonances with Jupiter (Kirkwood, 1867). These regions are now known as Kirkwood gaps (Ryden , 2016). Figure 1.7 shows a histogram of small bodies in the inner Solar system. The gaps in the Main Asteroid Belt at the location of mean motion resonances can clearly be seen.

---

[4]https://www.nasa.gov/mission_pages/asteroids/overview/index.html (accessed Dec. 28, 2017)
[5]https://www.mps.mpg.de/planetary-science/small-bodies-comets-research (accessed Dec. 28, 2017)
[6]https://www.minorplanetcenter.net/iau/MPCORB.html (accessed Sep. 24, 2017)

Table 1.4: The current number of Trojans by planet according to the Minor Planet Center.

Planet	Number of Trojans
Earth	1
Mars	9
Jupiter	6701
Uranus	1
Neptune	17

Other dynamical classes of asteroids exist. Asteroids which have the same (or nearly the same) semi-major axis as a planet are known as Trojan Asteroids. Another way to state this is that Trojan Asteroids are in a 1:1 mean motion orbital resonance with a planet. Trojan Asteroids have been discovered for Jupiter, Uranus, Neptune, Mars, Earth and Venus (Marzari & Scholl, 2002; Scholl et al., 2005; Connors et al., 2011; Lykawka et al., 2011; Aron, 2013; de la Fuente Marcos & de la Fuente Marcos, 2014).

While Jupiter boasts a Trojan population which exceeds 6,000, by contrast, no Saturn Trojans have been discovered. This is likely because the Trojan regions of Jupiter are dynamically stable on Gyr timescales while those of Saturn are mostly not except for a few small niches. Saturn may once have had a large Trojan population, but even if it did, today this population would have been greatly depleted due to the overlap of the Trojan region with the Saturn-Jupiter 2:5 mean motion resonance and secular resonances (Marzari & Scholl, 2000; Marzari, et al., 2002; Nesvorný & Dones, 2002).

Nevertheless, the instability of the Trojan region does not exclude the possibility that Saturn has captured Centaurs into temporary Trojan orbits (Horner & Wyn Evans, 2006), and future surveys such as the LSST may indeed discover such objects. Jupiter has by far the largest number of discovered Trojans. The number of Trojans for each planet can be found at the Minor Planet Center[7]. The current numbers of Trojans by planet are shown in Table 1.4. It is believed that as the planets migrated, they captured objects into their Trojan regions. This explains the high inclinations of the orbits of Trojans of Jupiter and Neptune (Gomes et al., 2005).

Some asteroids come dangerously near to or even cross Earth's orbit. These asteroids are known as Near Earth Objects or NEOs. The term Near Earth Asteroids or NEAs is also used. There are three main subtypes of NEAs: Amor, Apollo, and Aten which are defined using their semi-major axes and perihelion distances, q, as follows:

- Amors - have semi-major axes greater than 1 au and 1.017 au $< q <$ 1.3 au

- Apollos - have semi-major axes greater than 1 au and $q <$ 1.017 au which places them in Earth-crossing orbits with semi-major axes beyond Earth's

[7]https://www.minorplanetcenter.net/iau/lists/Trojans.html (accessed Dec. 10, 2017).

Table 1.5: The number of NEAs listed by subtype according to the Minor Planet Center.

Type of Asteroid	Number
Aten	1285
Apollo	8582
Amor	7393
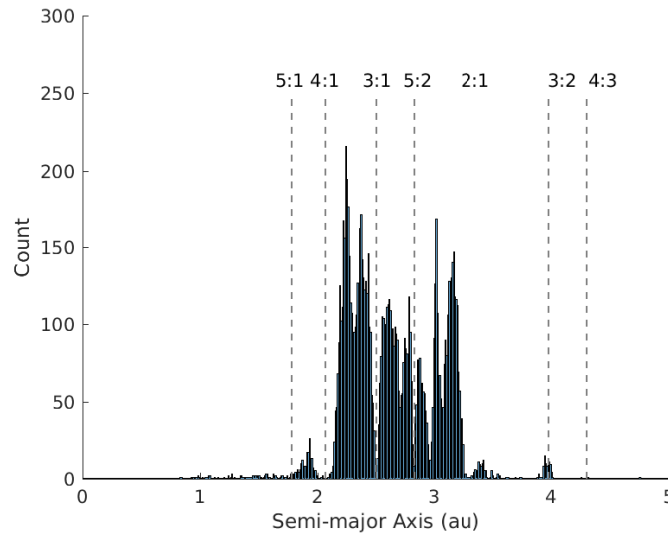
Figure 1.7: A histogram of small bodies in the inner Solar system. The large concentration of asteroids is the Main Asteroid Belt. Also shown are the locations of a few of Jupiter's interior mean motion resonances. Note the dearth of asteroids at these locations.

- Atens - have semi-major axes less than 1 au

(Norton & Chitwood, 2008). The Apollos are Earth-crossing but the Amors are not. Atens which are not Earth crossing are referred to as Atiras[8].

As of this writing the Minor Planet Center classifies over 17,000 objects as NEAs[9]. The breakdown by subtype is shown in Table 1.5. These types of asteroids may exist in part due to perturbations from giant planets which are known to perturb the orbits of asteroids into planet-crossing orbits. Specifically the ν_6 secular resonance of Saturn and the 3:1 MMR of Jupiter are believed to be responsible for the transport of asteroid fragments to Earth-crossing orbits (e.g. Wisdom, 1982, 1983; Froeschle & Scholl, 1986).

---

[8]https://cneos.jpl.nasa.gov/about/neo_groups.html (accessed January 1, 2018)
[9]https://www.minorplanetcenter.net/iau/lists/MPLists.html (accessed Dec. 10, 2017).

1.5.2 Comets

Comets are bodies of ice and rock that orbit the Sun in much more eccentric orbits than those of the planets. What differentiates comets from asteroids is their large amount of ice. In general, at large heliocentric distances, comets exist as single nuclei of ice and rock orbiting the Sun (Levison & Duncan, 1997). But at closer distances ices begin to sublimate causing the comet to have its own atmosphere. This atmosphere appears as a fuzzy ball around the comet nucleus and is called the coma (Bennett et al., 2016; Fraknoi et al., 2016). In certain cases, activity is also driven by mechanisms unrelated to heliocentric distance (Jewitt, 2009).

As the comet continues to draw closer to the Sun, two tails develop - the ion tail and the dust tail (Zeilik, 2002; Fraknoi et al., 2016). Each tail has a general direction of away from the Sun. The tails develop by two different mechanisms. The dust tail develops due to radiation pressure from the Sun. As particles sublimate and leave the nucleus, radiation pressure pushes the particles outward as they continue to orbit the Sun. The result is a curl-shaped tail.

The ion tail develops due to fast moving charged particles from the Sun whose magnetic field rips particles right off the nucleus, trapping them and carrying them along. With each passage around the Sun, a comet loses some of its own mass which is shed in the form of particles which spread throughout the comet's orbit over time (Festou et al., 2004).

Traditionally, comets have been categorized as either short period or long period. Long-period comets revolve around the Sun with orbital periods greater than 200 years, and short-period comets revolve around the Sun with orbital periods less than 200 years (Levison, 1996).

1.5.3 Comet Origins

It is generally accepted that originally many (but not all!) of the icy bodies known as comets originated from somewhere beyond Neptune in orbits which did not bring them into the inner Solar system.

Today this region beyond Neptune has several major subpopulations in which these bodies could have originally abided including the Edgeworth-Kuiper Belt (Levison & Duncan, 1997), the Scattered Disk (Volk & Malhotra, 2008), or in the Oort cloud (Emel'yanenko et al., 2005).

The Edgeworth-Kuiper Belt is a region between the semi-major axis of Neptune's orbit and 48 au (the location of the 1:2 MMR of Neptune). Small bodies in orbits with semi-major axes in this region are called Kuiper Belt Objects (or KBOs) (Lykawka & Mukai, 2007). A medium-sized Kuiper Belt Object is on the order of 10^2 km in diameter, and the largest are on the order of 10^3 km in diameter (Murray-Clay & Schlichting, 2011).

The Scattered Disk is a region between the Edgeworth-Kuiper Belt and 1000 au (Tiscareno & Malhotra, 2003; Lykawka & Mukai, 2007). Small bodies in orbits with semi-major axes in this region are known as Scattered Disk Objects

or SDOs. At this time, the Minor Planet Center recognizes over 540 SDOs[10].

The Oort Cloud is a cloud of comets surrounding the Sun (Oort, 1950). Objects in this cloud are known as Oort Cloud Objects or OCOs. The exact boundaries of the Oort cloud remain uncertain, but the outer boundary is believed to extend out to at least 20,000 au (Hills, 1981) and may extend out to 200,000 au (Duncan et al., 1987; Dones et al., 2015). Long-period comets are believed to have originated in the Oort cloud (e.g. Oort, 1950; Fouchard et al., 2014).

OCOs, KBOs, SDOs and other small bodies in orbits which have semi-major axes beyond the orbit of Neptune are classified as Trans-Neptunian Objects (or TNOs) by the Minor Planet Center of which 1900 are known[11]. So it can be said that some comets originally would have been classified as TNOs.

However, over time, the orbits of these bodies were perturbed by gravitational perturbations from planets (Duncan et al., 1988; Levison & Duncan, 1997; Volk & Malhotra, 2008), a passing star (Oort, 1950; Hills, 1981) and galactic tides (Heisler & Tremaine, 1986; Duncan et al., 1987). These perturbations caused the orbits to evolve into those which could enter the inner Solar system.

Thus, the specific classification of any small Solar system body such as a comet may be ephemeral as small bodies may transition back and forth between different classes of objects during their lifetime (Tiscareno & Malhotra, 2003; Horner et al., 2004).

1.5.4 Comet Taxonomy

The very basic taxonomical scheme which classified comets as short-period or long-period was based on the longest time over which calculated orbital parameters for comets were considered reliable which then was about 200 years. Today, this scheme has become obsolete (Levison, 1996). Comet taxonomy is fluid, and more than one taxonomical scheme has been proposed.

The taxonomical scheme of Levison (1996) separates comets into two broad categories based on the value of their Tisserand parameter with Jupiter, T_J: Nearly Isotropic Comets have $T_J < 2$ and Ecliptic Comets have $T_J > 2$.

Ecliptic Comets are further subclassified as Jupiter-Family, Chiron-type or Encke-type. Jupiter-Family comets have $2 < T_J < 3$ (e.g. Levison et al., 2006). Encke-type comets have $T_J > 3$ with semi-major axes less than that of Jupiter's and Chiron type comets have $T_J > 3$ with semi-major axes greater than that of Jupiter's.

Nearly Isotropic Comets are split into two classes: New and Returning. Comets with $a > 10,000$ au are classified as New and comets with $a < 10,000$ au au are classified as Returning. Returning comets are further split in two classes of their own: those with $a < 40$ au are termed Halley-type and those with $a > 40$ au are termed External (Levison, 1996). The entire scheme is shown in Figure 1.8.

---

[10]https://www.minorplanetcenter.net/iau/lists/t_centaurs.html (accessed Dec. 10, 2017)
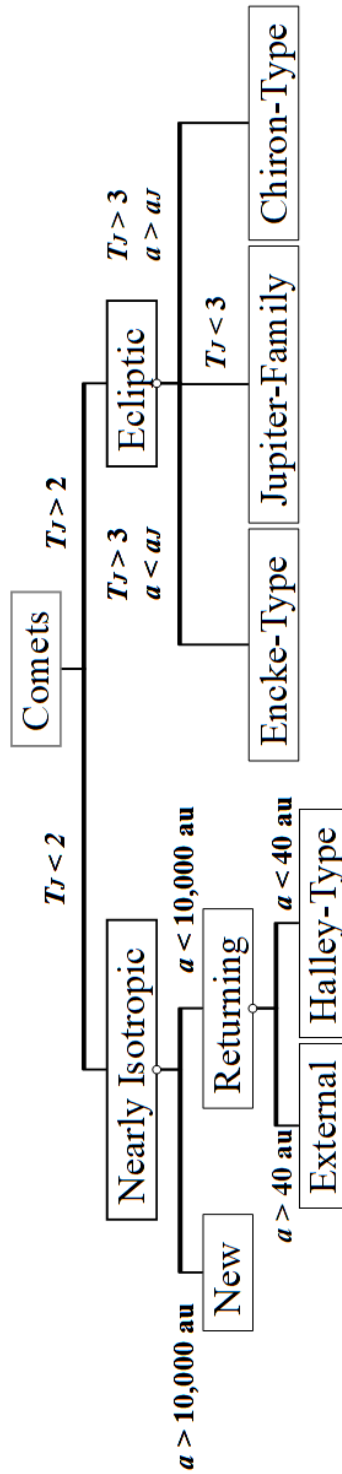[11]https://minorplanetcenter.net/iau/lists/t_tnos.html (accessed Dec. 10, 2017).

34

Figure 1.8: The comet taxonomical scheme of Levison (1996). T_J is the Tisserand parameter with respect to Jupiter and a_J is the semi-major axis of Jupiter. (Image created by author but based on an image in Levison (1996))

The taxonomical classification scheme of Horner et al. (2003) (henceforth known as the HEBA scheme) places each comet, Centaur and TNO into one of two broad classes: comets and comet-like bodies.

Comet-like bodies are placed into a major class based on the planet controlling the dynamics of the body at perihelion and aphelion using up to two letters and then are placed into a subclass using a Roman numeral based on the Tisserand parameter, T_p, of the planet controlling the dynamics of the small body at perihelion.

The first letter of the major class is the starting letter of the planet controlling the dynamics of the body at perihelion, and the second that of the planet controlling the body at aphelion or if no planet controls at aphelion the letters E, T or EK are used depending on values of q and Q. For example, if Saturn controls the dynamics of the body at perihelion and Neptune at aphelion then the body is said to be in the SN class.

If the body is controlled by the same planet at both perihelion and aphelion then only the one letter of the controlling planet is used. Table 1.6 shows the letters used in the HEBA classes and the ranges over which each planet controls the dynamics of a small body at perihelion and aphelion based on Horner et al. (2003).

If there is no controlling planet at aphelion then if the perihelion lies in the range 4 au $< q <$ 33.5 au, and the aphelion lies in the range 33.5 au $< Q <$ 60 au then the letter E is used for Edgeworth-Kuiper belt for the second letter of the major class. If the perihelion lies in the range 4 au $< q <$ 33.5 au, and the aphelion lies in the range $Q >$ 60 au then the letter T is used for Trans-Edgeworth-Kuiper Belt for the second letter of the major class.

There are two special cases where no planet controls at perihelion or aphelion. Objects with $q >$ 33.5 au and $Q >$ 60 au are said to be in the T class, and objects with $q >$ 33.5 au and $Q <$ 60 au are said to be in the EK class.

Table 1.6: The letters used in the HEBA classes and the ranges over which each planet controls the dynamics of a small body at perihelion and aphelion based on Horner et al. (2003). The first four letters shown are for the giant planets and may be used as the first or second letter of the major class. The E class may be used as the second letter of the major class only. Classes EK and T are special cases where no planet controls at perihelion or aphelion.

Letters	Perihelion (au)	Aphelion (au)
J	4 - 6.6	4 - 6.6
S	6.6 - 12	6.6 - 12
U	12 - 22.5	12 - 22.5
N	22.5 - 33.5	22.5 - 33.5
E	$4 < q < 33.5$	$Q < 60$
EK	$q > 33.5$	$Q < 60$
T	$q > 33.5$	$Q > 60$

The four subclasses are given in Table 1.7 and are labeled I, II, III and IV based

on the value of T_p.

Table 1.7: The HEBA subclasses based on the Tisserand parameter of the planet controlling the dynamics of the small body at perihelion. Based on Horner et al. (2003).

Subclass	Tisserand Parameter
I	$T_p \leq 2$
II	$2 < T_p < 2.5$
III	$2.5 < T_p < 2.8$
IV	$T_p > 2.8$

For example, using Table 1.7, if Saturn controlled the dynamics of a small body at perihelion, Uranus controlled them at aphelion, and the Tisserand parameter with respect to Saturn was 2.6 then the object would be classified as SU_{III}. As another example, if Saturn controlled the dynamics at perihelion, $Q = 35$ au and $T_p = 2.85$ then the object would be classified as SE_{IV}.

Four comet classes cover all bodies that have perihelia $q \leq 4$ au and are defined in Table 1.8. The four comet classes in the HEBA taxonomical scheme are E = Encke-type comet, SP = short-period comet, I = intermediate-period comet and L = long-period comet.

Table 1.8: The four comet classes in the HEBA taxonomy. E = Encke-type comet, SP = short-period comet, I = intermediate-period comet and L = long-period comet. Based on Horner et al. (2003).

Class	Perihelion (au)	Aphelion (au)
E	$q \leq 4$	$Q \leq 4$
SP	$q \leq 4$	$4 < Q \leq 35$
I	$q \leq 4$	$35 < Q \leq 1000$
L	$q \leq 4$	$Q > 1000$

1.5.5 Centaurs

In 1977, a small body was discovered orbiting the Sun between Saturn and Uranus (Kowal et al., 1979). It was named 2060 Chiron. Today we know that Chiron's orbit has a semi-major axis of about 13.65 au and that Chiron itself has a radius of at least 71 km (Groussin et al., 2004).

Its discovery was surprising because at that time no objects of this size were known to have orbits like this between giant planets. Chiron's discovery was followed in 1992 by the discovery of 5145 Pholus orbiting between Uranus and Neptune.

As time went on, more of these curious objects were found - 7066 Nessus in 1993, 8405 Asbolus in 1995 and 10199 Chariklo in 1997. It was soon realized that these bodies represented a new class of objects which orbit the Sun between Jupiter and Neptune. Today, we refer to such objects as Centaurs.

The Minor Planet Center defines a Centaur as a small body which has a semi-major axis between the orbits of Jupiter and Neptune and a perihelion distance greater than the semi-major axis of Jupiter[12]. Other definitions include

- comets with $T_J > 3$ and semi-major axes greater than that of Jupiter's (Levison, 1996; Duncan et al., 2004)

- small bodies with 5 au $< q < 28$ au and $a < 1,000$ au (Emel'yanenko et al., 2013).

This work adopts the definition of Centaur used by the Minor Planet Center. Applying this definition to a database of small bodies obtained from the Minor Planet Center shows that the number of objects classified as Centaurs stands at 223 [13], however, the actual population is believed to be much higher. Horner et al. (2004) estimate the real population of Centaurs with diameters larger than 1 km to be 44,300. Figure 1.9 shows the currently known Centaurs according to the Minor Planet Center in the HEBA scheme.

It is believed that Centaurs are a relatively short-lived transitional class of objects between KBOs and Jupiter-Family comets (Tiscareno & Malhotra, 2003). Small objects survive in the Centaur region on average for 10 Myr (Levison & Duncan, 1994; Tiscareno & Malhotra, 2003; Dones et al., 1996; Horner et al., 2004).

Since the Solar system is about 4.6 billion years old, the Centaurs we see today must have originated in another part of the Solar system. Thus, for their population to be maintained, they must have a replenishing source. Numerical studies show that the orbits of KBOs and SDOs can be perturbed by Neptune in such a way that their perihelia decrease until the objects transition into Centaurs (Duncan et al., 1988; Levison & Duncan, 1997; Volk & Malhotra, 2008).

SDOs in particular are a likely source of Centaurs (Di Sisto & Brunini, 2007). Other source populations include the Oort Cloud (Emel'yanenko et al., 2005; Brasser et al., 2012; de la Fuente Marcos & de la Fuente Marcos, 2014; Fouchard et al., 2014), Trojan populations of Jupiter (Horner et al., 2004), and Trojan populations of Neptune (Horner & Lykawka, 2010).

The lifetimes of Centaurs are punctuated by close encounters with the giant planets. These close encounters along with other orbital perturbations cause the osculating orbital parameters to change over time. Thus, the orbits of Centaurs are in a constant state of flux. The dynamical evolution of the orbits of Centaurs are complex, and the entire Centaur region is highly chaotic. Sometimes Centaurs can maintain a near constant perihelion while their semi-major axes and eccentricities change (Horner et al., 2003).

Numerical studies show that Centaurs exist in one of two dynamical classes (Tiscareno & Malhotra, 2003; Bailey & Malhotra, 2009). One type consists of those Centaurs whose proper semi-major axis changes in time according to a power law. These are referred to as random-walk Centaurs. The other type consists of Centaurs which abruptly jump between mean motion orbital resonances

---

[12]http://www.minorplanetcenter.net/iau/lists/Unusual.html (accessed Dec. 10, 2017).
[13]https://www.minorplanetcenter.net/iau/lists/t_centaurs.html (accessed Dec. 10, 2017).
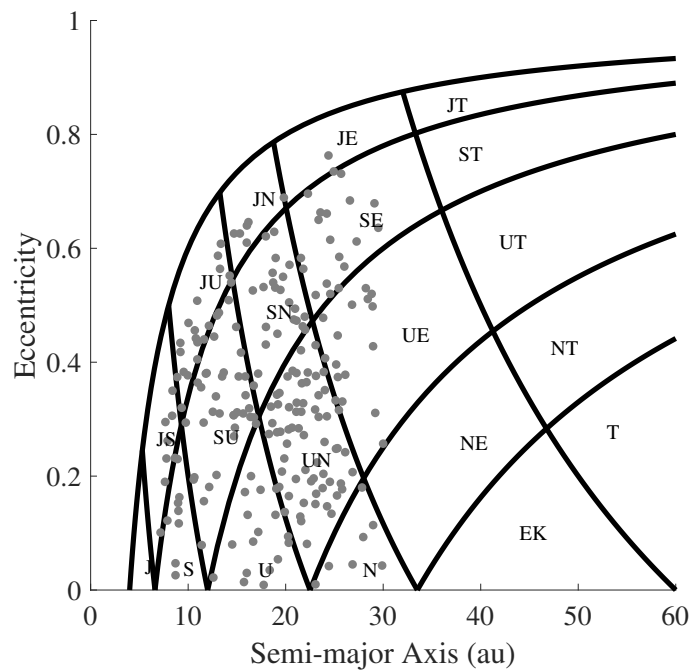
Figure 1.9: The currently known Centaurs in the HEBA scheme using $a - e$ data taken from the Minor Planet Center. Curves which extend from the lower left to the upper right are contours of constant perihelion. Curves which extend from the upper left to the lower right are contours of constant aphelion. The letters J, S, U and N stand for Jupiter, Saturn, Uranus and Neptune. T stands for Trans-Edgeworth-Kuiper Belt. E and EK stand for Edgeworth-Kuiper Belt.

of the four Jovian planets. Resonance sticking dominates the dynamics of these Centaurs throughout their lifetimes. These are called resonance hopping Centaurs. Numerical studies show that on average, resonance hopping Centaurs have longer dynamical lifetimes than random-walk Centaurs. Random-walk Centaurs are more likely to evolve into Jupiter-Family comets than resonance hopping Centaurs (Di Sisto & Brunini, 2007; Bailey & Malhotra, 2009).

Orbital perturbations can cause Centaurs to jump back and forth between different small body populations. Centaurs can transition into Jupiter-Family comets (Levison, 1996; Horner et al., 2004), then back into Centaurs, then back into Jupiter-Family comets again multiple times. Centaurs can collide with the Sun or a planet, be ejected from the Solar system entirely or even evolve into NEOs (Horner et al., 2004). The latter is of particular concern given that Centaurs are made mostly of volatile material and can be much larger than comet nuclei. If one of the larger Centaurs were to make it to the inner Solar system it would spread dangerously large amounts of debris capable of bombarding Earth and blocking sunlight (Hahn & Bailey, 1990; Napier et al., 2015). As a comparison, comet C/1995 O1, Hale-Bopp, one of the largest comets known, has a nucleus with a diameter of at most 35 km (Weaver & Lamy, 1997), but the largest Centaur known, Chariklo, has a diameter of about 250 km (Araujo et al., 2016).

1.6 The Effects of Planets on Small Bodies

In a general sense, planets perturb the orbits of small bodies. But more specifically planets produce three major effects on small body orbits. These effects are known as sculpting, shepherding and clustering.

Sculpting creates orbital gaps in groups of small body populations. The gaps can be seen as ranges in semi-major axis in which there are relatively few bodies compared to nearby orbits.

The cause of sculpting is a planet or planet(s) in mean motion resonances with the small body population. Examples of sculpting by planets include the Kirkwood gaps in the main asteroid belt (e.g. Kirkwood, 1867; Wisdom, 1983; Moons et al., 1998; Roig et al., 2002), gaps in the Kuiper Belt (Levison & Duncan, 1993) and possibly in the TNO region (Batygin & Morbidelli, 2017).

Sculpting can also be applied to satellites in mean motion resonances with ring particles about a planet. For example, the satellite Mimas of Saturn is in a 2:1 mean motion resonance with ring particles in the Huygens Gap at the inner edge of the Cassini division (French et al., 2016). And Saturn's moon Pan is in a 1:1 mean motion resonance with ring particles in the Encke gap (Spahn et al., 1993).

Sculpting has even been used to detect unseen exoplanets in protoplanetary discs by searching for gaps in the disc (Jang-Condell, 2017).

Shepherding constrains a group of small bodies to orbits with semi-major axes within a certain relatively narrow range and is the opposite of sculpting. One example is the Hilda asteroids in a 3:2 MMR with Jupiter (e.g. Schubart, 2007). The bodies are grouped around 3.97 au from the Sun as shown in Fig-

ure 1.7. Shepherding is also applied to satellites confining ring particles to a narrow semi-axis range. For example, Saturn's satellites Prometheus and Pandora shepherd particles in Saturn's F ring (Murray & Dermott, 1999; French et al., 2003).

Clustering is a grouping of the longitude of the ascending nodes and arguments of perihelion of small body orbits. Clustering has been used to infer the existence of the proposed Planet Nine (Batygin & Morbidelli, 2017).

1.7 Ringed Small Bodies

The field of ringed small bodies was born in 2013 by the serendipitous discovery of two narrow rings around the Centaur Chariklo which orbits between Saturn and Uranus (Braga-Ribas et al., 2014). Since then, rings have been detected around the TNO Haumea (Ortiz et al., 2017), and may exist around the Centaur Chiron (Ortiz et al., 2015). The existence of these ringed small bodies naturally raises several questions such as how did the rings form? Are ringed small bodies commonplace? And what is the longevity of such rings?

Explanations for the origin of rings around small bodies include an impactor (Melita et al., 2017), a collision between an orbiting satellite and another body (Melita et al., 2017), the tidal disruption of an orbiting satellite (El Moutamid et al., 2014), ejected debris from cometary activity (Pan & Wu, 2016) and the tidal disruption of the small body due to a close encounter between the small body and a giant planet (Hyodo et al., 2016).

The question of longevity becomes especially poignant in the Centaur region where close encounters between Centaurs and giant planets are common (Horner et al., 2004) and are quite capable of severely damaging or destroying such rings.

But even if rings could survive a close encounter with a giant planet, viscous forces should widen such rings on time scales such as hundreds of years (Michikoshi & Kokubo, 2017) or 100,000 years (Pan & Wu, 2016) which is far shorter than the typical $\sim$10 Myr lifetime of a Centaur (Tiscareno & Malhotra, 2003). However, the lifetime of rings could be extended by orders of magnitude due to stabilizing shepherd satellites (El Moutamid et al., 2014; Ortiz et al., 2015) or self-gravitating rings (Rimlinger et al., 2017).

If the body is active, then it could act as a replenishing source for rings thus also extending their lifetime. This idea is reasonable especially given the fact that some satellites of giant planets are known to be sources for ring material (e.g. Burns et al., 1999; Hedman et al., 2007). More evidence that rings can survive in the Centaur region comes from Araujo et al. (2016) who found that close encounters between Chariklo and a giant planet capable of severely damaging or destroying the rings are very rare.

This introduces the possibility that rings around Centaurs could pre-date their entrance into the Centaur region. This idea is bolstered by the discovery of a ring around the dwarf planet Haumea which lies in the Trans-Neptunian region (Ortiz et al., 2017). It is beneficial to study each of these three bodies and their rings in more detail.

1.7.1 Ring Detection

The rings of Saturn have been known since 1610 and can be seen from Earth in even small telescopes. However, rings around other bodies in our Solar system are too faint and/or too close to the body to be seen directly from Earth-based telescopes. These rings must be detected using a method which does not involve direct observation.

One method is to monitor the light intensity from a star as a body occults it. Then, as the rings around the body pass in front of the star, the rings block some of the star light causing a dip in the light curve.

Given the circular or elliptical shape of rings, any particular ring may cause up to two dips in the light curve. One dip occurs when the ring passes in front of the star, ahead of the small body. The second dip occurs after the small body has occulted the star when the part of the ring trailing behind the small body blocks some of the starlight. Viewing an occultation like this from different locations on Earth allows the shape of the small body to be inferred and the pole orientation to be estimated.

This technique was used to discover the rings of Uranus (Planetary Laboratory et al., 1978), the rings of Chariklo (Braga-Ribas et al., 2014) and possible rings around Chiron (Elliot, 1995; Bus, 1996; Ortiz et al., 2015). Figure 1.10 shows the light curve during the occultation of a star by Chariklo. The large dip in the center is caused by Chariklo itself. The other smaller dips are caused by rings.
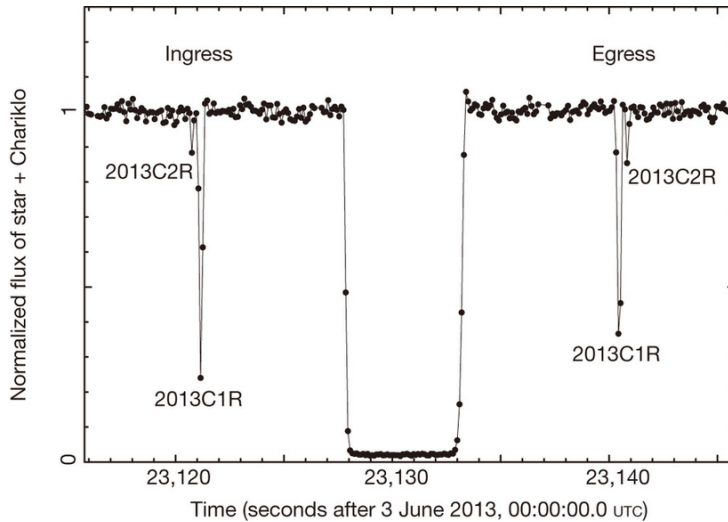
Figure 1.10: The light curve during the occultation of a star by Chariklo. The large dip in the center is caused by Chariklo itself. The other smaller dips are caused by rings. Taken from Braga-Ribas et al. (2014).

Valuable information can be gained by analysing light curves like the one

shown in Figure 1.10, but other factors must be considered before pertinent information can be gained. If the relative speed of the body is known, it can be used in conjunction with the time interval for a dip to determine a ring width.

A range of possible ring orbital radii can also be found. To do this, star occultation data can be analysed to determine the locations in the sky relative to the body at which the dips occurred. It is beneficial if the occultation is viewed from multiple locations as this can provide multiple data points. Simplifying assumptions can be made such as assuming the rings are circular and lie in the equatorial plane of the body.

Figure 1.11 shows the locations about Chiron in the sky at which dips in the light curve occurred during an occultation of a star. These locations can be fitted to a set of possible elliptical shapes. Assuming a circular shape of the rings, the elliptical shape is an illusion caused by projection. The elliptical shapes can be used to determine a range of possible ring orbital radii.
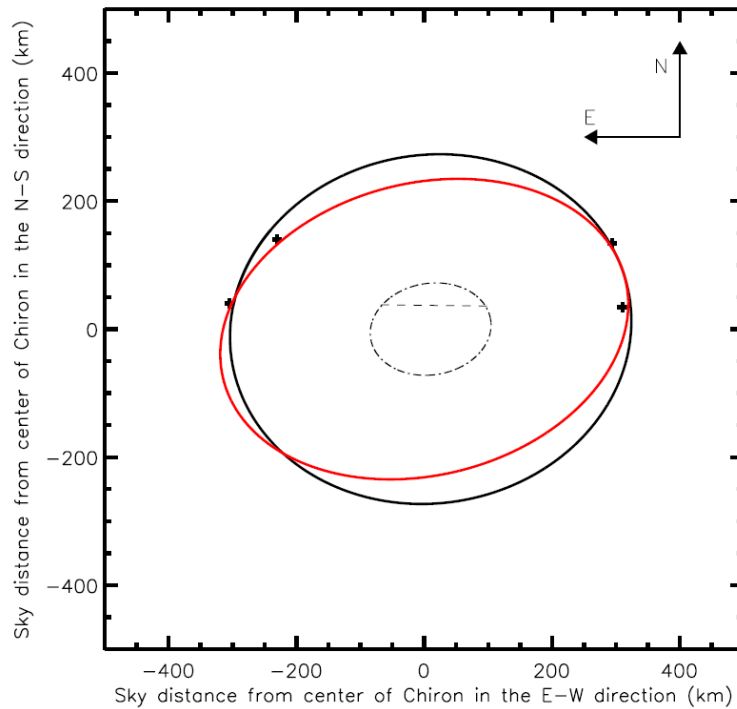
Figure 1.11: The locations about Chiron in the sky at which dips in the light curve occurred during an occultation of a star. The top two data points were found using the Faulkes telescope on Mount Haleakala. The two bottom points were found using the IRTF 3 m telescope at Mauna Kea. Image taken from (Ortiz et al., 2015).

Another important factor to consider when using this technique is the angle

at which the rings are being viewed. The aspect angle is defined as the angle between the rotation axis of the body and the line of sight direction of the observer. If the aspect angle is known or even if just its range is known, then this can be used to find possible coordinates of the poles of the body.

1.7.2 Chariklo

Chariklo is a Centaur orbiting between Saturn and Uranus with a semi-major axis of 15.8 au, an eccentricity of 0.172 and an inclination of 23.4°. Various values for the mean radius of Chariklo have been reported and range from 119 km (Fornasier et al., 2014) to 137 km (Altenhoff et al., 2001).

Chariklo is thought to have a non-spherical shape with an major to minor ellipsoid axis ratio of 1.1 (Fornasier et al., 2014). Its surface is believed to be composed of mostly refractory material and water ice (Groussin et al., 2004).

Chariklo's density is poorly known. Braga-Ribas et al. (2014) suggest a bulk density of 1 g/cm^3. Using this density and reported size range, this puts the mass of Chariklo somewhere in the range 10^{18} kg - 10^{19} kg assuming a spherical shape.

The ring structure of Chariklo consists of two separate rings. An inner ring of radius 391 km and width 7 km and an outer ring of radius 405 km and width 3 km. The rings are believed to be composed of mostly silicates with water ice, tholins and amorphous carbon (Duffard et al., 2002). At this time Chariklo is not believed to be active and no activity has been detected since its discovery. However, it is not known if Chariklo has been active in the past and thus acted as a replenishing source for its rings. A much more detailed description of Chariklo and its rings will be given in Chapter 2.

1.7.3 Chiron

Chiron's physical properties have been difficult to ascertain due to interference from circum-nuclear material, Chiron's non-spherical shape and cometary activity. Nevertheless, a concerted effort has been taken to obtain properties such as size, shape, and density (Fornasier et al., 2013; Ortiz et al., 2015). Proposed radii for Chiron range from 71 km to 186 km (Sykes & Walker, 1991; Groussin et al., 2004; Ortiz et al., 2015).

Chiron's bulk density cannot be established due to the large uncertainty in its size. A density range of 500 kgm^{-3} - 1,000 kgm^{-3} has been proposed for Chiron (Meech et al., 1997). Assuming a spherical body, this places the mass of Chiron somewhere on the order of 10^{17} kg - 10^{19} kg.

Chiron is believed to be porous and comprised of a mixture of dust and ices such as CN, CO, CO_2, and water ice (Stern, 1989; Luu & Jewitt, 1990; Meech & Belton, 1990; Bus et al., 1991; Prialnik et al., 1995; Womack & Stern, 1995; Capria et al., 2000).

Since its discovery, observers have reported sporadic outbursts or changes in brightness of Chiron perhaps related to cometary activity (Bus et al., 1988; Hartmann et al., 1988, 1990; Luu, 1993; Lazzaro et al., 1996, 1997; Bus et al.,

2001; Silva & Cellone, 2001; Duffard et al., 2002). In addition to sporadic changes in brightness, Chiron also displays periodic activity, reaching a peak about every decade. This may or may not be real (Luu & Jewitt, 1990; Luu, 1993; Lazzaro et al., 1996) but is unrelated to the rotation of Chiron, which has a period of only 5.92 hours (Bus et al., 1989).

This activity prompted an organised global program of observations to follow Chiron through its perihelion passage in the mid-1990s (Stern, 1995) and led to Chiron becoming the first object designated as both an asteroidal and cometary body (2060 Chiron) and 95P/Chiron[14].

Cometary activity is driven by the sublimation of volatiles. Within $\sim$2.5 au from the Sun, water sublimation typically dominates (Duncan et al., 1988; Quinn et al., 1990; Levison & Duncan, 1997; Meech & Svoren, 2004; Emel'yanenko et al., 2013). At greater heliocentric distances however, the temperature is too low for water to sublimate and so other volatile species drive the activity. Heliocentric distance is typically a strong driver of cometary activity for bodies on highly eccentric orbits as the body reaches maximum activity at perihelion and minimum activity at aphelion.

However, for cometary bodies in orbits of lower eccentricity, heliocentric distance does not drive the activity. For example, objects like 95/P Chiron and comet 29P/Schwassman-Wachmann 1 display sporadic outbursts of activity which occur well beyond perihelion and seemingly have nothing to do with heliocentric distance (Hartmann et al., 1988; Lazzaro et al., 1997; Duffard et al., 2002). Since Chiron has displayed activity at heliocentric distances where water ice cannot sublimate (Stern, 1989; Meech & Belton, 1990; Hartmann et al., 1990; Luu & Jewitt, 1990; Meech et al., 1997), other volatile sublimation must be responsible. One likely source of this activity is the outgassing of highly volatile ices such as CN, CO or CO_2 which escape due to thermal sublimation or the transformation of amorphous water ice to its crystalline form (Stern, 1989; Meech & Belton, 1990; Prialnik et al., 1995; Lazzaro et al., 1997; Capria et al., 2000).

After the discovery of rings around Chariklo, a reanalysis of star occultation data showed that the circum-nuclear material around Chiron could be interpreted as rings with a mean radius of 324 ± 10 km (Ortiz et al., 2015). A much more detailed description of Chiron and its rings will be given in Chapter 3.

1.7.4 Haumea

Haumea is a dwarf planet and is the most massive of the ringed small bodies having a mass of 4.006×10^{21} kg which is three orders of magnitude larger than the mass of Chiron or Chariklo. Its mass is better constrained due to Haumea's two moons named Hi'iaka and Namaka[15]. Its surface is believed to be comprised of water ice with a dark spot (Lacerda et al., 2008; Thirouin et al., 2016) and no atmosphere (Ortiz et al., 2017).

---

[14]http://www.minorplanetcenter.net/iau/lists/PeriodicCodes.html (accessed 23 Dec. 2016)
[15]https://planetarynames.wr.usgs.gov/Page/Planets#DwarfPlanets

The shape of Haumea is far from spherical, having a shape based on three axes known as a triaxial ellipsoid. The size of Haumea has been based on thermal models. One result for the length of its three axes is $2,000 \times 1,500 \times 1,000$ km (Rabinowitz et al., 2006). Ortiz et al. (2017) report that Haumea's major and minor axes have lengths of $1,704 \pm 4$ km and $1,138 \pm 26$ km respectively.

This shape is due to its very fast rotational period of 3.9 hours (Rabinowitz et al., 2006; Lacerda et al., 2008). Haumea's density is in dispute. Rabinowitz et al. (2006); Lellouch et al. (2010); Lockwood et al. (2014) and Thirouin et al. (2016) report a density of at least 2.5 g/cm^3 which is larger than a typical density of a TNO (Thirouin et al., 2016), though other TNOs such as 2002 GH$_{32}$ and 2003 UZ$_{413}$ have similar high densities (Perna et al., 2009; Thirouin et al., 2016). By contrast Ortiz et al. (2017) report an upper limit on Haumea's density of 1.885 g/cm^3 which if correct agrees more with other typical TNO densities.

The ring is believed to orbit in the equatorial plane of Haumea and exhibit 3:1 spin-orbit coupling with Haumea's rotation (Ortiz et al., 2017). The ring may be the result of a collision as Haumea is a member of the only known TNO collisional family though this is far from certain. Besides Haumea and its two moons, the family has ten other members (Rabinowitz et al., 2006; Thirouin et al., 2016). Tables showing the orbital and physical properties of Chariklo, Chiron and Haumea will be shown in Chapter Four.

1.8   Research Questions

In this thesis, three broad questions are addressed.

1.8.1   What is the likelihood that the rings of Chariklo could have formed before Chariklo entered the Centaur region?

This is addressed in Chapter 2. Nearly 36,000 Chariklo clones are integrated backwards in time for one Gyr under the influence of the Sun and the four giant planets. The close encounter distance for every close encounter between a clone and a giant planet is recorded. A scale to measure the severity of a close encounter based on close encounter distance is developed. Overall statistics of the close encounters, by planet, region and severity are taken. MEGNO and lifetime maps of a region of $a - e$ space containing the orbit of Chariklo are made.

1.8.2   What is the likelihood that any rings of Chiron could have formed before Chiron entered the Centaur region?

This is addressed in Chapter 3. The technique is very similar to that used for Chariklo. Nearly 36,000 clones of Chiron are integrated backwards in time for 100 Myr under the influence of the Sun and the four giant planets. The close encounter distance for every close encounter between a clone and a giant planet is recorded. The same scale used for Chariklo clones to measure the

severity of a close encounter is used for Chiron clones. Overall statistics of the close encounters, by planet and severity are taken. Statistics on the dynamical classes of a sample of clones are taken. MEGNO and lifetime maps of a region of $a - e$ space containing the orbit of Chiron are made.

1.8.3 How does the ring limit depend on the variables associated with a close encounter between a ringed small body and a planet?

This is addressed in Chapter 4. We use the criterion of Araujo et al. (2016) that the effect of a close encounter on a ring of a small body is just "noticeable" if the change in eccentricity of the orbit of any ring particle is 0.01. We define the ring limit as the distance of closest approach of a close encounter between a planet and a small ringed body in a parabolic or hyperbolic orbit about the planet in the planar, 3-body problem.

Close encounters between each giant planet and hypothetical one-ringed small bodies in parabolic or hyperbolic orbits about the planet are simulated using numerical integration, and the ring limit found for each trial. Ring particles are simulated using massless test particles initially in circular orbits which lie in the same plane as the orbit of the small body about the planet. For Jupiter, the ring limit is found for a range of small body masses, velocities at infinity of the small body and ring orbital radii.

For the other three giant planets, the ring limit is found for a Pluto-like body with a ring orbital radius of 50,000 km over a range of velocities at infinity. The large orbital radius was chosen so that a ring limit upper bound could be found which would cover a large range of possible orbital radii for ringed small bodies yet to be discovered.

2 The Dynamical History of Chariklo and its Rings

The field of ringed small bodies is only about four years old and is slowly growing. Since the discovery of rings around the Centaur Chariklo in 2013, rings have been found around the Trans-Neptunian Object (or TNO) Haumea and are suspected around the Centaur Chiron.

A natural question to ask based on these discoveries is what is the origin of these rings? At this time the origin of rings around small bodies is unknown. Also unknown is if all rings were created by the same mechanism or by different mechanisms. Theories of ring formation include cometary activity, collision with another body, collision between two satellites, tidal disruption of a satellite and tidal disruption of the body itself during a close encounter within the Roche limit of a planet.

The rings around Chariklo are the surprising given that its orbit exists in a region of the Solar system in which frequent close encounters with giant planets occur on time scales of thousands or even hundreds of years.

The severity of these encounters has consequences for ring origin theories. If close encounters within the tidal disruption distance are very common then this would support the idea that the rings originated in the Centaur region as any ring originating in the TNO region would likely have been destroyed by close encounters.

If close encounters within the Roche limit are found to be common then this would introduce the possibility that the rings could have been created in the Centaur region by tidal forces pulling particles off the small body which could then gather into rings.

On the other hand, if ring destroying close encounters are very rare, then this would introduce the possibility that the rings could have originated outside the Centaur region.

Because it was evident that past close encounters can have a strong impact on ring origin theories, it was natural to study these encounters in more detail in an attempt to measure their severity and frequency. But in order to accomplish this, a close encounter severity scale needed to be developed.

We noted the different factors that would affect the severity of close encounters such as the velocity at infinity, v_∞, of the small body, ring orbital radius, small body mass, planet mass, ring inclination and minimum separation distance d_{min}. We decided to ignore velocity effects and gauged the severity by comparing d_{min} to the critical distances of the Hill radius, tidal disruption distance, Roche Limit and "ring limit". The ring limit, R, was a curve in $d_{min} - v_\infty$ which separated noticeable encounters from non-noticeable encounters. That is, if $d_{min} < R$ then the encounter was noticeable and non-noticeable otherwise.

An encounter was considered just noticeable if given initially circular rings, the change in orbital eccentricity of any ring particle was 0.01. We accounted for the effect of ring inclination by defining the ring limit in the planar problem. Inclined rings are harder to perturb than rings in the plane of the small body's

orbit because eccentricity is altered only by planar perturbing forces. Perturbing forces normal to the orbital plane perturb the orbital inclination but not the eccentricity (Murray & Dermott, 1999). As such, defining the ring limit in this way ensured that ring inclination would not cause noticeable encounters to occur at distances beyond the ring limit.

We approximated R by setting it equal to 10 tidal disruption distances for each planet. This approximation partially accounted for the effects of small body mass, planet mass and ring orbital radius.

The severity scale was created and consisted of five different rankings for the severity of an encounter. In order of decreasing severity, encounters were classified as extreme, severe, moderate, low or very low. For example, if d_{min} was greater than the tidal disruption distance but less than the ring limit then this encounter was ranked as moderate. In this scale, close encounters of very low severity occurred outside the Hill radius.

The following work made use of our scale and the technique of numerical integration of clones of Chariklo backwards in time to determine the likelihood that ring destroying close encounters between Chariklo and any of the four giant planets have occurred in the past as well as the stability of Chariklo's present orbit, the chaoticity of the orbit, the region from which Chariklo originated and the time frame within which Chariklo entered the Centaur region. Each close encounter between a clone and a giant planet was recorded, and its severity determined using our scale.

The stability and chaoticity of Chariklo's current orbit were investigated by finding its dynamical lifetime and MEGNO parameter respectively. The half-life against leaving the Centaur region moving backwards in time was also found and used as a stability indicator.

The integrations were carried out, and the results analysed. Chariklo likely entered the Centaur region sometime during the last 20 Myr from somewhere in the Trans-Neptunian region. Close encounters within the tidal disruption distance or Roche limit were found to be extremely rare.

We concluded that it was statistically likely that Chariklo's rings could have originated in the Trans-Neptunian region assuming that the effects of viscous dispersion were negated by other stabilizing factors such as shepherd satellites. This also indicated that ring creation due to the tidal disruption of Chariklo during a close encounter was unlikely.

Chariklo's orbit was found to be highly chaotic but exhibited a degree of stable chaos. Its half-life against leaving the Centaur region moving backwards in time was found to be 3 Myr.

This work was published in the Astronomical Journal in 2017 with the title "The Dynamical History of Chariklo and its Rings" (Wood, J., Horner, J., Hinse, T. C., & Marsden, S. C. 2017, AJ, 153, 245). This published paper follows.

The Dynamical History of Chariklo and Its Rings

Jeremy Wood[1,2], Jonti Horner[2,3], Tobias C. Hinse[4,5], and Stephen C. Marsden[2]

[1] Hazard Community and Technical College, Community College Drive, Hazard, KY 41701, USA; jeremy.wood@kctcs.edu
[2] Computational Engineering and Science Research Centre, University of Southern Queensland, West Street, Toowoomba, QLD 4350, Australia
[3] Australian Centre for Astrobiology, UNSW Australia, Sydney, NSW 2052, Australia
[4] Korea Astronomy and Space Science Institute, 776 Daedukdae-ro, Yuseong-gu, Daejeon 305-348, Korea
[5] Armagh Observatory, College Hill, Armagh BT61 9DG, UK

Abstract

Chariklo is the only small solar system body confirmed to have rings. Given the instability of its orbit, the presence of rings is surprising, and their origin remains poorly understood. In this work, we study the dynamical history of the Chariklo system by integrating almost 36,000 Chariklo clones backward in time for 1 Gyr under the influence of the Sun and the four giant planets. By recording all close encounters between the clones and planets, we investigate the likelihood that Chariklo's rings could have survived since its capture to the Centaur population. Our results reveal that Chariklo's orbit occupies a region of stable chaos, resulting in its orbit being marginally more stable than those of the other Centaurs. Despite this, we find that it was most likely captured to the Centaur population within the last 20 Myr, and that its orbital evolution has been continually punctuated by regular close encounters with the giant planets. The great majority (>99%) of those encounters within 1 Hill radius of the planet have only a small effect on the rings. We conclude that close encounters with giant planets have not had a significant effect on the ring structure. Encounters within the Roche limit of the giant planets are rare, making ring creation through tidal disruption unlikely.

Key words: minor planets, asteroids: individual (10199 Chariklo) –
planets and satellites: dynamical evolution and stability – planets and satellites: rings

1. Introduction

The Centaurs are a dynamically unstable population of small bodies in the outer solar system. The first Centaur to be discovered, Chiron, was discovered in 1977. After the discovery, astronomers searched through archival images, revealing the presence of Chiron on old photographic plates, which allowed the object's orbit to be precisely determined. It was soon realized that Chiron followed an unusual path around the Sun, spending the vast majority of its time between the orbits of Saturn and Uranus (Kowal et al. 1979). In the decades since Chiron's discovery, many other Centaurs have been found, all following unstable orbits in the outer solar system. Though the definition of Centaur varies within the astronomical community, we will use the definition adopted by the Minor Planet Center that Centaurs move on orbits with semimajor axes between those of Jupiter and Neptune, and have perihelia beyond Jupiter's orbit[6] (e.g., Sheppard et al. 2000; Jewitt 2009). They exhibit extreme dynamical instability (e.g., Horner et al. 2004a; Bailey & Malhotra 2009), being scattered chaotically as a result of regular close encounters with the giant planets.

As a result of their extreme dynamical instability, the observed Centaurs cannot simply be the last remaining members of a once larger, primordial population. Instead, they must be continually replenished. Over the years, a number of other solar system small body populations have been suggested as potential sources for the Centaurs, including captured Oort Cloud comets (e.g., Emel'yanenko et al. 2005; Brasser et al. 2012; Fouchard et al. 2014), the Jovian Trojans (e.g., Horner & Evans 2006; Horner et al. 2012b), and the Neptune

Trojans (Horner & Lykawka 2010a, 2010b; Horner et al. 2012a).

The primary source population, however, seems likely to be the trans-Neptunian objects—principally the Scattered Disk (e.g., Di Sisto & Brunini 2007; Volk & Malhotra 2008), with a small contribution from the classical Edgeworth–Kuiper Belt (e.g., Levison & Duncan 1997). In turn, the Centaurs are thought to be the primary parent population for the short-period comets—with up to a third of Centaurs likely to be captured to that population at some point during their chaotic evolution (e.g., Horner et al. 2004a).

The largest known Centaur is Chariklo, with an estimated diameter of approximately 250 km (Fornasier et al. 2014). It moves on a moderately eccentric orbit between the orbits of Saturn and Uranus, with a semimajor axis of 15.8 au. Early dynamical studies showed that Chariklo moves on a relatively stable orbit for a Centaur, with an estimated dynamical half-life of 10.3 Myr (Horner et al. 2004a).

In 2013, observations of a chance stellar occultation by Chariklo revealed the unexpected presence of two narrow rings with radii 391 and 405 km, respectively—making it the only small body in the solar system confirmed to possess rings (Braga-Ribas et al. 2014).

The discovery of Chariklo's rings was a great surprise and has prompted significant discussion on their nature and origin, while also opening up the possibility that other small bodies such as Chiron could also possess rings (e.g., Ortiz et al. 2015; Pan & Wu 2016).

A variety of mechanisms have been proposed to explain the rings, including leftover debris from a collision with another small body, debris from the tidal disruption of another small body (El Moutamid et al. 2014), partial tidal disruption of Chariklo itself (Hyodo et al. 2016), and dust particles sent into

---

[6] http://www.minorplanetcenter.net/iau/lists/Unusual.html (accessed 2016 January 15).

orbit due to an outflow of CO and/or N_2 from Chariklo as a result of cometary activity (Pan & Wu 2016).

El Moutamid et al. (2014) suggest the possibility that shepherd satellites could exist around Chariklo, making the rings more stable. Such satellites are known to sculpt the rings of the giant planets—with several examples found in the Saturnian system alone (e.g., Colwell et al. 2009).

While such shepherding satellites have not yet been found in orbit around Chariklo, their presence would potentially ensure the long-term survival of the ring system.

The presence of rings around Chariklo is perhaps particularly surprising when one considers that the orbits of Centaurs are highly chaotic, as a result of the gravitational influence of the giant planets (Tiscareno & Malhotra 2003; Bailey & Malhotra 2009). On average, a Centaur remains just 10 Myr in the Centaur region (Levison & Duncan 1994; Dones et al. 1996; Tiscareno & Malhotra 2003; Horner et al. 2004a), which is far less than the age of the solar system (4.6 Gyr).

During their lifetime, Centaurs cross the orbits of the giant planets and most likely experience multiple close encounters within 1 Hill radius of those planets during their stay in the Centaur region (Tiscareno & Malhotra 2003; Bailey & Malhotra 2009; Araujo et al. 2016). This opens up the possibility that Chariklo has had a close encounter with a giant planet at some time in its past, which was so close that the rings as they exist today would not have survived.

The goal of this work is to determine the dynamical history of Chariklo and its rings, and to examine the chaoticity and lifetimes of Chariklo-like orbits in semimajor axis-eccentricity space. In Section 2, we present the known properties of Chariklo based on earlier observational work and introduce criteria that we will apply to measure the severity of a close encounter. In Section 3 we describe our methodology, before presenting our results in Section 4 and summarizing our conclusions in Section 5.

2. Chariklo Properties and Theory

Chariklo was discovered in 1997 by the Spacewatch program,[7] moving on an orbit that lies between those of Saturn and Uranus, within 0.09 au of the location of the 4:3 mean motion resonance with Uranus. Its physical properties and those of its rings are presented in Table 1. Orbital elements of Chariklo are shown in Table 2.

Since its discovery, a number of groups have carried out observations of Chariklo at a variety of wavelengths, with the goal of disentangling its surface composition. Despite the work that has been carried out, there remains significant disagreement on the Centaur's surface composition. Groussin et al. (2004) report that the reflectance spectrum of Chariklo is consistent with a surface composed of 80% refractory material and 20% water ice.

Guilbert et al. (2009) reported water ice in the combined spectrum of Chariklo+rings, and Duffard et al. (2014) showed that the water ice feature comes only from the rings, and not from Chariklo. The rings are believed to be composed of water ice, silicates, tholins, and some amorphous carbon (Duffard et al. 2014).

To date, no cometary activity has been detected for Chariklo, despite it passing through perihelion in the last decade. However, this does not rule out the possibility that it may

---

[7] http://spacewatch.lpl.arizona.edu/discovery.html (accessed 2016 October 29).

Table 1
Properties of Chariklo and Its Rings

Property	Value	Uncertainty
Radius (km)	137 (1)	10
	151 (2)	15
	118 (3)	6
	124 (4)	9
	125 (5)	
	119 (6)	5
Albedo	0.045 (7)	0.01
Composition	60% amorphous carbon	
	30% silicates	
	10% organics (8)	
	3% water ice (9)	
Inner ring width (km)	7 (4)	
Inner ring radius (km)	391 (4)	
Outer ring width (km)	3 (4)	
Outer ring radius (km)	405 (4)	
Ring composition	20% water ice	
	40%–70% silicates	
	10%–30% tholins	
	Small quantities of amorphous carbon (8)	

References. (1) Altenhoff et al. (2001), (2) Jewitt & Kalas (1998), (3) Groussin et al. (2004), (4) Braga-Ribas et al. (2014), (5) El Moutamid et al. (2014), (6) Fornasier et al. (2014), (7) Campins & Fernández (2000), (8) Duffard et al. (2014), (9) Brown & Koresko (1998).

Table 2
Orbital Elements of Chariklo Taken from the Asteroids Dynamic WWW[a] site for Epoch MJD 2,457,600.0 Based on an Observational arc of 9684.35 days

Element	Value ± Uncertainty (1-sigma)
Eccentricity	0.172265 ± 1.8036e–06
Semimajor axis	15.77739 ± 3.75e–05 au
Inclination	23.408508 ± 9.5473e–06 deg
Longitude of ascending node	300.38512 ± 2.9189e–05 deg
Longitude of perihelion	241.9872 ± 0.00014188 deg
Mean anomaly	65.9988 ± 0.00029106 deg

Note.
[a] http://hamilton.dm.unipi.it/astdys/ (accessed 2015 December 31).

---

have displayed cometary activity in the past (Guilbert et al. 2009).

Backwards integrations show that Chariklo has a backward half-life of 9.38 Myr, some 1.6 Myr longer than the next largest Centaur Chiron (Horner et al. 2004b).

2.1. The Stability of Rings through Close Encounters: The "Ring Limit" Criterion

The severity of a close encounter between a small body (such as Chariklo) and one of the giant planets has been shown to depend on the closest approach distance of the encounter, and the velocity of the small body at infinity (Araujo et al. 2008; Hyodo et al. 2016). In order to determine the dynamical history of Chariklo and its rings, we neglect velocity effects following Araujo et al. (2016) and compare the minimum close encounter distance between Chariklo and a

Table 3
A Scale Ranking the Close Encounter Severity between a Ringed Small Body and a Planet Based on the Minimum Distance Obtained between the Small Body and the Planet, d_{min}, during the Close Encounter, R_H, 10 R_{td}

Minimum Distance Range	Severity
$d_{min} \geqslant R_H$	Very Low
$10\,R_{td} \leqslant d_{min} < R_H$	Low
$R_{td} \leqslant d_{min} < 10\,R_{td}$	Moderate
$R_{roche} \leqslant d_{min} < R_{td}$	Severe
$d_{min} < R_{roche}$	Extreme

Note. R_{td} and R_{roche} are the Hill radius of the planet, $R = 10 \times$ tidal disruption distance, tidal disruption distance, and Roche limit, respectively (see text for details).

planet to three different critical distances within the Hill sphere of the planet. The first of these is the distance between Chariklo and a planet at which tidal forces can disrupt a Chariklo-ring particle binary pair instantaneously. This tidal disruption distance, R_{td}, for a binary consisting of a massless, outermost ring particle in a circular orbit and Chariklo is given by

$$R_{td} \approx r \left(\frac{3M_p}{m_{ch}} \right)^{\frac{1}{3}}, \qquad (1)$$

where M_p is the mass of the planet, m_{ch} is the mass of Chariklo, and r is the orbital radius of a ring particle (Agnor & Hamilton 2006; Philpott et al. 2010). When Chariklo is just within the tidal disruption distance to a planet, an outermost ring particle is just outside Chariklo's Hill sphere. According to Araujo et al. (2016) the minimum distance obtained between Chariklo and a planet during a close encounter must be $\leqslant 10\,R_{td}$ in order for the encounter to have a significant effect on the rings. We will refer to this distance as the "ring limit," R. They considered the effect "noticeable" if the maximum change in eccentricity of any orbiting ring particle was at least 0.01.

But there is one more critical distance to consider. At an even closer distance to a planet is the Roche limit—the distance within which a small body like Chariklo can be torn apart by tidal forces. For a small, spherical satellite of a planet, the equation for the Roche limit is (Murray & Dermott 1999)

$$R_{roche} \approx R_{ch} \left(\frac{3M_p}{m_{ch}} \right)^{\frac{1}{3}}, \qquad (2)$$

where R_{ch} is the physical radius of Chariklo.

Since closer approaches have a larger effect than more distant ones, the minimum distance, d_{min}, obtained between Chariklo and a planet during a close encounter can be used to assess severity.

We now present in Table 3 a severity scale based on d_{min} relative to the distances R_H, R, R_{td}, and R_{roche}.

3. Method

3.1. Chariklo

In order to determine whether Chariklo has experienced sufficiently close encounters with the giant planets to disrupt its rings during its life, we need to be able to determine its historical dynamical evolution.

To do this, we follow the same methodology as that used in previous studies of dynamically unstable objects (e.g., Horner

et al. 2004a; Horner & Lykawka 2010a; Kiss et al. 2013; Pál et al. 2015) and follow the evolution of a suite of clones of Chariklo backward in time for a period of 1 Gyr. By following the evolution of a large population of Chariklo clones, we can obtain a statistical overview of the object's potential past history.

As in those earlier works, we created a grid of test particles, centered on the best-fit solution taken from Table 2, by incrementing the semimajor axis, a, eccentricity, e, and inclination, i, of the test particles in even steps through the full $\pm 3\sigma$ uncertainty ranges in those elements. We held the three rotational orbital elements, argument of perihelion, longitude of ascending node, and mean anomaly constant across our population of clones.

Thirty-three massless test particles per orbital parameter were created for parameters a, e, and i to yield a total of $33^3 = 35{,}937$ test particles. Test particles were evenly spaced across the full uncertainty range of the orbital parameter.

The initial orbital elements of the four giant planets were found using the NASA JPL HORIZON ephemeris[8] for epoch 2000 January 1 at UT 00:00. Inclinations and longitudes for both Chariklo and the planets were relative to the ecliptic plane.

The planets were then integrated (within the heliocentric frame) to the epoch MJD 2,457,600.0—the epoch of the Chariklo clones using the *Hybrid* integrator within the MERCURY N-body dynamics package (Chambers 1999). Test particles and planets were then integrated backward in time for 1 Gyr in the 6-body problem (the Sun, four giant planets, and the test particle), subject only to the gravitational forces of the Sun and giant planets. This integration time is 100 times longer than the typical lifetime of a Centaur ($\sim$10 Myr). Therefore the conclusions presented in this study are limited to within this time span.

For the symplectic integration, we chose a time step of 40 days (Horner et al. 2004a, 2004b) corresponding to approximately 1% of the orbital period of Jupiter, the innermost planet at the start of our integrations, ensuring an accurate orbit calculation for the giant planets and the particle during non-close-encounter epochs (e.g., Tiscareno & Malhotra 2003).

We set the accuracy tolerance parameter for the switch-over integration algorithm to be 10^{-12}. This ensured an accurate integration of the test particle during epochs of high eccentricity excursions as a result of close encounters. A close encounter was said to have occurred when the distance between a test particle and a planet was $\leqslant$3 Hill radii. The time of every close encounter between a test particle and any planet was recorded, along with the instantaneous planet and test particle a–e–i elements and the minimum separation obtained between the test particle and planet, d_{min}.

Test particles were removed from the simulation by colliding with a planet, upon reaching a barycentric distance of 1000 au, achieving $e \geqslant 1$ or by approaching within 0.005 au of the Sun. Removal times were recorded.

Moving backward in time, the number of test particles in the Centaur region was assumed to decrease exponentially over some time interval according to the standard radioactive decay equation (Horner et al. 2004b):

$$N = N_o e^{-\lambda t}. \qquad (3)$$

Here, N_o is the initial number of test particles, N is the number of test particles remaining in the Centaur region at a time t, and λ is the decay constant. The decay constant can be found from the slope of the best-fit line of a graph of $\ln\left(\frac{N}{N_o}\right)$ versus time. Then the half-life, τ, is given by

$$\tau = \frac{-\ln(0.5)}{\lambda}. \qquad (4)$$

The data for the number of test particles remaining in the Centaur region at a time t were fit to Equation (3) to obtain the decay constant. Then Equation (4) was used to find the half-life.

The half-life gives a best first estimate to Chariklo's age as a Centaur—with 50% of the clones of Chariklo being ejected within that time period. We also used the half-life in Equation (3) to determine the time at which 99% of all Chariklo-like objects would have left the Centaur region.

3.2. The Severity of Close Encounters and the Mass of Chariklo

In order to gain an understanding of whether Chariklo's rings existed prior to its capture to the Centaur region, or are a more recent addition, we can investigate the times at which test particles had encounters with the planets that were sufficiently close to disrupt the rings.

If the great majority of clones were to experience even a few severe or greater disruptive encounters or a large number of low to moderate encounters, this would suggest that Chariklo's rings most likely formed in the relatively recent past.

On the other hand, if relatively few clones have encounters deep enough to disturb the rings, then it is clearly feasible that the rings could be primordial (and, equally, such infrequent close encounters might in turn suggest that any origin for the rings involving the tidal disruption of Chariklo or an ancient satellite seems unlikely).

We therefore examined the depths and timings of the close encounters between test particles and planets, and ranked the severity of each encounter using the scale in Table 3.

As Table 3 along with Equations (1) and (2) show, the severity of a close encounter depends in part on Chariklo's mass. This mass was estimated using the average density of Chariklo from Braga-Ribas et al. (2014) of 1000 kg m^{-3} and the radius value of 125 km from El Moutamid et al. (2014). A mass of 8.18×10^{18} kg was obtained. This calculation assumed that the shape of Chariklo was a perfect sphere, as it is nearly spherical with the major to minor axis ratio of 1.1 (Fornasier et al. 2014).

3.3. MEGNO and Lifetime Maps

In addition to our N-body integrations of Chariklo's orbital evolution, a complementary suite of calculations was performed to examine the wider dynamical context of Chariklo's orbit.

Since sampling very large regions of phase space is impractical with full-scale N-body integrations, we instead generated a MEGNO (mean exponential growth factor of nearby orbits; Cincotta et al. 2003) map for the region of phase space bound by $14\,\mathrm{au} \leqslant a \leqslant 19\,\mathrm{au}$ and $e \leqslant 0.8$ for Chariklo-like orbits. These are orbits that initially have the same orbital parameters as Chariklo, except for semimajor axis and eccentricity.

The resolution of the map was 1024×800 pixels. The map was constructed by integrating one test particle per pixel or 30,000 test particles total using the Gragg–Bulirsh–Stoer (Hairer et al. 1993) method.

The initial values of a and e for each test particle were determined by each location of a pixel on the map. The integration algorithm makes use of a variable step-size determined by a relative and absolute tolerance parameter, which were both set to be close to the machine precision. The total integration time for each particle in the a–e grid was 1 Myr.

MEGNO maps show the chaoticity of a region of a–e space by calculating a parameter $\langle Y \rangle$ that is proportional to the Lyapunov characteristic exponent at each point. The reader is referred to Cincotta & Simó (2000), Goździewski et al. (2001), Cincotta et al. (2003), Giordano & Cincotta (2004), and Hinse et al. (2010) for more details on MEGNO maps. For an explanation of Lyapunov characteristic exponents, the reader is referred to Whipple (1995).

$\langle Y \rangle$ will asymptotically converge toward 2.0 for quasi-periodic orbits and diverge from 2.0 for chaotic orbits as the system is allowed to evolve in time.

For this work, quasi-periodic orbits were color coded blue and highly chaotic orbits were coded yellow. Test particles were removed by following the same criteria as for the long-term integration described earlier in this work. In addition, we terminated a given integration when $\langle Y \rangle > 12$, which indicates a strong degree of chaos.

When a test particle was removed, the time of removal and the $\langle Y \rangle$ value were recorded. If a test particle survived the entire simulation, then its removal time was recorded as 1 Myr. A lifetime map was then generated in conjunction with the MEGNO map covering the same a–e grid space. In the lifetime map, shortest removal times were color-coded black and the longest with yellow.

4. Results

4.1. The Dynamical History of Chariklo

More than 70 million close encounters within 3 Hill radii were recorded, with roughly 7.1 million of these being at distances less than 1 Hill radius. The close encounters were analyzed using eight different subsets of the entire encounter data set. Five of those subsets examined close encounters, while the clone in question was a member of one of the solar system's various small body populations (detailed later), with the other three described as follows:

1. The set of first close encounters—a first close encounter is the earliest time chronologically at which a close encounter occurred. Each test particle had one and only one of these.
2. The set of close encounters at any time at which the test particle was classified as a Centaur. Each test particle had more than one of these.
3. The set of earliest close encounters chronologically (not necessarily a first close encounter) at which each test particle was classified as a Centaur. Each test particle had one and only one of these.

The subsets of close encounters based on the membership of the clone in a small body population when the close encounter occurred are described as follows:

Table 4
The Percentage of Close Encounters as a Function of Membership of the Different Small Body Populations Chariklo's Clones Occupied through the Course of the Integrations

Region	Percent
Inner SS	7
Comet	9
Centaur	53
TNO	31
Ejection	0.4

1. Inner SS—$a \leqslant a_J$.
2. Comet—$a > a_J$ and $q < a_J$.
3. Centaur—$a_J < a < a_N$ and $q > a_J$.
4. TNO—$a \geqslant a_N$.
5. Ejection—the test particle was being ejected from the solar system at the time of the close encounter.

Here, a is the semimajor axis of the test particle at the time of the close encounter, a_J is the semimajor axis of Jupiter, a_N is the semimajor axis of Neptune, and q is the perihelion distance of the test particle.

The percentage of close encounters that occurred when the test particle was in each of the five population subsets is shown in Table 4. The Centaur and TNO subsets dominate with 53% and 31% of the close encounters, respectively. This implies but does not prove that Chariklo entered the Centaur region from beyond Neptune.

To determine the dynamical history of Chariklo and if Chariklo did enter the Centaur region from beyond Neptune, three of the subsets were investigated.

First, analysis of the Centaur subset showed that the average time between consecutive close encounters within 3 Hill radii of a planet in the Centaur region was 8 kyr. Therefore, on Myr timescales, the earliest time chronologically of a close encounter of a test particle while classified as a Centaur was taken to be the approximate time of insertion of the test particle into the Centaur region.

The set of earliest close encounters chronologically in which each test particle was classified as a Centaur was used to determine the number of test particles in the Centaur region as function of time. These data were analyzed by fitting them to Equation (3), with time measured from the start date backward in time.

Figure 1 shows the decay of the number of test particles in the Centaur region moving backward in time. Note the reverse "s" shape of the graph. It took ∼1.0 Myr for the swarm of clones to disperse enough so that the decay could start to be exponential.

The exponential decay lasted from around 1.0 to 14.1 Myr ago. The best-fit line over the interval is shown as the straight line. The linear regression coefficient of the line was −0.998, which shows a strong anti-correlation.

Between 14.1 and 25 Myr ago, the decay proceeded more slowly and no longer strongly correlated to the best-fit line. This occurred because by that time many remaining test particles had evolved onto more stable orbits, which in turn took longer to decay.

From the slope of the best-fit line of −0.2346 Myr^{-1} and Equation (4), the half-life with respect to removal from the Centaur region was calculated to be ∼3 Myr. Since we expect half-lives with respect to removal from the Centaur region to be
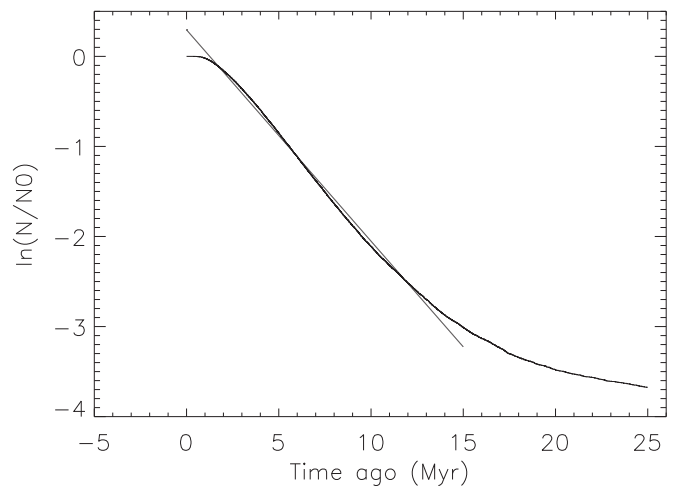
Figure 1. The decay of test particles from the Centaur region moving backward in time. The decay is exponential from 1.0 to 14.1 Myr ago. The straight line is the line of best fit over this time interval. It has a slope of −0.2346 Myr^{-1} and linear regression coefficient of −0.998. The slope was used to find the half-life of ∼3 Myr. At a time of 14.1 Myr ago, only 5.57% of the test particles were in the Centaur region. Note the backward "s" shape. The bin size is 1 kyr.
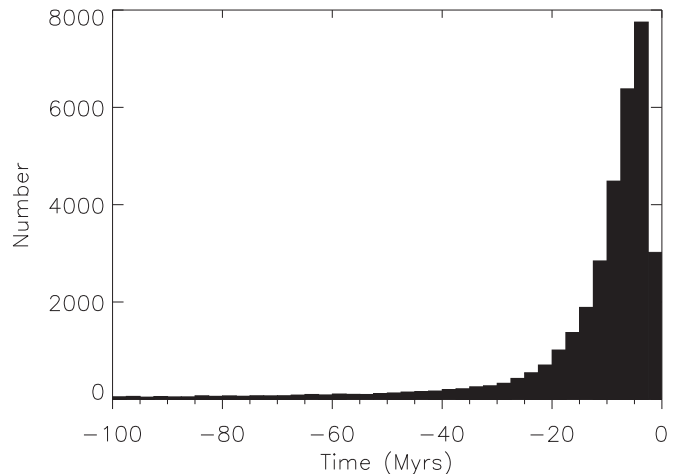
Figure 2. A histogram of the number of first close encounters over the last 100 Myr. The bin size is 2.5 Myr.

less than half-lives with respect to removal from the solar system, this value is in broad agreement with the work of Horner et al. (2004b), who found a backward integrated half-life of Chariklo with respect to removal from the solar system of 9.78 Myr.

Using the 3 Myr value for the half-life in Equation (3) suggests that there is a 99% probability that Chariklo was injected into the Centaur region at some time within the last 20 Myr.

Finally, once a likely time frame for injection into the Centaur region was established, the set of first close encounters was studied to determine from what region of the solar system Chariklo entered the Centaur region. Figure 2 shows a histogram of the number of first close encounters over the last 100 Myr.

Table 5 shows statistics on the first close encounters by region of the solar system. From the table it seems most likely that Chariklo entered the Centaur region from an orbit outside that of Neptune, perhaps from the Edgeworth–Kuiper Belt

Table 5
Statistics on the Set of First Close Encounters by
Small Body Population of the Solar System

Subset	Percent	Mean Time Ago (Myr)
Inner SS	2	15.7
Comet	21	12.1
Centaur	6	15.5
TNO	63	32.6
Ejection	8	31

Table 6
The Number of Close Encounters within 1 Hill Radius
by Planet and Population

Population	J	S	U	N
Inner SS	492255	1531	0	0
Comet	452415	139289	11879	6652
Centaur	56142	991571	2033886	717860
TNO	9026	224005	475861	1465906
Ejection	18687	9671	479	571

Note. Most close encounters occurred between the Centaur population and Uranus.

Table 7
The Hill Radii, Ring Limits, Tidal Disruption Distances, and
Roche Limits for Each Giant Planet (See Text for Details)

Planet	R_H (au)	R (au)	R_{td} (au)	R_{roche} (au)
J	0.3387	0.02400	0.002400	7.408×10^{-4}
S	0.4128	0.01606	0.001606	4.956×10^{-4}
U	0.4473	0.008584	0.0008584	2.649×10^{-4}
N	0.7704	0.009069	0.0009069	2.799×10^{-4}

Table 8
The Number and Percent of Close Encounters by Severity That Occurred
within 1 Hill Radius of Any Planet

Severity	Number	Percent
Low	7084469	100.0
Moderate	21953	0.0
Severe	1025	0.0
Extreme	239	0.0

(Horner et al. 2004b) or Scattered Disk (Duncan et al. 2004; Di Sisto & Brunini 2007). Two factors point to this conclusion:

1. The small percentage (2%) of the subset of first close encounters which were also members of the inner solar system subset makes it statistically unlikely that Chariklo was captured directly to the inner solar system from elsewhere (such as a long-period comet orbit, or the main asteroid belt) and then migrated outward to the Centaur population.
2. The much larger percentage (63%) and earliest chronological mean time of the subset of first close encounters that were also members of the TNO subset makes it statistically likely that Chariklo was a TNO before becoming a Centaur.

These dynamical results potentially complement the observed physical properties of Chariklo, which also suggest both an origin beyond the orbit of Neptune, and that the object has not spent a protracted period in the inner solar system.

First, the presence of volatiles on Chariklo's surface suggests that it has not spent lengthy periods interior to the solar system's ice-line, where most sublimation of volatile material occurs (Whipple & Sekanina 1979; Di Sisto et al. 2009; Brown et al. 2011).

Indeed, Levison & Duncan (1997) suggest that just 25 kyr in the inner solar system is enough to entirely devolatilize comets. However, it should be noted that Chariklo is significantly larger than the nuclei of short-period comets (Weissman & Lowry 2008)—and so could have potentially contained far more volatile material, and would therefore been able to survive a longer period of devolatilization. Still, the presence of volatiles does suggest an origin beyond the ice-line—and most likely beyond the orbit of Neptune.

Nevertheless, though the percentages of close encounters occurring in the inner solar system and Comet subsets are relatively small, they are not negligible.

This allows for the possibility that Chariklo could have been active for brief periods in its past, and its rings replenished by cometary activity. The only caveat is that Chariklo would have needed to migrate outward from such an orbit before its volatiles were extinguished. However, such inward and outward migrations are dynamically feasible (Horner et al. 2004a).

It should also be noted that for Chariklo to exhibit comet-like activity, it would not be necessary for the orbit to be in the inner solar system, as Centaurs beyond Jupiter are known to be active (Jewitt 2009).

To determine which planet dominated the close encounters in each population, the close encounters of each of the five population subsets were subdivided by planet. The results are shown in Table 6.

Uranus dominated the number of close encounters of the Centaur subset followed by Saturn, Neptune, and Jupiter. In the TNO subset, Neptune dominated, followed by Uranus, Saturn, and Jupiter. Thus, statistically, Neptune is most likely responsible for perturbing Chariklo into the Centaur region over time.

Jupiter dominated the number of close encounters of the other three subsets—Inner SS, Comet, and Ejection.

4.2. The Dynamical History of the Rings of Chariklo

The values of all ring limits, tidal disruption distances, and Roche limits are shown by planet in Table 7.

Jupiter had the largest value of R at 0.02400 au and Uranus the smallest at 0.008584 au. All values of R were well within 1 Hill radius of each planet by an order of magnitude or larger.

Thus to have a close encounter of at least moderate severity, it must be far closer than the size of the planet in question's Hill sphere—sufficiently close, in fact, that it would be placed within the domain of the regular satellites of that planet.

For example, to have a moderate close encounter with Jupiter, Chariklo would have to approach the giant planet at a distance similar to the orbital radius of Themisto, or roughly a factor of four times more distant from the planet than Callisto.

In other words, disruptive encounters require very close encounters, and hence might be expected to be relatively infrequent.

This hypothesis is well supported by our data, as can be seen in Tables 8 and 9. Every single clone of Chariklo experienced multiple close encounters; however, the great majority of these

Table 9
Severity of Close Encounters by Planet That Occurred
within 1 Hill Radius of Any Planet

Severity	J	S	U	N
Low	1012998	1360893	2520339	2190239
Moderate	14685	4884	1675	709
Severe	707	219	71	28
Extreme	135	71	20	13

Note. 99%, of close encounters were of low severity. Only 0.0034% of close encounters were of extreme severity.

approaches were relatively distant. Over 99% of all close encounters were outside the ring limit $R = 10\,R_{td}$ for the planet in question. Therefore we conclude that planetary close encounters have not played a major role in the disruption of rings.

Just 35% of the clones experienced at least one encounter within $10R_{td}$. Thus more than half of the clones never experienced even at least a moderate close encounter.

Furthermore, since only 0.0034% of the close encounters were extreme, it is unlikely (but still possible) that the rings were created by gaseous outflow during a close encounter (Hyodo et al. 2016), because this would require Chariklo to be closer to the planet than its Roche limit.

This theory of ring formation may be further put in doubt if the purported rings around Chiron (Ortiz et al. 2015) and the Saturnian satellites Rhea and Iapetus (Sicardy et al. 2016) are confirmed, because it would suggest that rings around small bodies are more common and are not formed by a very rare extreme close encounter.

It should be noted that no age of the rings of Chariklo can be stated with absolute certainty, since the total effects of gaseous outflow, shepherd satellites (if any), ring replenishment, and non-gravitational forces are unknown.

4.3. MEGNO and Lifetime Maps

The lifetime map in Figure 3 shows that the longest lifetimes for Chariklo-like orbits in the a–e region bound by $14\,\text{au} \leqslant a \leqslant 19\,\text{au}$ and $0 \leqslant e \leqslant 0.8$ lie mostly in the rectangle bound by $14\,\text{au} \leqslant a \leqslant 17.4\,\text{au}$ and $0 \leqslant e < 0.26$.

The effect of eccentricity on the lifetime can clearly be seen. In the range $0.26 \leqslant e \leqslant 0.55$, virtually no lifetimes of 1 Myr can be seen for any value of a. Orbits with $e > \sim 0.55$ have noticeably shorter lifetimes for nearly all a values, to as low as 0.01 Myr. We attribute this drop in lifetime to the crossing of Saturn's orbit.

The MEGNO map in Figure 3 shows that the entire region is dominated by highly chaotic orbits ($\langle Y \rangle \geqslant 5$).

Unlike lifetime, chaoticity does not display a clear relationship with eccentricity for constant a. Instead, relatively small islands of low chaoticity (quasi-periodic orbits) can be seen scattered about the region. The extent of their sizes might well depend on the initial phase angle of Chariklo. It is noteworthy that these islands lie in the same rectangle that contains nearly all of the most long-lived orbits seen in the lifetime map.

The orbits with relatively longer lifetimes and lower chaos are said to display stable chaos, and Figure 3 shows that Chariklo has one of these orbits.
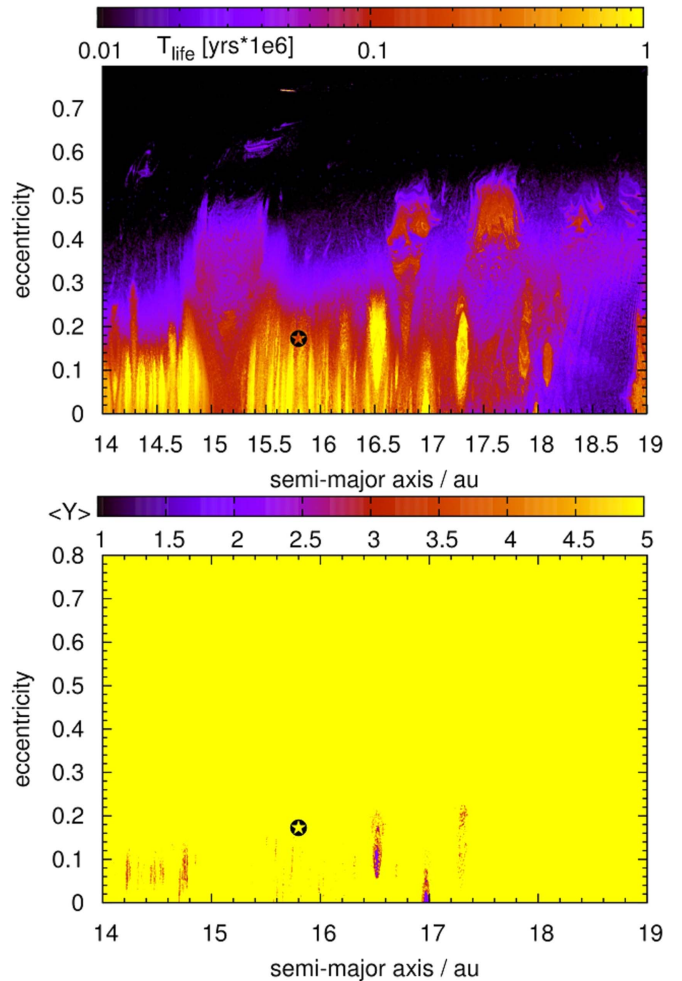
Figure 3. The lifetime map (top panel) and the MEGNO map (bottom panel) of Cariklo-like orbits. Chariklo is located at $a = 15.8\,\text{au}$ and $e = 0.172$, and is marked by the star. For the top panel, the longest lifetimes are shown in yellow and the shortest are shown in black, while for the bottom panel, highly chaotic orbits are shown in yellow and the least chaotic are shown in blue.

5. Conclusions

The dynamical history of Chariklo and its rings was determined using the technique of numerical integration of massless clones backward in time for 1 Gyr, and by recording close encounters between test particles and giant planets.

We find that Chariklo most likely originated in an orbit beyond Neptune and was likely captured into the Centaur population via perturbations from Neptune sometime within the last 20 Myr. The backward half-life with respect to removal of clones from the Centaur region is ~3 Myr, which is in good agreement with previous work on the backward half-life of Chariklo with respect to removal from the solar system.

Our results show that a small fraction of the clones of Chariklo spent some time significantly closer to the Sun than its current orbit. This suggests that it is possible but unlikely that Chariklo has undergone periods of cometary activity in its past —a result that mirrors the findings of Horner et al. (2004a) that Centaurs can experience multiple periods of cometary behavior throughout their lifetimes.

The critical distances of the Hill radius, tidal disruption distance, "ring limit" (defined as ten times the tidal disruption distance), and Roche limit were used to create a severity scale for close encounters based solely on the minimum distance

obtained between the test particle and planet during the encounter.

More than 99% of all close encounters over the course of our simulations were sufficiently distant so that no impact on the structure of Chariklo's rings would be expected. Indeed, just 35% of all clones experience an encounter within ring limit with one of the giant planets. In other words, 65% of clones never experience a sufficiently close encounter to significantly disrupt the ring system in a single pass. We conclude that planetary encounters have likely not played a major role in influencing the structure of the rings.

Close encounters in which the test particle crossed the Roche limit were extremely rare—making up just 0.0034% of the total sample of encounters observed. As result, we consider that it is highly unlikely that Chariklo's rings were created as a result of tidal disruption during such an encounter.

There is only a small chance that the rings have been replenished due to cometary activity in the inner solar system.

The lifetime of Chariklo-like orbits (orbits with different a and e) are found to be dependent on the eccentricity of the orbit, with a general trend that orbits with higher eccentricities have shorter lifetimes. The crossing of Saturn's orbit plays a strong role in reducing the lifetime of an orbit.

Nearly all Chariklo-like orbits in the region bounded by $14\,\mathrm{au} \leqslant a \leqslant 19\,\mathrm{au}$ and $0 \leqslant e \leqslant 0.8$ are strongly chaotic, with only relatively small islands in a–e space, which are less chaotic. Chariklo's orbit ($a = 15.8\,\mathrm{au}$, $e = 0.172$) displays stable chaos by having a very chaotic orbit in a region with a relatively longer lifetime compared with nearby Chariklo-like orbits.

Chariklo needs to be studied further to determine definitively if it shows evidence of past cometary activity. If it is ever proven that Chariklo was once active, it would support the idea presented here that in the past Chariklo could have had an orbit closer to the Sun where its rings could have been replenished.

References

Agnor, C. B., & Hamilton, D. P. 2006, Natur, 441, 192
Altenhoff, W. J., Menten, K. M., & Bertoldi, F. 2001, A&A, 366, L9
Araujo, R. A. N., Sfair, R., & Winter, O. C. 2016, ApJ, 824, 80
Araujo, R. A. N., Winter, O. C., Prado, A. F. B. A., & Vieira Martins, R. 2008, MNRAS, 391, 675
Bailey, B. L., & Malhotra, R. 2009, Icar, 203, 155
Braga-Ribas, F., Sicardy, B., Ortiz, J. L., et al. 2014, Natur, 508, 72

Brasser, R., Schwamb, M. E., Lykawka, P. S., & Gomes, R. S. 2012, MNRAS, 420, 3396
Brown, J. C., Potts, H. E., Porter, L. J., & Le Chat, G. 2011, A&A, 535, A71
Brown, M. E., & Koresko, C. C. 1998, ApJ, 505, 65
Campins, H., & Fernández, Y. 2000, EM&P, 89, 117
Chambers, J. E. 1999, MNRAS, 304, 793
Cincotta, P. M., Giordano, C. M., & Simó, C. 2003, PhRvD, 182, 151C
Cincotta, P. M., & Simó, C. 2000, A&AS, 147, 205
Colwell, J. E., Nicholson, P. D., Tiscareno, M. S., et al. 2009, in Saturn From Cassini-Huygens, The Structure of Saturn's Rings, ed. M. K. Dougherty et al. (Berlin: Springer), 375
Di Sisto, R. P., & Brunini, A. 2007, Icar, 190, 224
Di Sisto, R. P., Fernández, J. A., & Brunini, A. 2009, Icar, 203, 140
Dones, L., Levison, H. F., & Duncan, M. J. 1996, in ASP Conf. Ser. 107, Completing the Inventory of the Solar System, ed. T. W. Rettig & J. M. Hahn (San Francisco, CA: ASP), 233
Duffard, R., Pinilla-Alonso, N., Ortiz, J. L., et al. 2014, A&A, 568, A79
Duncan, M., Levison, H., & Dones, L. 2004, in Comets II, ed. M. Festou, H. U. Keller, & H. A. Weaver (Tucson, AZ: Univ. Arizona Press), 193
El Moutamid, M., Kral, Q., Sicardy, B., et al. 2014, in AAS/DDA Meeting 45 Abstracts, #402.05
Emel'yanenko, V. V., Asher, D. J., & Bailey, M. E. 2005, MNRAS, 361, 1345
Fornasier, S., Lazzaro, D., Alvarez-Candal, A., et al. 2014, A&A, 568, L11
Fouchard, M., Rickman, H., Froeschlé, C., & Valsecchi, G. B. 2014, Icar, 231, 99
Giordano, C. M., & Cincotta, P. M. 2004, A&A, 423, 745
Goździewski, K., Bois, E., Maciejewski, A. J., & Kiseleva-Eggleton, L. 2001, A&A, 378, 569
Groussin, O., Lamy, P., & Jorda, L. 2004, A&A, 413, 1163
Guilbert, A., Barucci, A., Brunetto, R., et al. 2009, A&A, 501, 777
Hairer, E., Nørsett, S. P., & Wanner, G. 1993, Solving Ordinary Differential Equations I, Vol. 8 (Berlin: Springer)
Hinse, T. C., Christou, A. A., Alvarellos, J. L. A., & Goździewski, K. 2010, MNRAS, 404, 837
Horner, J., & Evans, N. W. 2006, MNRAS, 367, L20
Horner, J., Evans, N. W., & Bailey, M. E. 2004a, MNRAS, 355, 798
Horner, J., Evans, N. W., & Bailey, M. E. 2004b, MNRAS, 354, 798
Horner, J., & Lykawka, P. S. 2010a, MNRAS, 405, 49
Horner, J., & Lykawka, P. S. 2010b, MNRAS, 402, 13
Horner, J., Lykawka, P. S., Bannister, M. T., & Francis, P. 2012a, MNRAS, 422, 2145
Horner, J., Müller, T. G., & Lykawka, P. S. 2012b, MNRAS, 423, 2587
Hyodo, R., Charnoz, S., Genda, H., & Ohtsuki, K. 2016, ApJL, 828, L8
Jewitt, D. 2009, AJ, 137, 4296
Jewitt, D., & Kalas, P. 1998, ApJL, 499, L103
Kiss, C., Szabó, G., Horner, J., et al. 2013, A&A, 555, A3
Kowal, C. T., Liller, W., & Marsden, B. G. 1979, in IAU Symp. 81, Dynamics of the Solar System (Dordrecht: Reidel), 245
Levison, H. F., & Duncan, M. J. 1994, Icar, 108, 18
Levison, H. F., & Duncan, M. J. 1997, Icar, 127, 13
Murray, C. D., & Dermott, S. F. 1999, Solar System Dynamics (Cambridge: Cambridge Univ. Press)
Ortiz, J. L., Duffard, R., Pinilla-Alonso, N., et al. 2015, A&A, 576, A18
Pál, A., Kiss, C., Horner, J., et al. 2015, A&A, 583, A93
Pan, M., & Wu, Y. 2016, AJ, 821, 18
Philpott, C. M., Hamilton, D. P., & Agnor, C. B. 2010, Icar, 208, 824
Sheppard, S., Jewitt, D., Trujillo, C., Brown, M., & Ashley, M. 2000, AJ, 120, 2687
Sicardy, B., El Moutamid, M., Quillen, A. C., et al. 2016, arXiv:1612.03321
Tiscareno, M., & Malhotra, R. 2003, AJ, 126, 3122
Volk, K., & Malhotra, R. 2008, ApJ, 687, 714
Weissman, P. R., & Lowry, S. C. 2008, MPS, 43, 1033
Whipple, A. L. 1995, Icar, 115, 347
Whipple, F. L., & Sekanina, Z. 1979, AJ, 84, 1894

3 The Dynamical History of 2060 Chiron and its Proposed Ring System

Chiron holds the distinction of being the first Centaur ever discovered. As time went on, it was found that Chiron was just one member of a class of objects orbiting between Jupiter and Neptune which today are known collectively as the Centaurs.

Though no other Centaurs besides Chariklo are known to have rings, the Centaur Chiron is the strongest candidate for the next ring-bearing Centaur as circum-nuclear material has been detected around it (Elliot, 1995; Bus, 1996).

Originally this material was interpreted as jets or jet-like structures, however, in light of the discovery of the rings around Chariklo, a reanalysis of star occultation data has given rise to the idea that the material could be interpreted as a ring structure (Ortiz et al., 2015).

That reanalysis suggests that, if the material is a ring, then its radius has the same order of magnitude as the rings of Chariklo $\sim 10^2$ km. If Chiron does indeed have rings, then this suggests the possibility that rings around small bodies might not be so rare. At this time it is not known how rare or commonplace rings around small bodies are.

Chiron is believed to have a less stable orbit than Chariklo (Horner et al., 2004). Though both objects orbit between Saturn and Uranus, only Chiron crosses the orbit of Saturn.

As with Chariklo, the severity and frequency of past close encounters of Chiron with each of the giant planets determines the likelihood that Chiron's rings could have formed outside the Centaur region.

As we did for Chariklo, we decided to investigate the close encounters of Chiron using the technique of numerical integration of clones backwards in time. The stability and chaoticity of Chiron's current orbit were investigated by finding its dynamical lifetime and MEGNO parameter respectively.

Each close encounter between a clone and a giant planet was recorded, and its severity determined using our scale. We found the half-life against backwards removal from the Centaur region by marking the time of the last close encounter of each clone in the Centaur region and fitting the number of remaining clones as a function of time to the radioactive decay equation. This half-life was then used as a stability indicator.

By analysing the severity and frequency of the close encounters, the possibility that Chiron's supposed ring could predate Chiron's entrance into the Centaur region was found. By marking the region of the Solar system which each clone entered moving backwards in time, we determined the likely region from which Chiron originated.

In addition, the likely dynamical class of Chiron was also determined by analysing the behavior of the semi-major axis in time for a sample of clones. The dynamical class of a Centaur can either be random-walk or resonance hopping. The dynamical class has ramifications for dynamical lifetime and sink population for the Centaur. Resonance-hopping Centaurs tend to have longer lifetimes than

random-walk Centaurs and are less likely to evolve into Jupiter-Family comets.

The integrations were carried out, and the results analysed. Chiron likely entered the Centaur region within the last 8.5 Myr from somewhere in the Trans-Neptunian region. Close encounters capable of destroying or severely damaging the rings were found to be so extremely rare that it is statistically likely that the rings of Chiron could have originated in the Trans-Neptunian region if the effects of viscous dispersion were negated by other stabilizing factors such as shepherd satellites.

The rings of Chiron were probably not created by the tidal disruption of Chiron itself due to the extreme rarity of close encounters within the Roche Limit. Chiron's half-life against leaving the Centaur region moving backwards in time was found to be 0.7 Myr, and the dynamical behavior of a sample of clones shows that Chiron is more likely a random walk Centaur than a resonance-hopping Centaur.

This work was published in the Astronomical Journal in 2018 with the title "The Dynamical History of 2060 Chiron and its Proposed Ring System" (Wood, J., Horner, J., Hinse, T. C., & Marsden, S. C. 2018, AJ, 155, 2). This published paper follows.

CrossMark

The Dynamical History of 2060 Chiron and Its Proposed Ring System

Jeremy Wood[1,2] , Jonti Horner[2,3] , Tobias C. Hinse[4] , and Stephen C. Marsden[2]

[1] Hazard Community and Technical College, 1 Community College Drive, Hazard, KY 41701, USA; jeremy.wood@kctcs.edu
[2] University of Southern Queensland, Computational Engineering and Science Research Centre, West Street, Toowoomba, QLD 4350, Australia
[3] Australian Centre for Astrobiology, UNSW Australia, Sydney, NSW 2052, Australia
[4] Korea Astronomy and Space Science Institute, 776 Daedukdae-ro, Yuseong-gu, Daejeon 305-348, Republic of Korea

Abstract

The surprising discovery of a ring system around the Centaur 10199 Chariklo in 2013 led to a reanalysis of archival stellar occultation data for the Centaur 2060 Chiron by Ortiz et al. One possible interpretation of that data is that a system of rings exists around Chiron. In this work, we study the dynamical history of the proposed Chiron ring system by integrating nearly 36,000 clones of the Centaur backward in time for 100 Myr under the influence of the Sun and the four giant planets. The severity of all close encounters between the clones and planets while the clones are in the Centaur region is recorded, along with the mean time between close encounters. We find that severe and extreme close encounters are very rare, making it possible that the Chiron ring system has remained intact since its injection into the Centaur region, which we find likely occurred within the past 8.5 Myr. Our simulations yield a backward dynamical half-life for Chiron of 0.7 Myr. The dynamical classes of a sample of clones are found. It is found that, on average, the Centaur lifetimes of resonance hopping clones are twice those of random-walk clones because of resonance sticking in mean motion resonances. In addition, we present MEGNO and chaotic lifetime maps of the region bound by $13\,\mathrm{au} \leqslant a \leqslant 14\,\mathrm{au}$ and $e \leqslant 0.5$. We confirm that the current mean orbital parameters of Chiron are located in a highly chaotic region of $a - e$ phase space.

Key words: minor planets, asteroids: individual (2060 Chiron) – planets and satellites: dynamical evolution and stability – planets and satellites: rings

1. Introduction

The study of small bodies of the solar system was changed forever in 1977, with the discovery of a large icy object moving on an orbit between those of Saturn and Uranus (Kowal et al. 1979). That object was subsequently named Chiron. It was soon realised that its orbit was dynamically unstable, with a mean half-life of 0.2 Myr, which is far shorter than the age of the solar system (e.g., Oikawa & Everhart 1979; Hahn & Bailey 1990). For more than a decade, 2060 Chiron was an oddity—but following the discovery of 5145 Pholus in 1992, a growing population of such objects in the outer solar system has been discovered—a population now known as the Centaurs.

Over the years, a number of different schemes have been proposed to define Centaurs (e.g., Horner et al. 2003; Elliot et al. 2005; Chiang et al. 2007; Gladman et al. 2008). Across all these schemes, it can be generally said that Centaurs have orbits between the giant planets Jupiter and Neptune. For this work, we follow the definition used by the Minor Planet Center, which considers objects to be Centaurs if they move on orbits with perihelia beyond the orbit of Jupiter and with semimajor axes within the orbit of Neptune.[5] Those objects in this region that are trapped in 1:1 resonance with one of the giant planets (the Trojans) are excluded from the list, and are not considered to be Centaurs. Using this definition, more than 220 objects can presently be classified as Centaurs.[6]

The Centaurs move on highly chaotic orbits that are frequently perturbed by the gravitational influence of the four giant planets. The strongest perturbations typically occur as a result of close approaches between the Centaurs and those planets (e.g., Marsden 1962; Horner et al. 2004b). The instability of the Centaur region is exemplified by the fact that Centaurs have dynamical lifetimes and half-lives much less than the age of the solar system, with values typically ≪100 Myr (Dones et al. 1996; Levison & Duncan 1997; Tiscareno & Malhotra 2003; Horner et al. 2004a; Di Sisto & Brunini 2007; Bailey & Malhotra 2009; Pál et al. 2015).

It is therefore clear that these objects are ephemeral in nature, and that their ranks must be replenished over time from other sources. Proposed source populations for the Centaurs include the Oort Cloud (Emel'yanenko et al. 2005; Brasser et al. 2012; de la Fuente Marcos & de la Fuente Marcos 2014; Fouchard et al. 2014), the Jupiter Trojans (Horner et al. 2004a; Horner & Wyn Evans 2006; Horner et al. 2012b), the Neptune Trojans (Horner & Lykawka 2010; Lykawka & Horner 2010; Horner et al. 2012a), the Scattered Disk (Di Sisto & Brunini 2007; Volk & Malhotra 2008), and other populations in the Edgeworth-Kuiper Belt (Levison & Duncan 1997; Volk & Malhotra 2008). Of these many source regions, it is thought that the majority of Centaurs originate within the Scattered Disk (Di Sisto & Brunini 2007; Volk & Malhotra 2008).

After these small bodies escape from one of the more stable source populations into the Centaur region, they will typically spend on the order of $\sim 10^6$ years as a Centaur before diffusing out of that region (Tiscareno & Malhotra 2003). The final fates of Centaurs are varied—some will collide with the Sun or one of the planets, or will be torn apart by tidal forces during a planetary close encounter, while others will be thrown onto orbits beyond Neptune or will be ejected from the solar system entirely (Noll 1994; Horner et al. 2004a; Volk & Malhotra 2008; Wood et al. 2016).

---

[5] http://www.minorplanetcenter.net/iau/lists/Unusual.html (accessed 2016 December 17).
[6] http://www.minorplanetcenter.net/iau/lists/t_centaurs.html (accessed 2017 October 8).

During the course of their evolution, studies have shown that at least one-third of the Centaurs will evolve onto cometary orbits with perihelia in the inner solar system (Horner et al. 2004b; Jewitt 2004; Bailey & Malhotra 2009). As such, the Centaurs are generally regarded as the principal parent population for the short period comets (Tiscareno & Malhotra 2003; Groussin et al. 2004; Horner et al. 2004a; Volk & Malhotra 2008; Bailey & Malhotra 2009; Jewitt 2009; Kovalenko et al. 2011).

Indeed, several Centaurs (including Chiron) have been observed exhibiting cometary activity (e.g., Jewitt 2009; Shi & Ma 2015; Wierzchos et al. 2017). Given the extreme dynamical instability exhibited by the Centaurs, coupled with the frequent close encounters they experience with the giant planets, the discovery in 2013 of a system of rings orbiting the Centaur 10199 Chariklo came as a huge surprise (Braga-Ribas et al. 2014). Those rings, revealed by unexpected dimmings of a star occulted by Chariklo prior to and immediately after the occultation event, are narrow and dense, and lie at radii of ∼391 and ∼405 km.

It is still unknown whether the rings formed recently, or pre-date Chariklo's injection into the Centaur region, though rings have also recently been discovered around the dwarf planet Haumea (Ortiz et al. 2017), which orbits beyond Neptune. This suggests that rings around small bodies could form in the Trans-Neptunian region.

Furthermore, a recent dynamical study has shown that such rings could readily survive with Chariklo through its entire evolution in the Centaur region, since sufficiently close encounters to disrupt the rings are rare (Wood et al. 2017).

The chance discovery of Chariklo's ring system prompted a reanalysis of stellar occultation data obtained for 2060 Chiron in 1993, 1994, and 2011 by Ortiz et al. (2015). The original analysis of that occultation data found dips in the light curve that, it was thought, corresponded to regions outside the nucleus, which were then interpreted as comet-like dust jets (Elliot et al. 1995; Bus et al. 1996) or symmetrical jet-like features (Ruprecht et al. 2015). The recent reanalysis of this data suggests that it might also be interpreted as evidence for a ring system similar to that of Chariklo, with a mean radius of 324 ± 10 km (Ortiz et al. 2015).

The origin of this proposed ring structure could be the result of a tidal disruption of Chiron due to a close encounter with a planet (Hyodo et al. 2016), a collision between Chiron and another body (Melita et al. 2017), a collision between an orbiting satellite and another body (Melita et al. 2017), the tidal disruption of an orbiting satellite (El Moutamid et al. 2014), or debris ejected from Chiron itself due to cometary activity (Pan & Wu 2016).

Over time, rings can widen due to viscous spreading (Michikoshi & Kokubo 2017). This process can occur on timescales as short as hundreds of years. However, the extent of the rings can be constrained, keeping them far more narrow, if shepherd satellites are present (French et al. 2003; Jacobson & French 2004; El Moutamid et al. 2014; Michikoshi & Kokubo 2017). At the present time no shepherd satellites are known to exist orbiting any Centaur, and hence their possible dynamical role will not be considered in this study.

Given the extreme dynamical instability exhibited by Chiron, it is interesting to consider whether its ring system could survive through the entirety of its life as a Centaur. If deep close encounters with the giant planets are sufficiently

Table 1
The Orbital Elements of Chiron for Epoch 2457600.5 JD

Property	Value	Units
a	$13.639500 \pm (1.48 \times 10^{-6})$	au
e	$0.38272700 \pm (9.62 \times 10^{-8})$	…
i	$6.947000 \pm (6.67 \times 10^{-6})$	deg
Ω	$209.21600 \pm (6.05 \times 10^{-5})$	deg
ω	$339.53700 \pm (6.19 \times 10^{-5})$	deg
M	$145.97800 \pm (2.97 \times 10^{-5})$	deg

Note. Based on an observational arc length of 44,305.9 days taken from the asteroids dynamic site (accessed 2015 December 31). Here, a is the semimajor axis, e is the eccentricity, and i is the inclination of the orbit. Ω, ω, and M are the longitude of ascending node, argument of perihelion, and mean anomaly, respectively. Each uncertainty is the standard deviation around the best-fit solution.

frequent, then it might be possible to place a constraint on the age of any rings around Chiron on the basis of its past dynamical history.

As a result, in this work, we follow Wood et al. (2017), and examine the dynamical history of Chiron and its proposed ring system. In doing so, we explore the likelihood that its rings could be "primordial" (i.e., could date back to before the object was captured as a Centaur) barring ring dispersal by viscous spreading. Our results also allow us to explore the likely source population of Chiron, and to confirm its status as one of the most dynamically unstable Centaurs.

In Section 2, we present the physical and orbital properties of 2060 Chiron. In Section 3, we discuss the means by which we can measure the severity of close encounters between ringed small bodies and planets, and in Section 4, we discuss the two dynamical classes that have been proposed for the Centaurs. We present our methodology in Section 5, and then present and discuss the results of our numerical integrations of Chiron in Section 6. Finally, in Section 7, we present our conclusions and discuss possible directions for future work.

2. The Properties of 2060 Chiron

2.1. Orbital Properties

After Chiron was discovered, pre-discovery images dating back as early as the late 19th century allowed its orbit to be well constrained (Liller et al. 1977; Kowal et al. 1979). It was soon found that the orbit of Chiron was unlike the orbit of any known small body at the time. Its aphelion lay between Saturn and Uranus, while its perihelion lay just interior to Saturn's orbit.

Since its discovery, more observations of Chiron have allowed its orbit to be even further refined. The current best-fit orbital properties of Chiron are shown in Table 1 and were taken from the Asteroids Dynamic site (Knezevic & Milani 2012).

Using the semimajor axis, a, and eccentricity, e, from Table 1, the perihelion and aphelion distances are found to be 8.4 au and 18.86 au, respectively. The semimajor axis is about 0.01 au away from the interior 5:3 mean motion resonance of Uranus located at about 13.66 au. The eccentricity of Chiron's orbit lies in the middle of the eccentricity range for the orbits of the known Centaurs, 0.01–0.73,[7] and is high enough to cause Chiron to cross the orbits of both Saturn and Uranus. These

---

[7] http://www.minorplanetcenter.net/iau/lists/Centaurs.html (accessed 2017 August 9).

giant-planet perturbations and close approaches have a significant effect on the dynamical evolution of Chiron's orbit (Oikawa & Everhart 1979; Scholl 1979; Kovalenko et al. 2002), which is reflected in the relatively short dynamical lifetime of ~1 Myr (Hahn & Bailey 1990; Horner et al. 2004a).

Furthermore, the half-life of its orbit is 1.03 Myr in the forward direction and 1.07 Myr in the backward direction (Horner et al. 2004a). Both times are much less than the age of the solar system.

The instability of Chiron's current orbit makes it highly unlikely that its orbit is primordial. Instead, the general consensus is that Chiron follows a chaotic orbit and originated in the Kuiper Belt (Oikawa & Everhart 1979; Hahn & Bailey 1990; Lazzaro et al. 1996; Silva & Cellone 2001; Duffard et al. 2002; Kovalenko et al. 2002).

Using the taxonomy of Horner et al. (2003), Chiron is classified as an object in the SU$_{\mathrm{IV}}$ class. This means that its dynamics are controlled by Saturn at perihelion and by Uranus at aphelion. The subscript IV means that the Tisserand parameter with respect to Saturn is >2.8 (Horner et al. 2003). The Tisserand parameter, T_p, is a quantity calculated from the orbital parameters of a small body and those of a planet it could encounter. It is defined by

$$T_p = \frac{a_p}{a} + 2\cos(i - i_p)\sqrt{\frac{a}{a_p}(1 - e^2)} \qquad (1)$$

(e.g., Murray & Dermott 1999). Here, a_p is the semimajor axis of a planetary orbit, i is the inclination of the small body orbit, and i_p is the inclination of the planetary orbit.

To first order, the Tisserand parameter of an orbit with respect to a given planet is expected to be conserved through an encounter with that planet, with the precise value giving an indication of the maximum strength of encounters that are possible with that planet.

Broadly, if $T_p > 3$, then particularly close encounters are not possible between the two objects, while for $2.8 \leqslant T_p \leqslant 3$, extremely close encounters can occur that might lead to the object being ejected from the solar system in a single pass (Horner et al. 2003).

2.2. Density, Size, and Mass

Unlike the relatively high precision with which the orbital parameters of Chiron are known, the physical properties remain much more poorly constrained. The diameter of Chiron has had to be estimated based on an assumed albedo. Though a strong effort to determine the size of Chiron has been made over the past 2 decades, efforts have been hampered by the interference from possible material located outside the nucleus, cometary activity, and Chiron's elongated shape (Fornasier et al. 2013; Ortiz et al. 2015).

Radius measurements ranging from 71 km (Groussin et al. 2004) to a constraint of <186 km (Sykes & Walker 1991) have been reported. Ortiz et al. (2015) report an overall average effective spherical radius of 90 km, which we adopt for this work.

Because of the large uncertainty in the size and mass of Chiron, Chiron's overall density is also poorly known. Meech et al. (1997), in their study of a coma around Chiron, report a bulk density in the range 500–1000 kg m^{-3}. Using a spherical radius of 90 km, this corresponds to a mass range of 1.53×10^{18} kg –3.05×10^{18} kg.

Table 2
A Scale Ranking the Severity of a Close Encounter between a Ringed Small Body and a Planet Based on the Minimum Distance Obtained between the Small Body and the Planet, $d_{\min}$, during the Close Encounter

$d_{\min}$ Range	Severity
$d_{\min} \geqslant R_{\mathrm{H}}$	Very low
$R \leqslant d_{\min} < R_{\mathrm{H}}$	Low
$R_{\mathrm{td}} \leqslant d_{\min} < R$	Moderate
$R_{\mathrm{roche}} \leqslant d_{\min} < R_{\mathrm{td}}$	Severe
$d_{\min} < R_{\mathrm{roche}}$	Extreme

Note. R_{H}, $R = 10R_{\mathrm{td}}$, R_{td}, and R_{roche} are the Hill radius of the planet with respect to the Sun, ring limit, tidal disruption distance, and roche limit, respectively.

3. Measuring the Severity of Close Encounters with Planets

Currently it is unknown what role, if any, the sporadic activity of Chiron played in the formation of any ring structure around the body. Rings could have formed either before or after Chiron entered the Centaur region. But given that Chiron presently lies in a chaotic and unstable orbit prone to planetary close encounters, it is of interest to determine the likelihood that such encounters could severely damage or destroy any orbiting ring structure.

To accomplish this, a method to gauge the severity of such an encounter is needed. Primarily, the severity of a close encounter between a ringed small body and a planet is determined by the minimum approach distance between the small body and planet, $d_{\min}$.

If the small body is in a parabolic or hyperbolic orbit relative to the planet (it has not been captured as a satellite), then the velocity at infinity of the small body relative to the planet also plays a role in determining the encounter severity, albeit to a lesser extent than the depth of the encounter.

Wood et al. (2017) ignored velocity effects and developed a severity scale based on $d_{\min}$ relative to the Hill radius, R_H; tidal disruption distance, R_{td}; the ring limit, $R = 10R_{\mathrm{td}}$; and the Roche limit, R_{roche}. This scale is shown in Table 2.

The Hill radius defines a sphere of influence centered on a secondary body of mass m_s in an orbit with orbital radius R_{radial} around a primary body of mass M_p in the planar problem. The Hill radius is approximately given by

$$R_H \approx R_{\mathrm{radial}}\left(\frac{m_s}{3M_p}\right)^{\frac{1}{3}} \qquad (2)$$

(e.g., Murray & Dermott 1999). For non-circular orbits, R_{radial} is approximated using the semimajor axis of the orbit. Loosely defined, the Hill radius is the distance around a secondary body (relative to a primary body) within which satellites can orbit without their orbits being completely disrupted by tidal forces due to the primary body. In the case where the secondary body is a planet and the primary body the Sun, it is found that all known planetary satellites follow this rule, being contained well within the Hill spheres of their host planets. For other objects moving in the system, the Hill radius of a planet can be used to indicate the region of space around its orbit, into which other objects move at their peril.

Typically encounters at a distance greater than ~3 Hill radii will have only a limited effect on the long-term stability of an object, while orbits that approach within this distance are

typically dynamically unstable, unless close approaches are prevented by mutual mean motion resonances between the objects concerned (e.g., Williams & Benson 1971; Malhotra 1995; Horner et al. 2011; Robertson et al. 2012; Wittenmyer et al. 2012).

The ring limit is a relatively new critical distance introduced by Araujo et al. (2016) and used by Wood et al. (2017) to examine the stability of Chariklo's ring system against close encounters. It is loosely defined as lying at 10 tidal disruption distances from a given planet, and represents an upper limit on the minimum approach distance for close encounters for which the effect on a ring of a minor body is just noticeable (meaning the maximum change in orbital eccentricity of the orbit of any ring particle = 0.01). Here we apply the ring limit to study the influence of close encounters between Chiron and the giant planets.

Given a typical solar system small body, the tidal disruption distance, R_{td}, lies well within the Hill radius for a given planet. When the separation between a small body and a planet is closer than R_{td}, a secondary body-satellite binary pair of total mass $m_s + m_{sat}$ and semimajor axis a_B can be permanently disrupted by tidal forces in one pass. It should be noted in passing that as defined in this manner, the ring limit and tidal disruption distances have no meaning for close encounters between planets and small bodies with no rings or satellites.

R_{td} can be approximated as the secondary-primary body separation at which a satellite orbiting the secondary body would lie at the outer edge of the secondary body's Hill sphere. R_{radial} in Equation (2) is then by definition R_{td}, and R_H is approximated by a_B. Solving for R_{td} yields

$$R_{td} \approx a_B \left(\frac{3M_p}{m_s + m_{sat}} \right)^{\frac{1}{3}} \qquad (3)$$

(e.g., Philpott et al. 2010). Closer still to the primary body, the Roche limit is the distance from the primary within which a secondary body held together only by gravity would be torn apart by tidal forces. For a rigid secondary body, the equation for the Roche limit with respect to a primary body is approximately

$$R_{roche} = 2.44 R_p \left(\frac{\rho_p}{\rho_s} \right)^{\frac{1}{3}} \qquad (4)$$

(Roche 1849; Murray & Dermott 1999). Here, R_p is the physical radius of the primary body, ρ_p is the density of the primary body, and ρ_s is the density of the secondary body.

Now that a severity scale for close encounters has been established, it can be used to study simulated close encounters between ringed Centaurs and the giant planets.

4. The Two Dynamical Classes of Centaurs

Throughout its lifetime as a Centaur, the frequency and severity of close encounters between Chiron and the giant planets will affect the stability of any ring structure around Chiron. The frequency of close encounters can be affected by a Centaur's so-called dynamical class.

Previously it was shown that small bodies including Centaurs can be classified based on their perihelion, aphelion, and Tisserand parameter (as detailed in Horner et al. 2003).

However, as Bailey & Malhotra (2009) showed, Centaurs may also be classified into one of two classes based on their long-term dynamical behavior. The first type consists of those Centaurs that randomly wander from orbit to orbit. The semimajor axes of these Centaurs' orbits increase and decrease in time with no particular pattern. These Centaurs are known as random-walk Centaurs.

Centaurs of the other type spend most of their time temporarily trapped in mean motion resonances of the giant planets and typically jump from one resonance to the other. A small body is in a mean motion orbital resonance with a planet if the ratio of the orbital period of the planet to the orbital period of the small body equals a ratio of two small integers (Murray & Dermott 1999).

Becoming temporarily trapped in a resonance is a behavior known as resonance sticking (Lykawka & Mukai 2007). While trapped in a resonance, the semimajor axes of these Centaurs' orbits oscillate about a constant value which corresponds to the resonance location. These Centaurs are known as resonance hopping Centaurs. Since it is possible that resonance sticking can protect small bodies from close encounters with planets (Malhotra 1995), the dynamical class of a Centaur can have consequences for any ring structure around it.

The two types can also be more rigorously defined mathematically. As the semimajor axes of random-walk Centaurs wander aimlessly and those of resonance hopping Centaurs remain more constant, we would expect that on average the standard deviation of semimajor axis values of random-walk Centaurs would increase in time more predictably than those of resonance hopping Centaurs.

Mean standard deviation, then, can be used as a tool to distinguish between the two dynamical types. Random-walk Centaurs are those Centaurs whose mean square standard deviation of semimajor axis, $\langle \sigma^2 \rangle$, varies as a power law in time. It is said that these Centaurs display generalized diffusion. This can be expressed mathematically as

$$\langle \sigma^2 \rangle = Dt^{2H}. \qquad (5)$$

Here, t is time, D is the generalized diffusion coefficient, and H is the Hurst exponent with $0 < H < 1$. Random-walk Centaurs can then be generally defined as those Centaurs for which the semimajor axis behavior is well described by generalized diffusion. Conversely, it then goes that the behavior of the semimajor axis of resonance hopping Centaurs is not well described by generalized diffusion.

Centaurs of both types may also display both random walking and resonance sticking during their lifetime. To determine if a Centaur is in fact trapped in a particular mean motion resonance, care must be taken.

Resonances do not exist at a single point but have widths in phase space. For example, for any particular resonance, a Centaur can be trapped in the resonance over a range of semimajor axis values.

To positively determine if a small body is trapped in a resonance, two behaviors must be displayed. First, the semimajor axis of the small body orbit must oscillate about the resonance location, and second, the primary resonance angle must librate in time (Smirnov & Shevchenko 2013).

The primary resonance angle is defined by $p\lambda - q\lambda_p - (p - q)\bar{\omega}$, where p and q are integers, λ_p is the mean longitude of the planet's orbit, λ is the mean longitude of the small body's orbit, and $\bar{\omega}$ is the longitude of perihelion of the small

body's orbit (Murray & Dermott 1999; Roig et al. 2002; Bailey & Malhotra 2009; Smirnov & Shevchenko 2013).

This angle is related to the perturbation of the orbit of a small body around a central body (like the Sun) by a third body (like a planet) in the planar 3-body problem. The reader is referred to Murray & Dermott (1999) for details.

5. Method

To study the dynamical history of Chiron and its ring system, a suite of numerical integrations were performed using the *n*-body dynamics package MERCURY (Chambers 1999).

A total of 35,937 massless clones of Chiron were integrated backward in time for 100 Myr in the six-body problem (Sun, four giant planets, and clone). The integration time is justified, as it is at least 100 times longer than the approximate half-life of Chiron (Hahn & Bailey 1990; Horner et al. 2004a).

The orbital elements of the individual clones were chosen from a range of three standard deviations below to three standard deviations above the accepted value of each orbital parameter of Chiron for epoch 2457600.0 JD taken from the Asteroid Dynamic Site (Knezevic & Milani 2012).

To create our cloud of clones for Chiron, we varied each of the orbital elements as follows. First, we sampled the $\pm 3\sigma$ uncertainty range in semimajor axis, a. We tested 11 unique values of the semimajor axis, ranging from $a - 3\sigma$ to $a + 3\sigma$, in even steps. At each of these unique semimajor axes, we tested 11 orbital eccentricities, which were again evenly distributed across the $\pm 3\sigma$ uncertainty in that variable. At each of these $121\,a - e$ pairs, we tested 11 unique inclinations also evenly spaced in the range $\pm 3\sigma$. This gave a grand total of 1331 potential $a - e - i$ combinations for Chiron. At each of these values, we tested 27 unique combinations of Ω, ω, and M, creating a $3 \times 3 \times 3$ grid in these three elements. The three values chosen for each of these three variables were the best-fit solution, and the two values separated by 3σ from that value. In total, this gave us a sample of 35,937 unique orbital solutions for Chiron.

The time step was chosen to be 40 days, which is approximately one-hundredth of an orbital period of Jupiter —the innermost planet included in this study. Similar time steps have been used before in integrations of both Centaurs and Main Belt asteroids (Tsiganis et al. 2000; Tiscareno & Malhotra 2003).

Clones were removed from the simulation upon colliding with a planet, colliding with the Sun, achieving an orbital eccentricity $\geqslant 1$, or reaching a barycentric distance >1000 au.

The masses and initial orbital elements of the four giant planets were found using the NASA JPL HORIZON ephemeris[8] for epoch 2451544.5 JD. Inclinations and longitudes for both Chiron and the planets were relative to the ecliptic plane.

In order to set their starting orbital parameters for the simulation, the planets were integrated (within the heliocentric frame) to the epoch 2457600.0 JD—the epoch of the Chiron clones using the *Hybrid* integrator within the MERCURY *n*-body dynamics package (Chambers 1999). The accuracy parameter was set to 1.d-12, and the hybrid handover radius was set to 3 Hill radii.

Table 3
Some Different Small Body Populations of the Solar System

Name	Definition
Inner SS	$a \leqslant a_J$
SP Comet	$a > a_J$ and $q < a_J$
Centaur	$a_J < a < a_N$ and $q > a_J$
TNO	$a \geqslant a_N$
Ejection	$e \geqslant 1$

Note. Here, a is the semimajor axis of the clone during the close encounter. The semimajor axis and other orbital values of the clone's orbit just before the close encounter were not recorded. a_J and a_N are the semimajor axis of Jupiter and Neptune, respectively; and q is the perihelion distance of the clone. Inner SS means inner solar system, SP comet means short period comet, TNO means trans-Neptunian object, and ejection means the clone was being ejected from the solar system at the time of the encounter.

Statistics on the close encounters were then taken by small body population of the solar system membership of the clone at the time of the encounter and by encounter severity. The different small body populations of the solar system used are defined in Table 3.

Physical properties of the planets were taken from NASA.[9] The mass of the Sun was also taken from NASA.[10] For Chiron we selected a bulk density of 1000 kg m^{-3}, which along with our selected radius of 90 km yielded a mass of 3.05×10^{18} kg. This mass was used in Equation (3) to determine the tidal disruption distance between Chiron and each planet. The density was used in Equation (4) to determine the Roche Limit between Chiron and each planet.

5.1. Determining the Half-life and Origin of Chiron

To determine the likely origin of Chiron, the chronologically earliest close encounter with a giant planet was analyzed for each clone, and the small body population of which the clone was a member at the time of the close encounter was found using the orbital parameters of the clone's orbit at the time of the encounter.

This then allowed the fraction of injection events from the various small body populations shown in Table 3 to be determined. (In other words, it allowed us to determine the likely source population of Chiron.)

Note that Trojans could overlap with the Centaur small body population the way we have defined it. However, in order to have a close encounter, a small body must have already exited the Trojan region.

Furthermore, though the Jupiter and Neptune Trojans are possible feeder populations to the Centaurs (e.g., Horner & Wyn Evans 2006; Horner & Lykawka 2010), our study is unable to yield any information on the likelihood of either of these being the source of Chiron. Therefore Trojans were omitted as separate populations in Table 3.

To determine the half-life of Chiron against removal from the simulation moving backward in time, the number of clones remaining at a time t was recorded as a function of time throughout the entire integration. Given N_o as the initial number of clones at a time $t = 0$, the half-life can be determined by fitting the data to the standard radioactive decay

---

[8] https://ssd.jpl.nasa.gov/horizons.cgi?s_body=1#top (accessed 2015 December 31).

[9] https://ssd.jpl.nasa.gov/?planet_phys_par (accessed 2017 June 16).
[10] https://nssdc.gsfc.nasa.gov/planetary/factsheet/sunfact.html (accessed 2017 June 17).

equation,

$$N = N_o e^{\frac{-0.693}{\tau}t}, \qquad (6)$$

where τ is the half-life. The time interval over which the decay of clones was exponential was obtained by the fit of the data to Equation (6). Then the fit was used to calculate the half-life.

Once the half-life was determined, it was used in Equation (6) to determine the time at which 99.99% of clones would be removed from the simulation assuming a constant half-life. This time was then set as the upper limit on the time at which Chiron entered the Centaur region.

5.2. Finding the Dynamical Class

A separate set of integrations was made using the IAS15 integrator in the REBOUND n-body simulation package (Rein & Liu 2012; Rein & Spiegel 2015) using the orbital values from a set of 1246 Chiron clones from the previous integrations.

Three different samples of clones of ~400 clones each were used—the first sample was taken from the first 1000 clones, the second from the middle 1000 clones, and the third from the last 1000 clones in the entire data set. The middle sample included the currently accepted orbital values of Chiron.

It was not necessary to find the dynamical class of every clone, since the objective of these integrations is to compare and contrast the two dynamical classes and to explore specific examples of the behavior of clones in each class. Just a sampling of clones is sufficient for these purposes.

The output time was set to 300 years, and the time step was set to 0.1 year. In these integrations, clones were removed from the simulation upon colliding with the Sun, colliding with a planet, achieving an eccentricity $\geqslant 1$, or leaving the Centaur region. Any clone that did not remain in the Centaur region for at least 100,000 years was not used. The dynamical class of each remaining clone was found using the method of Bailey & Malhotra (2009):

1. Determine the time at which the clone was injected into the Centaur region, T_{Centaur}. Determine the number of data points in the time interval $[0, T_{\text{Centaur}}]$.
2. Create a logarithmic interval of data points using [log (10), log(Data Points)].
3. Divide the interval into 16 equal logarithmic increments. Call the length of one of these increments j_s.
4. Create a window length of 10 data points in units of time. Set this equal to the smallest window length.
5. Create each z_{th} additional window length in units of data points, $w(z)_{\text{datapts}}$, by converting a logarithmic window into a window of data points using $w(z)_{\text{datapts}} = 10^{1+z(j_s)} + 1$ where $z \geqslant 1$.
6. Convert each window length from units of data points into units of time using $w(z)_{\text{time}} = w(z)_{\text{datapts}} \times$ (output time). The interval each window covers is closed on one end and open on the other. For example, the first window time interval would be $[0, w(z)_{\text{time}}]$.
7. Discard any window lengths more than 25% of the data set.
8. Using the smallest window length, partition the time interval $[0, T_{\text{Centaur}}]$ into equal windows of time and allow each window to overlap adjacent windows by half a window length.
9. Within each window, determine the standard deviation, σ, of the semimajor axis, a.
10. Calculate the mean standard deviation, $\bar{\sigma}$, over all windows.
11. Repeat the process for all the window lengths.
12. Perform a linear regression on $\log(\bar{\sigma})$ versus $\log(w(z)_{\text{time}})$.
13. The slope obtained from this regression is an approximation of the Hurst exponent.
14. A residual is the difference between an actual value and its expected value from the best-fit line. In this case, a residual of a particular value of $\log(\bar{\sigma})$ is found by finding the absolute value of the vertical distance from a value of $\log(\bar{\sigma})$ from the best-fit line. A Centaur is classified as being resonance hopping if the maximum value of any one residual is $\geqslant 0.08$. Otherwise, the Centaur is classified as random-walk. This method is based on the results of Bailey & Malhotra (2009), and the reader is referred to that work for more details.

Selected resonance hopping clones were studied in more detail by examining intervals of time in which the semimajor axis oscillated about a nearly constant value.

The semimajor axis values for these intervals of time were then smoothed using the technique of Hinse et al. (2010) to determine if the clone was trapped in a mean motion resonance of a giant planet. The method is as follows:

1. Qualitatively inspect graphs of semimajor axis versus time for resonance hopping Centaurs and identify intervals of time, ΔT_{res}, in which the semimajor axis seems to oscillate about a nearly constant value.
2. Select one of these intervals of time for study. Create a set of all semimajor axis data points during this time interval.
3. Initially, set the smoothed data set equal to the original data set.
4. By inspection, decide on a time window in units of data points. Set the window length to an odd number of data points and call this w_N.
5. Apply the window to the original data set at the first data point.
6. Evaluate the mean value of the semimajor axis over all data points within the window.
7. Set the value of the middle data point in this window (the $j_{(w_N-1)\times 0.5}$ data point) in the smoothed data set to this mean value.
8. Slide the window ahead by one data point in the original data set and set the value of the middle data point in this window in the smoothed data set equal to the mean semimajor axis over the entire window in the original data set.
9. Continue this process until the window ends on the last data point. If j_{last} is the last data point, then in the smoothed data set the $j_{\text{last}} - j_{(w_N-1)\times 0.5}$ data point is set to the mean value of the semimajor axis in the window in the original data set. Any data points before the $j_{(w_N-1)\times 0.5}$ data point and after the $j_{\text{last}} - j_{(w_N-1)\times 0.5}$ data point in the smoothed data set remain unchanged.
10. Try various window lengths until the smoothed data is as close to a cosine or sine wave in time as can be obtained by inspection.
11. Set the nominal location of the mean motion resonance equal to the mean value of the semimajor axis over the time interval ΔT_{res} in the smoothed data set.

12. Compare this location to known locations of mean motion resonances of the giant planets for identification. If the mean value is within 0.1 au of a resonance location, then consider that resonance as a possible candidate.

13. Examine the primary resonance angle associated with each candidate resonance for librating behavior over the time interval. If the angle librates, then consider the clone to be trapped in the resonance over the time of libration.

The locations of mean motion resonances of the giant planets, a_{res}, were found using

$$a_{res} = \left(\frac{j_1}{j_2} \right)^{\frac{2}{3}} a_p \qquad (7)$$

(Murray & Dermott 1999). Here, a_p is the semimajor axis of a planet; and j_1 and j_2 are integers. In this work j_1 and j_2 were limited to values between 1 and 20.

5.3. MEGNO and Lifetime Maps

The chaoticity and chaotic lifetime of Chiron's orbital evolution were studied by means of calculating global MEGNO and lifetime maps over a given parameter region. The MEGNO (Mean Exponential Growth of Nearby Orbits; Cincotta & Simó 2000; Goździewski et al. 2001; Cincotta et al. 2003; Giordano & Cincotta 2004; Hinse et al. 2010) factor is a quantitative measure of the degree of chaos and has found wide-spread applications within problems of dynamical astronomy. The time averaged MEGNO parameter, $\langle Y \rangle$, is related to the maximum Lyapunov Characteristic Exponent, γ, by

$$\langle Y \rangle = t \frac{\gamma}{2} \qquad (8)$$

as $t \to \infty$. For more on Lyapunov characteristic exponents, we direct the interested reader to Whipple (1995).

The detection of chaotic dynamics is always limited to the integration time period. Quasi-periodic or regular motion could in principle develop into chaotic motion over longer timescales. The calculation of $\langle Y \rangle$ involves the numerical solution of the associated variational equations of motion.

Following the definition of MEGNO, the quantity $\langle Y \rangle$ asymptotically approaches 2.0 for $t \to \infty$ if the orbit is quasi-periodic. For chaotic orbits, $\langle Y \rangle$ rapidly diverges far from 2.0. In practice, the limit $t \to \infty$ is not feasible and $\langle Y \rangle$ is only computed up to the integration time (eventually ended by some termination criterion such as the event of an escape or collision).

A MEGNO map is created using the technique of numerical integration of a number of massless test particles starting on initial orbits which cover a rectangular grid in $a - e$ space, with other orbital parameters held constant. In this work, the Gragg–Bulirsh–Stöer (Hairer et al. 1993) method was used to integrate 300,000 test particles for 1 Myr in the region of $a - e$ space bound by 13 au $\leqslant a \leqslant$ 14 au and $0 \leqslant e \leqslant 0.5$. The other orbital parameters were set to those of Chiron.

The resolution of the map was 600×500 $(a - e)$. One test particle was integrated for each $a - e$ pair, for a total of 300,000 $a - e$ pairs.

The time step varied and was determined using a relative and absolute tolerance parameter, both of which were set to be close to the machine precision. A test particle was removed

Table 4
Percentage of First Close Encounters by Clone Small Body Population Membership

Region	% CE
Inner SS	1
SP Comet	2
Centaur	2
TNO	60
Ejection	34

Note. The TNO population has the highest percentage of first close encounters, making it the most likely source population of Chiron.

from the simulation if it collided with a planet or the Sun, was ejected from the solar system, or if $\langle Y \rangle > 12$ (indicating a strong degree of chaos).

When a test particle was removed, the time of removal and the $\langle Y \rangle$ value were recorded. If a test particle survived the entire simulation, then its removal time was recorded as 1 Myr. We will call the removal time the "chaotic lifetime," which is not the same as dynamical lifetime. However, it can be said that the dynamical lifetime is equal to or greater than the chaotic lifetime.

A chaotic lifetime map was then generated in conjunction with the MEGNO map by color-coding the lifetimes in the same $a - e$ grid used to create the MEGNO map. In the lifetime map the shortest removal times were color-coded black and the longest yellow. The resulting lifetime and MEGNO maps can be seen in Figures 7 and 8, respectively.

6. Results

6.1. Half-life and Origin of Chiron

The percentage of first close encounters by clone small body population membership is shown in Table 4. The TNO population has the highest percentage of first close encounters, making it the most likely source population of Chiron.

Thirty-four percent of clones were in a hyperbolic or parabolic orbit during their first close encounter, which indicates a potential origin within the Oort cloud. The Centaur and Inner solar system populations combined contributed just 3% of the first close encounters.

The short period comet population claims 2% of first close encounters. These three populations combined likely illustrate potential final destinations for Chiron in the future, since dynamical evolution that takes no account of the influence of non-gravitational forces is entirely time-reversible.

Figure 1 shows the natural log of the fraction of remaining clones versus time over the last 2.5 Myr. The decay is exponential for the time interval [0.12 Myr, 0.5 Myr]. By 1 Myr ago, the decay curve departs markedly from this initial exponential decay.

This is typical and results from clones that have evolved onto more stable orbits. Because of this, these clones are no longer sampling the original phase space at the start of the decay.

To maximize the fit, the half-life during the exponential decay was determined on the interval [0.12 Myr, 0.367 Myr] and found to be about 0.7 Myr. Other larger intervals were tried and yielded the same result. This value is comparable to, but slightly shorter than, the value of 1.07 Myr reported by Horner et al. (2004b) for this quantity.
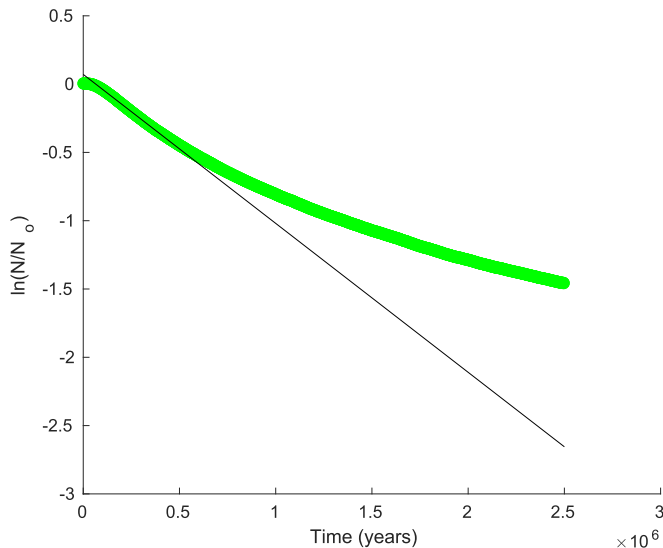
Figure 1. Natural log of the fraction of remaining clones versus time over the last 2.5 Myr. The decay is exponential through the interval [0.12 Myr, 0.50 Myr]. The half-life during the interval [0.12 Myr, 0.367 Myr] was found to be about 0.7 Myr. The solid line is the best-fit line for this interval and fits the data with a linear regression coefficient of 0.9999. By 1 Myr ago, it can be seen that the decay is no longer exponential.

Our smaller value is not surprising because Horner et al. (2004b) found their half-life using the longer time interval of 3 Myr, which included a longer tail over which the half-life was markedly different from its initial value.

A total 786 clones, just 2% of the total population, survived the entire integration time. Ninety-six percent of clones were ejected from the solar system on hyperbolic or parabolic orbits, which again points to an origin for Chiron beyond Neptune. Approximately 1% hit Jupiter, and the remaining 1% hit the Sun, Saturn, Uranus, or Neptune.

Using the best-fit line, we find that if the decay had remained exponential, then 99.99% of the clones would have been gone by 8.5 Myr ago. We use this time as the upper limit to the time at which Chiron first entered the Centaur region.

6.2. Close Encounters

The total number of close encounters between Chiron clones and the giant planets was 24,196,477. A total of 15,130,506 of these occurred while clones were in the Centaur region.

During their time in the Centaur region, clones experienced a close encounter on average every 5 kyr. Table 5 shows the number of these close encounters by planet.

As expected, clones had the highest numbers of close encounters with Saturn and Uranus, followed by Neptune and then Jupiter.

Table 6 lists the percentage of close encounters which occurred in the Centaur region by severity. It can be seen that the lower the severity, the greater the number of close encounters. There were only 48 severe and exactly zero extreme close encounters. These results show that encounters close enough to tidally disrupt Chiron or any ring system around Chiron are extremely rare events.

Thus it is unlikely that any ring structure around Chiron was created by tidal disruption due to a planetary close encounter, and barring ring dispersal by viscous spreading, it is possible that any ring structure around Chiron has survived its journey through the Centaur region and is in fact primordial.

Table 5
Close Encounters of Chiron Clones with Each Giant Planet while Clones Were in the Centaur Region

Planet	Number
Jupiter	553182
Saturn	6978716
Uranus	4567440
Neptune	3031168

Table 6
Percentage of Close Encounters of Chiron Clones with the Giant Planets by Severity while Clones Were in the Centaur Region

Severity	Percent
Very Low	89
Low	11
Moderate	0.03
Severe	0
Extreme	0

Table 7
Percentage of Clones and Mean Centaur Lifetime by Dynamical Class

Class	Percent	Avg. Centaur Life (Myr)
Resonance Hopping	5	1.1
Random-walk	95	0.52

Note. Random-walk dominates in quantity, but resonance hopping clones have about twice the mean centaur lifetime as random-walk clones due to resonance sticking.

6.3. Dynamical Class of Chiron

The dynamical classes of 1246 clones were determined. Table 7 shows the percentage of clones in each dynamical class, and the mean Centaur lifetime of clones in each class. Ninety-five percent of the sampled clones were classified as random-walk Centaurs, with the remaining 5% being classified as resonance hopping Centaurs.

The difference in mean Centaur lifetime between the two classes is stark. The mean Centaur lifetime for the resonance hopping clones was approximately twice as long as that of random-walk clones.

We hypothesise that the large difference is caused by resonance sticking in mean motion resonances of resonance hopping clones having the effect of prolonging their dynamical lifetimes. This is supported by the work of Bailey & Malhotra (2009). The top of Figure 2 shows the behavior of the semimajor axis of the orbit of one of the longest lived resonance hopping clones. In the figure, the semimajor axis spends about 5 Myr oscillating about the 2:3 mean motion resonance of Saturn centered at 12.5 au. Notice the horizontal band feature which covers this period of time. A shorter band centered at 15.1 au is caused by the exterior 1:2 mean motion resonance of Saturn.

Examination of other resonance hopping clones also showed relatively long periods of time for which each clone was trapped in one or more mean motion resonances. We conclude that resonance sticking acts to significantly prolong the lives of resonance hopping clones. Other notable resonances entered into by clones include the exterior 3:4, 4:7, and 1:3 resonances of Saturn; the Trojan or 1:1 resonance of Saturn; the interior 3:2
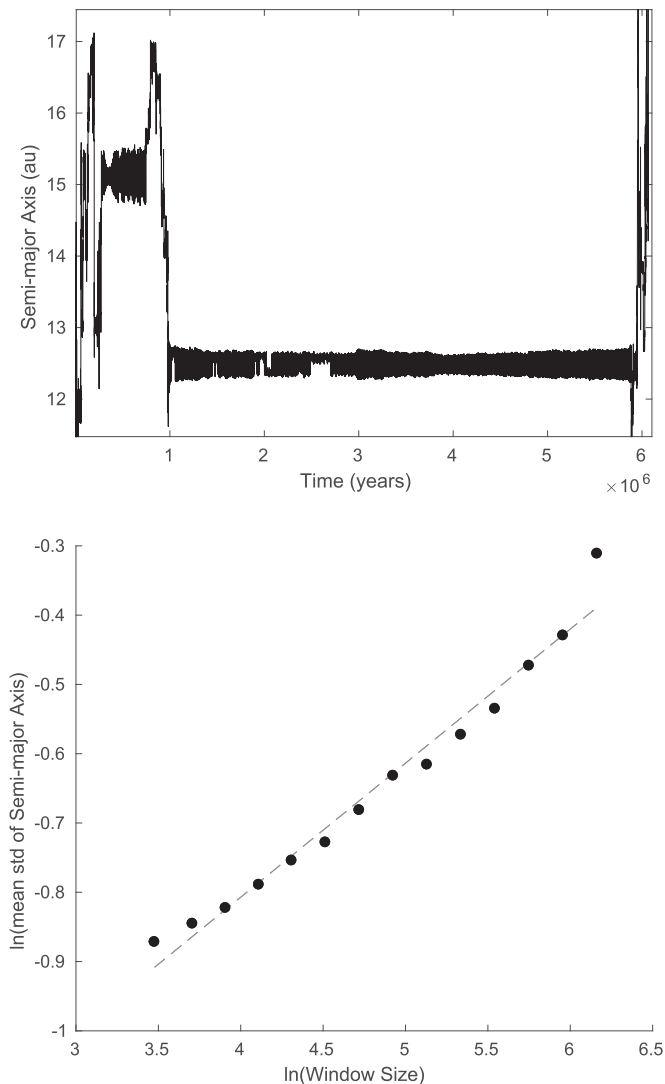
Figure 2. Top—an example of a resonance hopping clone. Note the long horizontal band feature. This clone spends about 5 Myr oscillating about the 2:3 mean motion resonance of Saturn located at 12.5 au. A shorter band centered at 15.1 au is caused by the exterior 1:2 mean motion resonance of Saturn. Bottom—the log–log plot used to identify the dynamical class of the clone in the top diagram. Notice the one data point at a larger distance from the trendline than the others. This is characteristic behavior for resonance hopping Centaurs. The Hurst exponent for this clone was 0.193, and its linear regression coefficient was 0.971. The maximum residual was 0.08.

resonance of Uranus; and the interior 3:2 and 4:3 resonances of Neptune.

The bottom diagram in Figure 2 shows the log–log plot used to classify the clone. It can be seen that it only takes one data point with a relatively large residual to cause a clone to be classified as resonance hopping.

The top diagram in Figure 3 shows another example of a resonance hopping clone. In contrast to the clone in Figure 2, which spends most of its time in one resonance, this clone spends most of its time hopping between mean motion resonances of the giant planets. Two of these resonances were positively identified as the 4:3 and 3:2 mean motion resonances of Neptune by observing the libration of their primary resonance angles.

The bottom diagram shows a close-up of the time spent in the 4:3 mean motion resonance of Neptune before and after

data smoothing. The smoothed data set has a mean semimajor axis value that is only 0.07 au away from the 4:3 mean motion resonance of Neptune, located at 24.89 au.

Figure 4 shows the primary resonance angle associated with the 4:3 mean motion resonance of Neptune for the clone in Figure 3 over the same time interval. The angle is defined by $4\lambda_N - 3\lambda - \bar{\omega}$, where λ_N is the mean longitude of Neptune. It can be seen that this angle librates.

Figure 5 shows an example of a random-walk clone. This clone does not spend the majority of its life trapped in mean motion resonances, as can be seen by the lack of long horizontal bands in the figure.

The mean Hurst exponent of the random-walk clones is 0.4664 ± 0.0782, and that of the resonance hopping clones is 0.3572 ± 0.1530. Here the error is given by the standard deviation of the mean. It can be seen that Hurst exponents of random-walk clones are more well defined than those of resonance hopping clones, as the standard deviation of the mean of the Hurst exponents of random-walk clones is about half that of the resonance hopping clones.

Hurst exponents ranged from -0.1764 to 0.6416 for resonance hopping clones and from 0.1446 to 0.7462 for random-walk clones. The lowest regression coefficient for a random-walk clone was 0.85, and resonance hopping clones had regression coefficients ranging from -0.33 to 0.99.

Bailey & Malhotra (2009) reported that random-walk Centaurs display Hurst exponents in the range 0.22–0.95. We found that only five of our random-walk clones had Hurst exponents outside this range—all of them <0.22.

Qualitative inspection showed that four of these five could be classified as resonance hopping Centaurs, as they spent the majority of their lives in mean motion resonances. The fifth clone displayed both random-walk and resonance hopping behavior, but spent most of its time experiencing random-walk evolution. The fit of that clone's log–log plot had a regression coefficient of only 0.85, which is more than three standard deviations away from the mean value of 0.9947 ± 0.0089 for random-walk clones.

Furthermore, the outliers also had another thing in common: of the total time spent in resonances, each spent the majority of that time in only one strong resonance and did not jump into any other strong resonances. An example of one of these five outliers is shown in Figure 6.

This particular clone spends 66% of its life in the 2:3 mean motion resonance of Saturn and never jumps to another strong resonance. It was classified as a random-walk clone because its residuals never exceeded 0.0601, but since it spent more time in a resonance than random walking, one could argue that this clone is resonance hopping even though our method classifies it as random-walk. The linear regression coefficient of its log–log plot was 0.88, and its Hurst exponent was 0.19.

We conclude that our results are in good agreement with those of Bailey & Malhotra (2009), but that our technique occasionally misclassifies a clone. A refinement of this technique may be to consider the regression coefficients as well as the residuals as part of the classification procedure.

For example, if the regression coefficient of a random-walk clone falls below some critical value, then the clone should be classified manually. That is, classify it using qualitative inspection of the clone's semimajor axis behavior over time. The exact critical value to use will be left open for now.
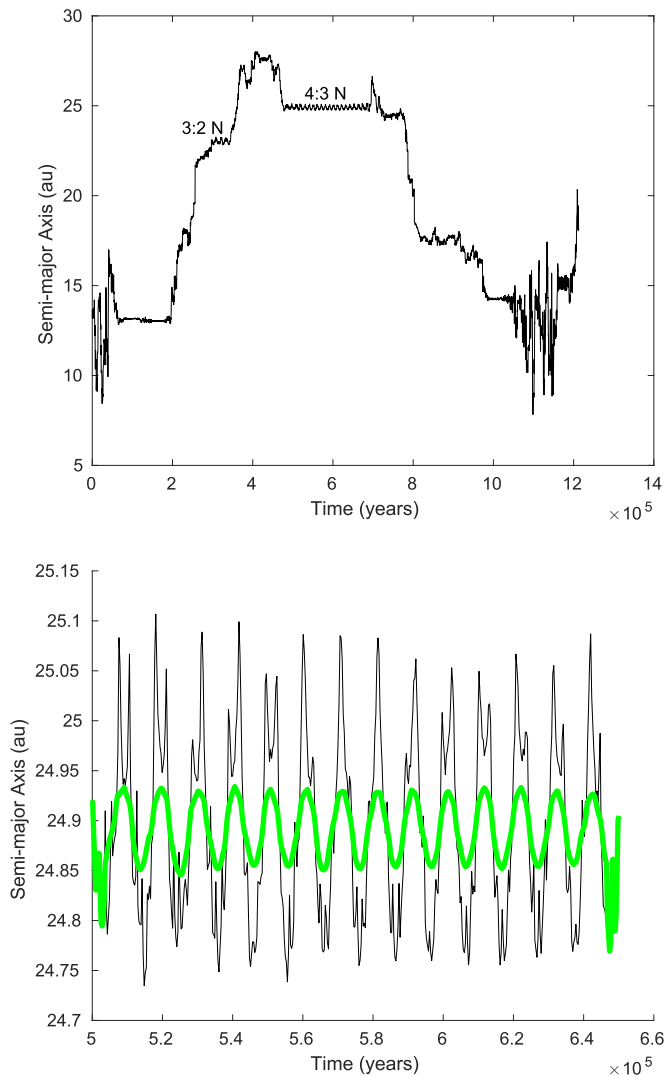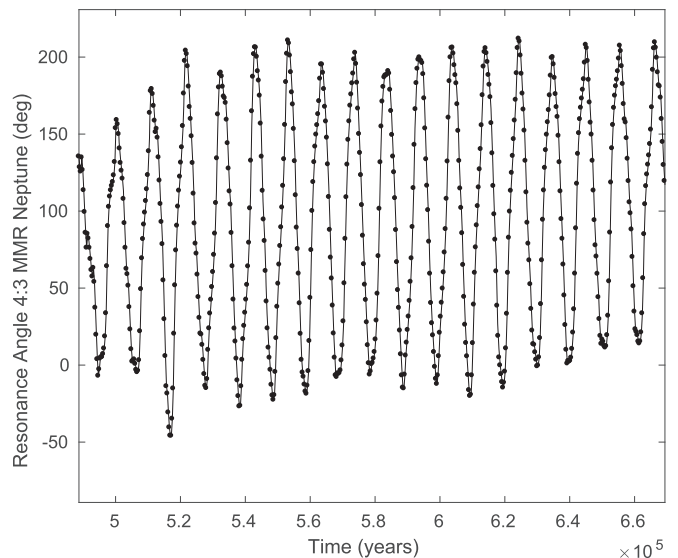
Figure 4. The primary resonance angle of the 4:3 mean motion resonance of Neptune defined by $4\lambda_N - 3\lambda - \bar{\omega}$ librates in time.

Figure 3. Top—another example of a resonance hopping clone. This clone spends most of its time trapped in various mean motion resonances of the giant planets. Two resonances were positively identified as the 4:3 and 3:2 mean motion resonances of Neptune. These are labeled in the figure. The Hurst exponent was 0.534, the linear regression coefficient was 0.9937, and the maximum residual was 0.08. Bottom—a close-up of the time spent in the 4:3 mean motion resonance of Neptune before and after data smoothing. The mean value of the smoothed data set was 24.89 au, which is about 0.07 au away from the 4:3 mean motion resonance of Neptune.

Another factor to consider is the distance of the Hurst exponent from the mean. All five of the outlying random-walk clones had Hurst exponents more than three standard deviations away from the mean. A refinement of the technique may be to manually classify any clones with outlying Hurst exponents. It remains to be seen if all outliers spend most of their lives in just one strong resonance or if this is just coincidental.

6.4. MEGNO and Lifetime Maps

Figure 7 shows the chaotic lifetimes of orbits in the region bound by 13 au $\leqslant a \leqslant$ 14 au and 0 $\leqslant e \leqslant$ 0.5. It can be seen that most orbits with $e \geqslant 0.23$ have lifetimes typically $\leqslant$0.01 Myr, which are noticeably shorter than the lifetimes of orbits of much lower eccentricity.

Chiron, located at the point (13.64 au, 0.38) lies in this region of relatively short lifetimes. Orbits with $a = 13$ au and

eccentricity of 0.23 just begin to cross the orbit of Saturn. All orbits with eccentricities above about 0.28 are Saturn crossing. This allows strong close encounters between objects on those orbits and the giant planet to occur immediately, which explains why most orbits with $e \geqslant 0.28$ have lifetimes $\leqslant$0.01 Myr—the lowest in the map.

One exception to this is the bump-like feature centered at 13.4 au, with a width of about 0.2 au. Orbits within the bump with eccentricities as high as 0.35 have lifetimes noticeably greater than 0.01 Myr.

For example, there are orbits in the bump with $e \geqslant 0.28$ with lifetimes of 0.1 Myr, which is an order of magnitude longer than most other orbits in the map with $e \geqslant 0.28$. Also of note is a cluster of orbits within the bump near $e = 0.1$, for which lifetimes can reach as high as 1 Myr—the longest in the map. We hypothesise that the bump feature is caused by resonance sticking in the 3:5 mean motion resonance of Saturn located at 13.4 au.

Small objects that get stuck in this resonance could have their chaotic lifetimes extended in the same way that the Centaur lifetime was extended for a clone stuck in the 2:3 mean motion resonance of Saturn, as seen in Figure 2. It should be noted, however, that most orbits located at 13.4 au with eccentricities below 0.06 have lifetimes noticeably shorter than 1 Myr.

This implies that small objects in this region of phase space are either not being captured in the resonance or are staying in the resonance for shorter times, which results in lower lifetimes. This may be caused by the decreasing width of the resonance for smaller eccentricities.

Such behavior of resonances has been seen before. For example, Murray & Dermott (1999) observed the same behavior for the 3:1 and 5:3 interior mean motion resonances of Jupiter located in the main asteroid belt.

Another bump of longer lifetimes that reach as high as 1 Myr is found between 13.9 and 14 au with $e \leqslant 0.05$. The low eccentricity of orbits in this bump help insulate them from destabilizing close encounters with Saturn and Uranus. Though their lifetimes of 1 Myr are relatively long compared to other orbits in the figure, this is still much shorter than the age of the
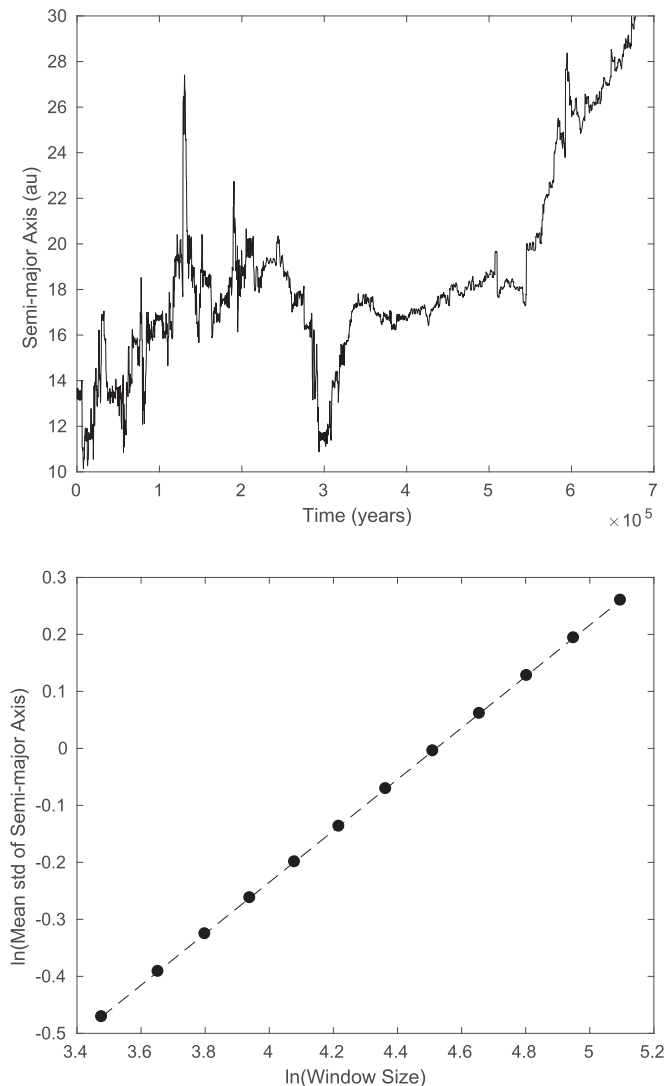
Figure 6. Random-walk clone that spent most of its life in the 2:3 mean motion resonance of Saturn located at 12.5 au. Though its residuals were ⩽0.0601, one could argue that it is a resonance hopping clone.

Figure 5. Top—an example of a random-walk clone. Notice how the long horizontal bands are absent. Bottom—the log–log plot used to identify the dynamical class of the clone in the top diagram. Notice the good fit. The linear regression coefficient was 0.9998, and the Hurst exponent for this clone was 0.4514. The maximum residual was 0.008.

solar system and so these orbits should be viewed as being only relatively stable.

Figure 8 is the MEGNO map of the same region of phase space. Almost the entire region, including the current orbit of Chiron, is highly chaotic. Two features of relatively lower chaos stand out: one island centered around 13.4 au with $0.1 \leqslant e \leqslant 0.15$ and a pair of islands between 13.9 and 14 au with $e < 0.04$. Here the MEGNO parameter reaches as low as 2.5. Two tinier islands can be seen between 13.7 and 13.9 au.

By comparison of the two maps, it can be seen that these islands are also embedded within regions of relatively long lifetimes that can reach as high as 1 Myr, making these islands regions of lower chaos and longer lifetimes.

It can also be seen that the two bumps of relatively long lifetimes found in the lifetime map also contain some orbits with lifetimes of 1 Myr that are also highly chaotic. Orbits that are chaotic but have a relatively long lifetime are said to display stable chaos.

Chiron, however, cannot be shown to display stable chaos, as it has a highly chaotic orbit and relatively short lifetime.
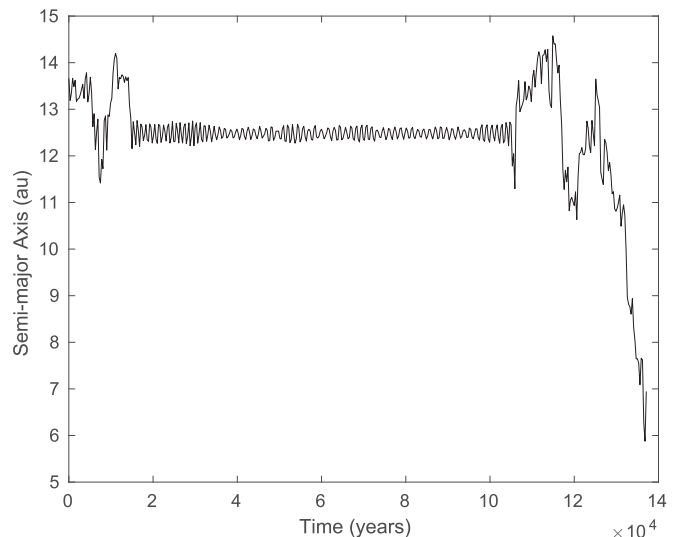
7. Conclusions

Using the technique of numerical integration of nearly 36,000 clones of the Centaur Chiron, we found the backward half-life of Chiron's orbit to be 0.7 Myr and showed that Chiron likely entered the Centaur region from somewhere beyond Neptune within the last 8.5 Myr.

Close encounters between Chiron and the giant planets severe enough to tidally disrupt Chiron or any ring system in a single pass were found to be extremely rare, and thus the origin of any ring structure is unlikely the result of tidal disruption of Chiron due to a planetary close encounter.

This led us to conclude that any supposed ring system around Chiron could be primordial barring ring dispersal by viscous spreading. Our results are similar to those of Wood et al. (2017) and Araujo et al. (2016) for the ringed Centaur Chariklo. In those studies, close encounters severe enough to severely damage or destroy the ring structure around Chariklo were also found to be very rare.

We also showed that the orbit of Chiron lies in a region of phase space that is both unstable and highly chaotic, and that the chaotic lifetime of Chiron is likely to be ⩽0.01 Myr. Resonance sticking was shown to have the ability to prolong the Centaur lifetime of Chiron clones by up to two orders of magnitude beyond its chaotic lifetime. Resonance sticking in the 2:3 exterior mean motion resonance of Saturn was cited as a strong example of this.

The dynamical classes of a sample of 1246 clones were determined while these clones were in the Centaur region. It was found that 95% of clones in the sample were categorized as random-walk Centaurs, and the remaining 5% were categorized as resonance hopping Centaurs. Because of resonance sticking, the mean Centaur lifetime of resonance hopping clones was about twice that of random-walk clones.

MEGNO and lifetime maps were made of the region in phase space bound by 13au ⩽ a ⩽ 14au and e ⩽ 0.5, which included the orbit of Chiron. It was found that nearly the entire region is highly chaotic, with relatively small islands of lower chaos. Other small islands of stable chaos (high chaos and relatively long lifetime) were found.
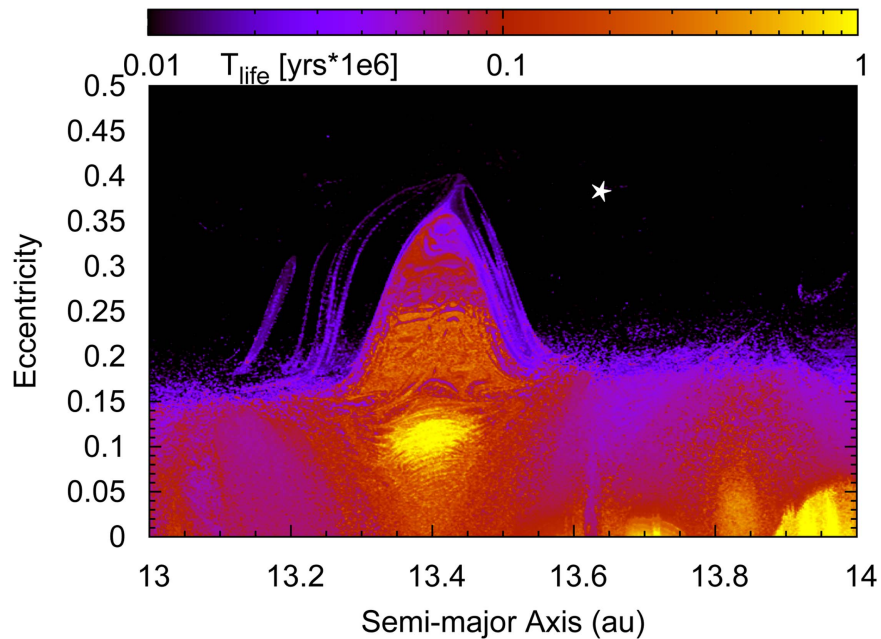
Figure 7. Chaotic lifetime map in $a - e$ space. Chaotic lifetime is the time to be removed from the simulation and not dynamical lifetime. However, the dynamical lifetime is greater than or equal to the chaotic lifetime. Chiron is shown as the star at the point (13.64 au, 0.38). A feature that stands out is the bump centered at 13.4 au, which has a width of about 0.2 au and a height of about 0.35. We hypothesize that the cause of the bump is resonance sticking in the 3:5 mean motion resonance of Saturn, which prolongs the lifetimes of test particles that get trapped in the resonance. A smaller bump can be seen between 13.9 and 14 au with $e \leqslant 0.05$. There is also a tiny bump in lifetimes up to 1 Myr between 13.7 and 13.75 au.
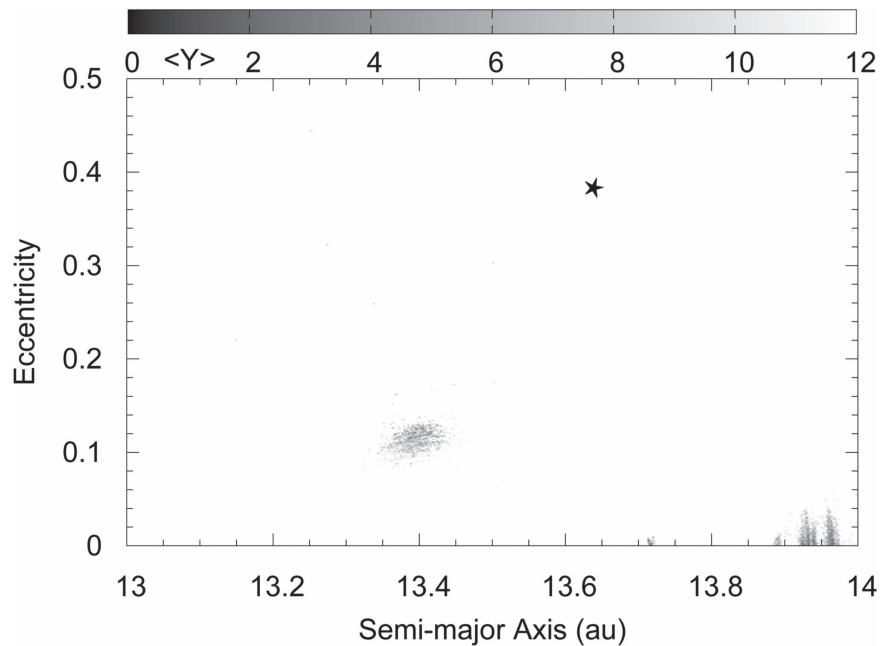
Figure 8. MEGNO map in $a - e$ space. Chiron is shown as the star at the point (13.64 au, 0.38). Nearly the entire region is highly chaotic. There are a few small islands of orbits with relatively low chaos. One is centered near 13.4 au with $0.1 \leqslant e \leqslant 0.15$, where the MEGNO parameter can reach as low as 3.5. Two others can be seen between 13.9 and 14 au, in which the MEGNO parameter reaches as low as 2.5. Two tinier islands can be seen between 13.7 and 13.9 au.

Most orbits with eccentricities $\geqslant 0.28$ had the lowest chaotic lifetimes in the map of $\leqslant 0.01$ Myr due to the crossing of Saturn's orbit. However, some test particles in orbits with $e \geqslant 0.28$ and semimajor axes within about 0.1 au of the exterior 3:5 mean motion resonance of Saturn located at 13.4 au were shown to have lifetimes up to 0.1 Myr, even for orbits with eccentricities up to about 0.35.

More research is needed to determine conclusively if the structure around Chiron is a ring system. It is not known

if rings around small bodies are rare or commonplace. If future discoveries reveal that ringed Centaurs are common, it would suggest a common mechanism for the creation of the rings.

If, on the other hand, ringed Centaurs are found to be rare, then this would suggest a more serendipitous origin for rings. The authors encourage more searches for rings around other small bodies to help answer this question.

ORCID iDs

Jeremy Wood ● https://orcid.org/0000-0003-1584-302X
Jonti Horner ● https://orcid.org/0000-0002-1160-7970
Tobias C. Hinse ● https://orcid.org/0000-0001-8870-3146

References

Araujo, R. A. N., Sfair, R., & Winter, O. C. 2016, ApJ, 824, 80
Bailey, B. L., & Malhotra, R. 2009, Icar, 203, 155
Braga-Ribas, F., Sicardy, B., Ortiz, J. L., et al. 2014, Natur, 508, 72
Brasser, R., Schwamb, M. E., Lykawka, P. S., & Gomes, R. S. 2012, MNRAS, 420, 3396
Bus, S. J., Buie, M. W., Schleicher, D. G., et al. 1996, Icar, 123, 478
Chambers, J. E. 1999, MNRAS, 304, 793
Chiang, E., Lithwick, Y., Murray-Clay, R., et al. 2007, in Protostars and Planets V, ed. B. Reipurth, D. Jewitt, & K. Keil (Tucson, AZ: Univ. Arizona Press), 895
Cincotta, P. M., Giordano, C. M., & Simó, C. 2003, PhyD, 182, 151
Cincotta, P. M., & Simó, C. 2000, A&AS, 147, 205
de la Fuente Marcos, C., & de la Fuente Marcos, R. 2014, Ap&SS, 352, 409
Di Sisto, R. P., & Brunini, A. 2007, Icar, 190, 224
Dones, L., Levison, H. F., & Duncan, M. 1996, in ASP Conf. Ser. 107, Completing the Inventory of the Solar System, ed. T. W. Rettig & J. M. Hahn (San Francisco, CA: ASP), 233
Duffard, R., Lazzaro, D., Pinto, S., et al. 2002, Icar, 160, 44
Elliot, J. L., Kern, S. D., Clancy, K. B., et al. 2005, AJ, 129, 1117
Elliot, J. L., Olkin, C. B., Dunham, E. W., et al. 1995, Natur, 373, 46
El Moutamid, M., Kral, Q., Sicardy, B., et al. 2014, in AAS Meeting 45 Abstracts, 402.05
Emel'yanenko, V. V., Asher, D. J., & Bailey, M. E. 2005, MNRAS, 361, 1345
Fornasier, S., Lellouch, E., Müller, T., et al. 2013, A&A, 555, A15
Fouchard, M., Rickman, H., Froeschlé, C., & Valsecchi, G. B. 2014, Icar, 231, 99
French, R. G., McGhee, C. A., Dones, L., & Lissauer, J. J. 2003, Icar, 162, 143
Giordano, C. M., & Cincotta, P. M. 2004, A&A, 423, 745
Gladman, B., Marsden, B. G., & Vanlaerhoven, C. 2008, in The Solar System Beyond Neptune, ed. M. A. Barucci et al. (Tucson, AZ: Univ. Arizona Press), 43
Goździewski, K., Bois, E., Maciejewski, A. J., & Kiseleva-Eggleton, L. 2001, A&A, 378, 569
Groussin, O., Lamy, P., & Jorda, L. 2004, A&A, 413, 1163
Hahn, G., & Bailey, M. E. 1990, Natur, 348, 132
Hairer, E., Nørsett, S. P., & Wanner, G. 1993, Solving Ordinary Differential Equations I, Vol. 8 (Berlin: Springer)
Hinse, T. C., Christou, A. A., Alvarellos, J. L. A., & Goździewski, K. 2010, MNRAS, 404, 837
Horner, J., Evans, N. W., & Bailey, M. E. 2004a, MNRAS, 354, 798
Horner, J., Evans, N. W., & Bailey, M. E. 2004b, MNRAS, 355, 321
Horner, J., Evans, N. W., Bailey, M. E., & Asher, D. J. 2003, MNRAS, 343, 1057

Horner, J., & Lykawka, P. S. 2010, MNRAS, 402, 13
Horner, J., Lykawka, P. S., Bannister, M. T., & Francis, P. 2012a, MNRAS, 422, 2145
Horner, J., Marshall, J. P., Wittenmyer, R. A., & Tinney, C. G. 2011, MNRAS, 416, L11
Horner, J., Müller, T. G., & Lykawka, P. S. 2012b, MNRAS, 423, 2587
Horner, J., & Wyn Evans, N. 2006, MNRAS, 367, L20
Hyodo, R., Charnoz, S., Genda, H., & Ohtsuki, K. 2016, ApJL, 828, L8
Jacobson, R. A., & French, R. G. 2004, Icar, 172, 382
Jewitt, D. 2009, AJ, 137, 4296
Jewitt, D. C. 2004, in Comets II, ed. M. C. Festou, H. U. Keller, & H. A. Weaver (Tucson, AZ: Univ. Arizona Press), 659
Knezevic, Z., & Milani, A. 2012, IAU Joint Discussion, 7, P18
Kovalenko, N. S., Babenko, Y. G., & Churyumov, K. I. 2002, EM&P, 90, 489
Kovalenko, N. S., Churyumov, K. I., & Babenko, Y. G. 2011, AstSR, 7, 230
Kowal, C. T., Liller, W., & Marsden, B. G. 1979, in Dynamics of the Solar System, Vol. 81 (Dordrecht: Reidel), 245
Lazzaro, D., Florczak, M. A., Betzler, A., et al. 1996, P&SS, 44, 1547
Levison, H. F., & Duncan, M. J. 1997, Icar, 127, 13
Liller, W., Chaisson, L. J., & Marsden, B. G. 1977, IAUC, 3151, 2
Lykawka, P. S., & Horner, J. 2010, MNRAS, 405, 1375
Lykawka, P. S., & Mukai, T. 2007, Icar, 192, 238
Malhotra, R. 1995, AJ, 110, 420
Marsden, B. G. 1962, ASPL, 8, 375
Meech, K. J., Buie, M. W., Samarasinha, N. H., Mueller, B. E. A., & Belton, M. J. S. 1997, AJ, 113, 844
Melita, M. D., Duffard, R., Ortiz, J. L., & Campo-Bagatin, A. 2017, A&A, 602, A27
Michikoshi, S., & Kokubo, E. 2017, ApJL, 837, L13
Murray, C. D., & Dermott, S. F. 1999, Solar System Dynamics (Cambridge: Cambridge Univ. Press)
Noll, K. 1994, PlR, 14, 8
Oikawa, S., & Everhart, E. 1979, AJ, 84, 134
Ortiz, J. L., Duffard, R., Pinilla-Alonso, N., et al. 2015, A&A, 576, A18
Ortiz, J. L., Santos-Sanz, P., Sicardy, B., et al. 2017, Natur, 550, 219
Pál, A., Kiss, C., Horner, J., et al. 2015, A&A, 583, A93
Pan, M., & Wu, Y. 2016, ApJ, 821, 18
Philpott, C. M., Hamilton, D. P., & Agnor, C. B. 2010, Icar, 208, 824
Rein, H., & Liu, S.-F. 2012, A&A, 537, A128
Rein, H., & Spiegel, D. S. 2015, MNRAS, 446, 1424
Robertson, P., Horner, J., Wittenmyer, R. A., et al. 2012, ApJ, 754, 50
Roche, E. 1849, Academie des Sciences de Montpellier: Memoires de la Sectiondes Sciences, 1, 243
Roig, F., Nesvorný, D., & Ferraz-Mello, S. 2002, MNRAS, 335, 417
Ruprecht, J. D., Bosh, A. S., Person, M. J., et al. 2015, Icar, 252, 271
Scholl, H. 1979, Icar, 40, 345
Shi, J. C., & Ma, Y. H. 2015, MNRAS, 454, 3635
Silva, A. M., & Cellone, S. A. 2001, P&SS, 49, 1325
Smirnov, E. A., & Shevchenko, I. I. 2013, Icar, 222, 220
Sykes, M. V., & Walker, R. G. 1991, Sci, 251, 777
Tiscareno, M. S., & Malhotra, R. 2003, AJ, 126, 3122
Tsiganis, K., Varvoglis, H., & Hadjidemetriou, J. D. 2000, Icar, 146, 240
Volk, K., & Malhotra, R. 2008, ApJ, 687, 714
Whipple, A. L. 1995, Icar, 115, 347
Wierzchos, K., Womack, M., & Sarid, G. 2017, AJ, 153, 230
Williams, J. G., & Benson, G. S. 1971, AJ, 76, 167
Wittenmyer, R. A., Horner, J., & Tinney, C. G. 2012, ApJ, 761, 165
Wood, J., Horner, J., Hinse, T. C., & Marsden, S. C. 2017, AJ, 153, 245
Wood, J. R., Horner, J., Hinse, T., Marsden, S. & Swinburne University of Technology 2016, in AAS/DPS Meeting 48 Abstracts, 120.23

4 Measuring the Severity of Close Encounters Between Ringed Small Bodies and Planets

The greatest gravitational perturbations of rings about a small body occur during close encounters between the ringed body and the giant planets. A study of the close encounter history of a ringed small body can help determine the likelihood that ring destroying close encounters have occurred. This in turn has consequences for ring origin theories and ring longevity.

In the two previous chapters, our results of integrations of clones of Chariklo and Chiron showed the likelihood that the rings around either body predated that body's entrance into the Centaur region. Numerical integrations of small bodies without rings are useful for direct study of small body dynamics and indirect study of the rings.

Integrations with rings around a large number of clones is too time prohibitive. This is why we developed a close encounter severity scale based only on the minimum separation distance obtained during the encounter. Using this scale we were able to successfully examine close encounters between ringed small bodies and giant planets without actually integrating the ring particles themselves.

However, our scale is dependent upon the accuracy with which the critical distances of the Hill radius, tidal disruption distance, Roche Limit and ring limit are known. The first four of these are well known and have approximate analytical solutions. The ring limit is a relatively new parameter which currently has no simple analytical expression.

Our first version of a close encounter severity scale included a ring limit set to a constant value of 10 tidal disruption distances. This value was based on previous work by other researchers and was constant for each planet. This was only a rough approximation as it ignored velocity effects and only partially accounted for the effects of the planet mass, small body mass and ring orbital radius.

In reality, the ring limit should a function of these quantities. Using numerical integration to simulate close encounters between giant planets and one-ringed small bodies over a range of orbital radii and small body masses for each planet would allow the functional dependence of the ring limit on these quantities to be found.

In order to improve our scale, close encounters between ringed small bodies and planets were simulated with the ring particles themselves included in the integrations. This allowed the functional dependence of the ring limit on each quantity to be found.

The integrations were carried out, and the results analysed. Using regression, it was found that the ring limit increased with ring orbital radius and planet mass as a power law ($R \sim r^{\alpha}$ and $R \sim M_p^{\gamma}$) and decreased with small body mass as a power law ($R \sim m_s^{\beta}$). The exponents α, β and γ were themselves a function of the velocity at infinity and other variables. No particular relationship between the ring limit and velocity at infinity could be found. The ring limit

was found to have a constant lower bound of approximately 1.8 tidal disruption distances with a small dependence on the mass of the planet. This means that all close encounters occurring within a distance of 1.8 tidal disruption distances are noticeable.

The ring limit equaled this lower bound only when the small body was in a parabolic orbit about the planet. Using this, an approximate analytical solution of the ring limit for parabolic orbits was obtained. Analytical solutions for hyperbolic orbits could only be found for specific cases.

The ring limit was found to form a curve in $d_{min} - v_\infty$ space. By extrapolating our data, a ring limit upper bound curve was found for close encounters between Chariklo and each planet.

We found that 26 out of 27 d_{min} values were within their respective ring limit upperbound curve as expected. At this time, we cannot explain the one discrepancy.

A paper entitled "Measuring the Severity of Close Encounters Between Ringed Small Bodies and Planets" has been submitted for publication in the Monthly Notices of the Royal Astronomical Society and is currently under review. This paper follows.

MEASURING THE SEVERITY OF CLOSE ENCOUNTERS BETWEEN RINGED SMALL
BODIES AND PLANETS

JEREMY WOOD,[1,2] JONTI HORNER,[3,4] TOBIAS C. HINSE,[5] AND STEPHEN C. MARSDEN[2]

[1] *Hazard Community and Technical College, Community College Drive Hazard, KY USA 41701*
[2] *Computational Engineering and Science Research Centre, University of Southern Queensland West St, Toowoomba, QLD 4350, Australia*
[3] *University of Southern Queensland, Computational Engineering and Science Research Centre West St, Toowoomba, QLD 4350, Australia*
[4] *Australian Centre for Astrobiology, UNSW Australia, Sydney, NSW 2052, Australia*
[5] *Korea Astronomy and Space Science Institute, 776 Daedukdae-ro, Yuseong-gu, Daejeon 305-348, Republic of Korea*

ABSTRACT

In our previous works, we studied close encounters of Chariklo and Chiron with the giant planets using numerical integration. In those works, we recognized the importance of establishing a criterion by which the effect of close encounters between ringed small bodies and planets on the stability of the rings could be measured. The severity of each encounter was found by comparing the minimum separation distance of the encounter, d_{min}, to known critical distances.

Two of these distances are the tidal disruption distance, R_{td}, and ring limit, R, which separates noticeable encounters from non-noticeable encounters. In previous work, $R = 10R_{td}$. In this work, we seek to improve our expression for R by fully accounting for the effects of the planet mass, as well as the velocity at infinity, v_∞, mass and ring orbital radius, r, associated with the small body.

To accomplish this, we use numerical integration to simulate close encounters between each giant planet and hypothetical one-ringed bodies in the three-body planar problem and find R for each encounter. Using regression, we find the functional dependence of R on planet mass, small body mass, v_∞, and r as well as discover that R has a nearly constant lower bound of approximately $1.8R_{td}$. We use these dependencies to extrapolate our R values to find a ring limit upper bound curve in $d_{min} - v_\infty$ space for close encounters between Chariklo and each giant planet.

We suggest three different methods for using this curve to find R and use all three to compare our extrapolated results to previously published d_{min} values associated with planet-Chariklo encounters in the seven-body non-planar problem. We find good agreement and that the new R values are more accurate than before.

Keywords: planets and satellites: dynamical evolution and stability, planets and satellites: rings

1. INTRODUCTION

The Centaurs are a population of icy bodies moving on dynamically unstable orbits in the outer Solar system (e.g. Tiscareno & Malhotra 2003; Horner et al. 2004a,b; Di Sisto & Brunini 2007; Bailey & Malhotra 2009). The first Centaur discovered, 2060 Chiron, was found in 1977 (Kowai et al. 1979), and it was soon found to be unusual. The second Centaur, 5145 Pholus, was found in 1992, and many more soon followed.

The exact definition of a Centaur varies within the research community. This work defines Centaurs as objects with semi-major axes between the orbits of Jupiter and Neptune, and perihelia beyond Jupiter (e.g. Sheppard et al. 2000). Using this definition, more than 220 of these objects have been discovered[1].

It is the general consensus that Centaurs were perturbed into their present orbits via gravitational interactions with the giant planets. The original source of the Centaurs is likely other more stable small body populations such as the Kuiper Belt objects (e.g. Levison & Duncan 1997; Horner et al. 2004b), Scattered Disk Objects (e.g. Di Sisto & Brunini 2007; Volk, & Malhotra 2008) Oort Cloud objects (e.g. Emel'yanenko et al. 2005; Brasser et al. 2012; Fouchard et al. 2014), Trojan asteroids of Jupiter (e.g. Horner & Evans 2006; Horner et al. 2012b), and Trojan asteroids of Neptune (Horner & Lykawka 2010a,b; Horner et al. 2012a).

On timescales comparable to the age of the Solar system (4.6 Gyr), Centaurs are indeed an ephemeral class of object with dynamical lifetimes on the order of 10 Myr (Tiscareno & Malhotra 2003). Objects in the Centaur population typically experience frequent close encounters with the four giant planets. These encounters can drive rapid evolution of Centaur orbits on timescales of just hundreds or thousands of years (Wood et al. 2017). This results in the orbits of Centaurs being chaotically perturbed, redistributing the objects throughout the Solar system, and in many cases, transferring them to other Solar system small body populations, such as the Jupiter family comets (e.g. Tiscareno & Malhotra 2003).

Other fates of Centaurs include planetary collision, collision with the Sun, injection into the Oort Cloud or ejection from the Solar system. Centaurs may even temporarily enter the Scattered Disk (e.g. Tiscareno & Malhotra 2003; Horner et al. 2004a,b; Bailey & Malhotra 2009).

Given the dynamically chaotic nature of the Centaur region, it came as a complete surprise when two narrow rings were discovered around the largest Centaur Chariklo by means of a stellar occultation event in 2013 (Braga-Ribas et al. 2014).

Analysis of occultation data concluded that the rings have radii of 391 km and 405 km with widths of about 7 km and 3 km respectively (Braga-Ribas et al. 2014). It has been suggested that rings may also exist or have existed around the Centaur Chiron (e.g. Ortiz et al. 2015; Pan & Wu 2016); satellites of Saturn and Uranus; and even the dwarf planet Pluto (Rawal & Nikouravan 2011; Sicardy et al. 2016). Though none of these have been confirmed, the Trans-Neptunian object Haumea is the only small body besides Chariklo known to have rings (Ortiz et al. 2017).

When considering the origin of the rings of the Centaurs, and whether or not they truly predate the injection of the objects to the Centaur population, it is relevant to note that the rings of Haumea are particularly interesting since Haumea is the largest object in the trans-Neptunian region's only known collisional family (e.g. Brown et al. 2007; Lykawka et al. 2012) - in other words, Haumea and its associated family are the debris left behind from a collision that could readily have injected material to orbits that would one day evolve to enter the Centaur population.

Indeed, by integrating over 35,000 clones backwards in time, Wood et al. (2017) and Wood et al. (2018) confirm that any rings around Chariklo or Chiron could predate their entrance into the Centaur region. Once there, given the frequency with which the Centaurs experience close encounters with the giant planets, it is natural to wonder what effect such encounters would have on the rings around those objects.

This has been investigated for the case of Chariklo by Araujo et al. (2016) in the seven-body (Sun, Chariklo, four giant planets, ring particle) non-planar problem who stated that the effect of a close encounter on a ring was qualitatively "noticeable" if the maximum change in eccentricity, Δe_{max}, of the orbit of any ring particle was ≥ 0.01. In that study, ring particles were initially randomly distributed in the same circular orbit before the encounter. After the encounter, the minimum approach distance of the small body to the planet (the close encounter distance) and the largest change in eccentricity of the orbit of a ring particle were recorded.

In this manner, they were able to investigate the likelihood that Chariklo's rings could survive through the duration of its life in the Centaur region. By studying the evolution of rings around 729 clones of Chariklo,

---

they found that, in the majority (93%) of cases, the rings remained unperturbed throughout the object's lifetime.

In general, the encounter severity is related to the minimum approach distance, d_{min}, between the ringed body and the planet. In Wood et al. (2017), a severity scale was introduced for close encounters between a ringed small body and a planet by comparing d_{min} to the critical distances of the Roche limit, tidal disruption distance, Hill radius and a new quantity called the "ring limit". The ring limit was loosely defined as the upper limit on the value of d_{min} for close encounters between Chariklo and a giant planet which had a noticeable effect on a ring. This ring limit was set to a crude constant value of 10 tidal disruption distances which ignored velocity effects.

In this work, we seek to refine the definition of the ring limit and find analytical solutions for it for special cases in the three-body planar problem (small body, planet, ring particle). We use the technique of numerical integration to simulate close encounters between hypothetical one-ringed bodies and each of the giant planets. In this manner, we determine the ring limit for Centaurs moving on hyperbolic and parabolic orbits around the planet.

We study the ring limit as a function of small body mass, planet mass, ring orbital radius and the velocity at infinity of the Centaur's orbit about the planet. We then investigate whether our results can be applied to close encounters between Chariklo and Jupiter in the seven-body non-planar problem (Sun, four giant planets, Chariklo, and ring particle).

This paper is partitioned as follows: in section 2 we describe the properties of Chariklo, Chiron and Haumea along with their rings; in section 3 present the theory of close encounters; in section 4 describe our experimental method; in section 5 present our results and summarise our conclusions in section 6.

2. THE PROPERTIES OF CHARIKLO, CHIRON, HAUMEA AND THEIR RINGS

Though Chiron was discovered over four decades ago, Chariklo and Haumea were discovered much more recently. The Spacewatch program discovered Chariklo in 1997 (Scotti & Williams 1997) in an orbit between Saturn and Uranus with a semi-major axis of 15.8 au.

Prior to the occultation event that led to the detection of Chariklo's rings, its size was poorly constrained, with literature values ranging from 118 - 151 km. The occultation observations (Braga-Ribas et al. 2014) suggested that Chariklo is likely oblate with an equivalent radius of 127 km - a value in strong agreement with the 124

Table 1. The orbital and physical properties of Chariklo. The orbital data is based on an observational arc length of 10,540.2 days. The epoch is 58000.0 MJD. [1] = The AST-DYS website (see footnote), [2] = (Sicardy et al. 2016), [3] = (Jewitt & Kalas 1998) [4] = (Groussin et al. 2004).

Property	Value	Ref
a	15.8218 ± 0.0000 au	[1]
e	0.172092 ± 0.000002	[1]
i	23.382 ± 0.000 deg	[1]
Ω	300.416 ± 0.000 deg	[1]
ω	242.896 ± 0.000 deg	[1]
M	77.67 ± 0.00 deg	[1]
Density	800 kgm^{-3} - $3{,}000$ kgm^{-3}	[2]
Mass	6×10^{18} kg - 3×10^{19} kg	[2]
Radius	118 ± 6 km - 151 ± 15 km	[3][4]

$\pm$ 9 km value obtained by those authors on the basis of thermal modeling.

Haumea was discovered in 2004 by Mike Brown and his adaptive optics team[2]. In 2005, the same team discovered two small moons orbiting Haumea[3]. The existence of the moons allowed the mass of Haumea to be better constrained than those of Chariklo and Chiron.

The orbital and physical properties of Chariklo, Chiron and Haumea are shown in Tables 1, 2 and 3 respectively. Orbital values were taken from the ASTDYS website[4][5][6]. a, e, i, Ω, ω, M are the semi-major axis, eccentricity, inclination, longitude of ascending node, argument of perihelion and mean anomaly respectively.

Where radius and density values are poorly known, they are presented as suspected ranges with no uncertainties. The mass range of Chiron was calculated using the radius and density ranges assuming a spherical body. In the case of Haumea, the mass was determined using a model of Haumea with its two satellites.

The properties of the rings (or supposed rings) of Chariklo, Chiron and Haumea are shown in Table 4.

3. THE THEORY OF CLOSE ENCOUNTERS

Table 2. The orbital and physical properties of Chiron. Orbital data are based on an observational arc length of 44,773.2 days. The epoch is 58000.0 MJD. The mass range was calculated using the density and radius ranges assuming a spherical body. [1] = the ASTDYS website, [2] = (Meech & Svoren 2004), [3] = (Groussin et al. 2004) [4] = (Sykes & Walker 1991).

Property	Value	Ref
a	13.6482 ± 0.0000	[1]
e	0.382254 ± 0.000000	[1]
i	6.95 ± 0.00 deg	[1]
Ω	209.201 ± 0.000 deg	[1]
ω	339.677 ± 0.000 deg	[1]
M	153.579 ± 0.000 deg	[1]
Density	500 kgm^{-3} - 1,000 kgm^{-3}	[2]
Mass	7.50×10^{17} kg - 2.70×10^{19} kg	-
Radius	71 ± 5 km - 186 km	[3][4]

Table 3. The orbital and physical properties of Haumea. Orbital data are based on an observational arc length of 22,795 days. The epoch is 58000.0 MJD. [1] = the ASTDYS website, [2] = (Lacerda & Jewitt 2007), [3] = (Ragozzine & Brown 2009), [4] = (Rabinowitz et al. 2006).

Property	Value	Ref
a	43.3542 ± 0.0008 au	[1]
e	0.189388 ± 0.000015	[1]
i	28.204 ± 0.000 deg	[1]
Ω	121.971 ± 0.000 deg	[1]
ω	238.869 ± 0.002 deg	[1]
M	214.066 ± 0.003 deg	[1]
Density	2,600 kgm^{-3}	[2][4]
Mass	$4.006 \pm 0.040 \times 10^{21}$ kg	[3]
Radius	$500 \times 750 \times 1,000$ km	[4]

3.1. DETERMINING THE VELOCITY AT INFINITY OF THE ORBIT OF THE SMALL BODY

Given the growing number of small Solar system bodies being found to have rings, it is interesting to consider the effect of close encounters between those objects and the giant planets on their ring systems. How close must an encounter be before the influence of the planet on a ring is noticeable? One solution to this problem would be to carry out exhaustive N-body dynamical studies for every object found to have rings (such as those detailed in Wood et al. (2017) and Wood et al. (2018)). How-

ever, should many such objects be discovered, such simulations would eventually prove prohibitive, given their computationally intensive nature.

It is therefore important to examine whether it is possible to develop a criterion by which the stability (or otherwise) of small-body rings can be assessed, in the context of the close encounters they will experience throughout their lifetimes. Previously we built such a criterion in Wood et al. (2017) which was based entirely upon the idea that the severity of a given encounter is determined by the strength of the tidal effects on the small body's ring system. Thus, the severity only depended on d_{min}.

However, the severity also depends on the velocity at infinity, v_∞, of the small body relative to the planet. v_∞ has little meaning for an elliptical orbit, however, in the overwhelming majority of cases, a small body undergoing a close encounter with a giant planet will follow a parabolic or hyperbolic path with respect to that planet, rather than being captured by it. For this reason, we therefore consider just parabolic and hyperbolic orbits in this work.

If the orbit of the small body relative to the planet is parabolic or hyperbolic, then for a given planet and small body mass in the planar problem, the orbit is defined by v_∞ and d_{min}.

Hyodo et al. (2016) show the derivation of v_∞ for the case in which the planet is restricted to a circular orbit about the Sun in this planar three-body problem. The reader is referred to that work for details. Given a small body and a planet both in orbit about the Sun and having a close encounter, the resulting equations are:

$$v_\infty^2 = v_r^2 + (v_\omega - v_K)^2 \tag{1}$$

where v_r and v_ω are the radial and azimuthal velocities respectively of the small body at the orbital distance of the planet from the Sun; and v_K is the Keplerian velocity of the planet in its orbit about the Sun. v_r and v_ω are given by:

$$v_r = v_K \sqrt{2 - \frac{a_o}{a} - \frac{a(1-e^2)}{a_o}} \tag{2}$$

$$v_\omega = v_K \sqrt{\frac{a(1-e^2)}{a_o}} \tag{3}$$

where a is the semi-major axis of the orbit of the small body, a_o is the semi-major axis of the orbit of the planet, and e is the eccentricity of the orbit of the small body about the Sun.

3.1.1. THE PROPERTIES OF PARABOLIC AND HYPERBOLIC ORBITS

Table 4. The properties of the rings (or supposed rings) of Chariklo, Chiron and Haumea. [1] = (Braga-Ribas et al. 2014), [2] = (Ortiz et al. 2015), [3] = (Ortiz et al. 2017).

Object	Inner Ring (km)	Outer Ring (km)	Widths (km)	Ref
Chariklo	390.6 ± 3.3	404.8 ± 3.3	7.17 ± 0.14; 3.4 +1.1 -1.4	[1]
Chiron	324	-	10	[2]
Haumea	2,287	-	70	[3]

The general formula for the trajectory of an object in a hyperbolic or parabolic orbit is given by:

$$r_{radial} = \frac{h^2}{\mu} \frac{1}{1 + e_s \cos(\theta - \theta_o)} \tag{4}$$

where r_{radial} and $\theta - \theta_o$ are the radial and angular positions of the small body, respectively, with the encountered planet located at one of the focii. θ_o is chosen in such a manner that the minimum approach distance occurs when $\theta - \theta_o = 0$.

Here, $\mu = G(M_p + m_s)$, G is the gravitational constant, M_p is the mass of the planet, m_s is the mass of the small body, h is the constant angular momentum per unit mass of the small body (angular momentum/small body mass) and e_s is the eccentricity of the orbit of the small body about the planet (not to be confused with e).

For a parabolic orbit, $e_s = 1$ and $v_\infty = 0$. For a given planet and small body mass, μ is constant, and a parabolic orbit is completely defined if d_{min} is known. Then h is given by:

$$h = \sqrt{2\mu d_{min}} \tag{5}$$

The velocity of an object moving in a parabolic orbit as a function of radial position is given by:

$$v = \sqrt{\frac{2\mu}{r_{radial}}} \tag{6}$$

For a hyperbolic orbit, $e_s > 1$ and $v_\infty > 0$. For any hyperbolic orbit the following relation applies:

$$d_{min} v_\infty^2 = \mu(e_s - 1) \tag{7}$$

Thus, if d_{min} and v_∞ are known, then e_s can be found. Then, substituting d_{min} in for r_{radial} in equation 4 yields:

$$d_{min} = \frac{h^2}{\mu} \frac{1}{1 + e_s} \tag{8}$$

from which h can be found. For any given r_{radial}, the velocity can therefore be found from:

$$v = \sqrt{\mu \left(\frac{2}{r_{radial}} + \frac{v_\infty^2}{\mu} \right)} \tag{9}$$

(Bate et al. 1971; Murray & Dermott 1999)

3.2. CRITICAL DISTANCES AND THE RING LIMIT

We define the ring limit, R, as the value of the minimum approach distance for close encounters between a planet and a ringed small body in a hyperbolic or parabolic orbit about the planet in the three-body planar problem for which the effect on the ring is just noticeable following the criterion of Araujo et al. (2016) for a just noticeable encounter.

The ring limit then defines a boundary between a noticeable and non-noticeable effect. This makes R distinct from the Hill radius, R_H, tidal disruption distance, R_{td}, and Roche limit, R_{roche}, as each of these involves a balance of forces.

For reason of comparison, it is beneficial to discuss these critical distances in more detail. The Hill radius of a less massive body with respect to a more massive body can be defined as the distance from the less massive body within which a satellite may orbit.

If the satellite orbit is within the Hill radius then the less massive body-satellite binary cannot be disrupted by tidal forces due to the more massive body. In the case for which the more massive body is a planet and the less massive body a small body of the Solar system, the Hill radius of the small body with respect to the planet is approximately given by:

$$R_H \approx R_{radial} \left(\frac{m_s}{3M_p} \right)^{\frac{1}{3}} \tag{10}$$

(e.g. Murray & Dermott 1999) where m_s is the mass of a small body, M_p the mass of the planet and R_{radial} the radial distance between the small body and the planet. Thus, during a close encounter between a ringed small body and a planet, the distance of orbiting ring particles from the small body must be less than that small body's Hill radius with respect to the planet in order for the ring particles to remain in orbit. Analogously the satellite of a planet must remain within the planet's Hill radius with respect to the Sun.

If a ringed small body is at a distance just within the tidal disruption distance from a planet, tidal forces can

disrupt a small body-ring particle binary pair instantaneously. The tidal disruption distance for a binary consisting of a small body and a massless ring particle in a circular orbit of radius r about the small body is given by:

$$R_{td} \approx r \left(\frac{3M_p}{m_s} \right)^{\frac{1}{3}} \qquad (11)$$

(Agnor & Hamilton 2006; Philpott et al. 2010). For example, when Chariklo is just within the tidal disruption distance to a planet, a ring particle is just outside Chariklo's Hill radius with respect to the planet.

There is one more critical distance to consider. At an even closer distance to a planet is the Roche limit - the distance from a more massive body (the primary body) within which a much less massive body (the secondary body) held together only by gravity can be torn apart by tidal forces. For a rigid secondary body, the equation for the Roche limit with respect to a primary body is approximately:

$$R_{roche} \approx 1.44 R_p \left(\frac{\rho_p}{\rho_s} \right)^{\frac{1}{3}} \qquad (12)$$

where R_p is the physical radius of the primary body, ρ_p is the density of the primary body and ρ_s is the density of the secondary body (e.g. Jeans 1928; Jeffreys 1947; Murray & Dermott 1999).

To give the reader a feel for the relative scales of these three parameters, we calculate the Hill radius of a planet with respect to the Sun, tidal disruption distance, and Roche limit using a Chariklo mass of 8×10^{18} kg and ring orbital radius set to that of the outer ring of Chariklo of 405 km for each of the four giant planets.

The Roche limits of Chariklo with respect to each giant planet were calculated for the case in which the density of Chariklo equals the density of the planet. Planetary radii were obtained from NASA[7]. The masses of the four giant planets were taken from the NASA JPL HORIZON ephemeris[8]. The results are shown in Table 5.

We now present in Table 6 our previously developed severity scale for a close encounter between a ringed small body and a planet based on the value of d_{min} relative to the Hill radius of the planet with respect to the Sun, ring limit, tidal disruption distance and Roche limit.

[7] http://solarsystem.nasa.gov/planets

[8] http://ssd.jpl.nasa.gov/horizons.cgi?s_body=1#top (accessed 31st December 2015) for epoch Jan 1, 2000, at 0:00 UT

Here, our aim is to define a more accurate/refined ring-limit distance resulting in a more rigorous quantitative close-encounter severity scale in the planar 3-body problem. In our previously published scale for the seven-body problem, only a constant value of 10 tidal disruption distances was used for the ring limit (Wood et al. 2017).

Unlike the critical distances, no simple equation for R is available. We expect that R should be a function of planet mass, small body mass, relative small body velocity at infinity, and ring orbital radius. This would be a five dimensional problem. However, if any two of the five quantities are held constant, the problem becomes one in only 3 dimensions. One example of this would be to hold the planet mass and small body mass constant while varying the other variables.

We theorize that the mathematical form of an equation for R in this 3D problem can be written as a factor f of the tidal disruption distance:

$$R = f R_{td} = f r \left(\frac{3M_p}{m_s} \right)^{\frac{1}{3}} \qquad (13)$$

where $f > 1$. This is justified because the impact of an encounter on the ring will become noticeable at a greater distance than that at which the orbit of a ring particle would be completely disrupted.

We expect f to be a function of the orbital radius, velocity at infinity, mass of the small body and mass of the planet. Thus, $f = f(r, v_\infty, m_s, M_p)$. f is dimensionless but can be thought of as the value of the ring limit expressed in units of tidal disruption distances.

For close encounters with any particular planet, M_p is constant, and this problem can be simplified even further by holding any two of the variables r, v_∞, and m_s constant.

Given these variables, we can use numerical integrations to quantify the value of f, and therefore work towards a standard formulism for the ring limit.

4. NUMERICAL METHOD

As the three - or more - body problem cannot be solved analytically, computers have been used to numerically approximate such systems using integration. Over the decades, computing power has continued to increase allowing for more and more robust simulations in areas such as Solar system dynamics, exoplanets, star clusters and even galactic astronomy (Horner & Jones 2010; Wang et al. 2015; Horner & Wittenmyer 2018; Benson et al. 2016). In this work we make use a relatively new integrator in an attempt to find specific analytical solutions for the ring limit.

Table 5. Approximate Roche limits, tidal disruption distances and Hill radii for Chariklo for the four giant planets using a Chariklo mass of 8×10^{18} kg, density equal to the density of each planet and a ring orbital radius of 405 km. Hill radii were calculated for each giant planet with respect to the Sun.

Planet	Roche Limit (km)	Tidal Disruption Distance (km)	Hill Radius (km)
Jupiter	101,000	362,000	5.30×10^7
Saturn	84,000	242,000	6.52×10^7
Uranus	37,000	129,000	6.99×10^7
Neptune	35,000	137,000	1.16×10^8

Table 6. A scale ranking the close encounter severity between a ringed small body and a planet based on the minimum distance obtained between the small body and the planet, d_{min}, during the close encounter taken from Wood et al. (2017). R_H, R, R_{td} and R_{roche} are the Hill radius of the planet with respect to the Sun, ring limit, tidal disruption distance and Roche limit respectively. For that work, the ring limit was set to a constant value of 10 tidal disruption distances.

d_{min} Range	Severity
$d_{min} \geq R_H$	Very Low
$R \leq d_{min} < R_H$	Low
$R_{td} \leq d_{min} < R$	Moderate
$R_{roche} \leq d_{min} < R_{td}$	Severe
$d_{min} < R_{roche}$	Extreme

4.1. Initialising the Simulations

In order to explore the complicated five-parameter problem in three dimensions, we used the technique of numerical integration of the three-body planar problem (small body, giant planet, ring particle) to simulate close encounters between giant planets and small one-ringed bodies in hyperbolic or parabolic orbits about a planet.

Before any integrations could be made, quantities such as initial distance and time step needed to be determined. To accomplish this, dozens of pre-runs were made in the three-body problem using the IAS15 integrator in the REBOUND N-body simulation package (Rein & Liu 2012; Rein & Spiegel 2015).

Based on the results from these pre-runs it was decided that an adaptable time step of 0.001 year would be used which would automatically adjust itself during the event of a close encounter.

Determining the initial distance of a small body from a planet is tricky. If the initial distance chosen is too close, then the close encounter is too brief to noticeably alter the orbit of a ring particle when otherwise it would. If the initial distance chosen is too large, then much

computation time is wasted as the small body makes it way toward the planet.

After a significant amount of benchmarking, we chose to begin our simulations with the ringed small body located one Uranus Hill radius away from Jupiter, Saturn and Uranus. For Neptune, the ringed small body began the simulation at a distance of one Neptune Hill radius from the giant planet. These initial conditions represented the optimal compromise between the length of arc on a given encounter and the amount of computational time required for the simulations. It was decided that a simulation would be terminated after the planet-small body distance went beyond the initial distance after the close encounter occurred.

Following Hyodo et al. (2016) the range $0 \leq v_{\infty} \leq 9$ km/s was chosen as the range for the velocity at infinity for Centaurs in orbits with $e \leq 0.9$ about the Sun as this range overlapped the v_{∞} range for all four giant planets.

For the small body mass range, we wanted a range that allowed the dependence of the ring limit on small body mass to be fully explored and included masses large enough to retain rings. It was decided that the small body masses would range from just above the mass of Chariklo to the mass of Pluto. The range chosen was 2×10^{20} kg $\leq m_s \leq 1.309 \times 10^{22}$ kg (the mass of Pluto[9]) which includes the mass of Haumea but not Chiron or Chariklo. We consider this mass range to be in the realm where $M_p \gg m_s$ as the planet masses are $> 10^6$ times larger than any small body mass in the range.

It was not necessary to include the mass of Chariklo or Chiron in this mass range since we could always be extrapolate to find ring limit values for other masses. Furthermore, a great many Centaurs likely remain undiscovered (Horner et al. 2004b) and therefore their masses are unknown.

When choosing a range for the ring orbital radii, we wanted a range large enough so that the dependence of the ring limit on r could be fully explored but small

[9] http://solarsystem.nasa.gov/planets/pluto/facts (accessed 19 February 2017)

enough so that the rings would lay well within the Hill radius of the small body with respect to the Sun. We also wanted the range to be much larger than currently known orbital radii. The reasons for this were two fold. First, we wanted to find an upper bound on the ring limit for a given small body mass and v_∞ to be used in a severity scale. And second, we wanted the range to be very large so that it would include orbital radii of any undiscovered ringed Centaurs.

We calculated Hill radii with respect to the Sun for the lower and upper bounds of our small body mass range for orbits with semi-major axes at the bounds of the Centaur region.

It was decided that a range of 25,000 km $\leq r \leq$ 100,000 km would be used. For this range, the rings would always be within 0.4 Hill radius of any mass and would never drop below 0.001 Hill radius. As a comparison, the outer ring of Chariklo is at 0.00156 Hill radius.

We decided that a total of 100 massless test particles would be used to simulate the ring if $r < 50,000$ km and 500 massless test particles would be used if 50,000 km $\leq r \leq 100,000$ km. It was decided that these numbers of test particles worked best based on results from the pre-runs.

For example, for r values in the range 50,000 km $\leq r \leq 100,000$ km it was found that changing the number of ring particles from 500 to 1,000 did not have a significant effect on the values of the ring limits determined so using only 500 particles was good enough. In each simulation, the ring particles were initially evenly distributed throughout the same circular orbit about the small body.

4.2. *Determining the Ring Limit*

To determine a ring limit value for any set of values of m_s, r, v_∞ and the mass of the planet in question, a close encounter between the small body and planet was simulated starting with the previously described initial conditions and an initial guess at the value of d_{min}. After the simulation, Δe_{max} was then determined from the simulation output.

If $\Delta e_{max} = 0.01$ then d_{min} is equal to the ring limit. To numerically approximate this, a tolerance, ϵ, was used such that if $|\Delta e_{max} - 0.01| < \epsilon$ then the ring limit was set equal to d_{min} and recorded in units of both kilometers and tidal disruption distances.

If however $|\Delta e_{max} - 0.01|$ was not within this certain tolerance then the close encounter was run again with d_{min} increased/decreased if $\Delta e_{max} - 0.01$ was positive/negative. This process was continued until $|\Delta e_{max} - 0.01|$ was within the certain tolerance.

The tolerances used were 1×10^{-5} if $R_{td} > 1,000,000$ km and 1×10^{-4} otherwise. The use of these different tolerances made R accurate to within 1,000 km in each case. For each value of r used for each small body mass, 46 measurements of R were made each using a different value of velocity at infinity chosen from the range 0 km/s $\leq v_\infty \leq 9$ km/s.

4.3. *The Ring Limit in Three Dimensions*

To determine an analytical solution for the ring limit, we needed to discover the mathematical relationship between the ring limit and each of the four variables - small body mass, planet mass, ring orbital radius and velocity at infinity. Our strategy was to hold two variables constant, plot our data in three dimensional phase space to create 3D structures and then use 2D slices of those structures while holding a third quantity constant to determine the mathematical relationship between the ring limit and the fifth variable.

Two major sets of integrations were performed one with the small body mass held constant and the other with the ring orbital radius held constant. Then for each major integration, the data was analyzed by holding the planet mass constant. In this way, three-dimensional structures were created from the data of each major integration.

4.3.1. *The Ring Limit as a Function of Velocity at Infinity, Ring Orbital Radius and Planet Mass*

In the first set of major integrations, we held the mass of the small body constant by setting it equal to the mass of Pluto (we will henceforth refer to a small body with the mass of Pluto as a Pluto-like body). Next, the mass of the planet was held constant and then the integrations were performed. This was done for each giant planet, and the data from those integrations was used to create four 3D structures in $R - r - v_\infty$ space. Up to 20 values of r and 46 values of v_∞ were chosen from the previously described ranges. The number of simulations totaled between 700 - 920 per planet.

In our initial simulations, we were unsure of how many would be needed to obtain a clear result. After several trials, it was realised that 700 simulations per scenario was sufficient to give an accurate value, and all future trials were run in this manner. The data from the extra simulations carried out in our earliest work were kept, which explains those cases where up to 920 simulations were carried out.

4.3.2. *The Ring Limit as a Function of Small Body Mass and Velocity at Infinity*

Another major set of integrations was performed with the ring orbital radius set to a constant value of 50,000 km and the mass of the planet set to the mass of Jupiter.

It was not necessary to extend these integrations to every planet since planet mass was varied in the other previously mentioned major set of integrations. Using data from these integrations, a 3D structure in $R - m_s - v_\infty$ space was created.

4.4. *The Ring Limit in Two Dimensions*

The ring limit can be studied in two dimensions by using 2D slices of 3d structures while holding a third variable constant everywhere in the slice. The ring limit's dependence on the planet mass was found by combining all four 3D structures in $R - r - v_\infty$ space into one superstructure. Then the intersection of 2D slices of constant ring orbital radius and velocity at infinity allowed the planet mass dependence to be determined.

2D slices of $R - r - v_\infty$ structures were made for each planet using a constant value of v_∞ and planet mass for each slice. Within each slice, R varied only with r. Then for each slice, a regression was done on R and r values to determine the best-fitting curve. This was done for each of the 46 different slices per r per planet.

2D slices of each $R - r - v_\infty$ structure were also made using a constant value of r and planet mass for each slice. Within each slice, R varied only with v_∞. Then for each slice, a regression was done on R and v_∞ values to determine the best-fitting curve. Up to 20 different 2D slices of constant r were made per planet.

Using an analogous technique, 2D slices of our plot in $R - m_s - v_\infty$ space were made using a constant value of planet mass along with either a constant m_s or v_∞ for each slice. Each slice was studied using regression. 18 slices were made with a constant m_s and 46 with a constant v_∞ for each m_s value. The entire analysis plan is shown in Figure 1.

4.5. *Applying Results to the Seven-body Non-planar Problem*

Finally, we extrapolated to find ring limit upper bound values for close encounters between Chariklo and Jupiter and compared those to d_{min} values reported by Araujo et al. (2016) for the seven-body non-planar problem.

5. RESULTS

5.1. *The Ring Limit in Three Dimensions*

Figure 2 shows examples of plots of our data in $R - r - v_\infty$ space for each planet for close encounters with a Pluto-like body.

Figure 3 shows the same 3D graphs in a rotated view for all planets on one plot with different colors being

used for each planet. A series of islands of data points can be seen for each planet. The effect of planet mass on the ring limit can clearly be seen. Given a constant velocity at infinity and ring orbital radius, the ring limit increases with planet mass.

This result is not surprising. We know that a planet with a larger mass has a stronger gravitational pull than a planet with a smaller mass. Therefore, a planet with a larger mass is able to perturb the orbits of a small body's ring particles at a greater distance than a body with a smaller mass.

The intersection between 138 2D slices of the structure in Figure 3 with constant r and 138 2D slices with constant v_∞ were examined - forty-six with constant r = 30,000 km, forty-six with constant r = 50,000 km and forty-six with constant r = 100,000 km. The intersection of each 2D slice of constant v_∞ with each 2D slice of constant r revealed that the variation in R as a function of M_p could be accurately modeled by a power law of the form:

$$R \sim M_p^\gamma \tag{14}$$

The exponent γ ranged from 0.229 to 0.327. The maximum value of γ occurred for values of $v_\infty = 0$ km/s and $r = 100,000$ km. The minimum value of γ occurred for values of $v_\infty = 3.9$ km/s and $r = 100,000$ km. As an example, Table A1 gives values of γ as a function of velocity at infinity which can be used for close encounters between any giant planet and a small body with a mass equal to the mass of Pluto with ring orbital radius of 50,000 km.

Figure 4 shows the plot of our data in $R - m_s - v_\infty$ space for a constant ring orbital radius of 50,000 km and planet mass set equal to the mass of Jupiter. Table A2 gives ring limits for close encounters between Jupiter and a Pluto-like body with a ring orbital radius of 50,000 km for the range $0 \leq v_\infty \leq 9$ km/s.

5.2. *The Ring Limit in Two Dimensions*
5.2.1. *The Ring Limit Versus Velocity at Infinity*

2D slices of $R - r - v_\infty$ space using a constant value of r for each slice show that the mathematical relationship between R and v_∞ is too complex to fit into one form. In Figure 5 we show a typical example of a 2D slice of $R - r - v_\infty$ space at constant r for close encounters between the four giant planets and a Pluto-like body.

The top graph is for a constant r value of 100,000 km, and the bottom for a constant r value of 30,000 km. Usually the ring limit increases with v_∞, but in the top graph R decreases with increasing v_∞ for values above 7 km/s for Uranus and 7.75 km/s for Neptune. In the bottom graph R increases with increasing v_∞ over all
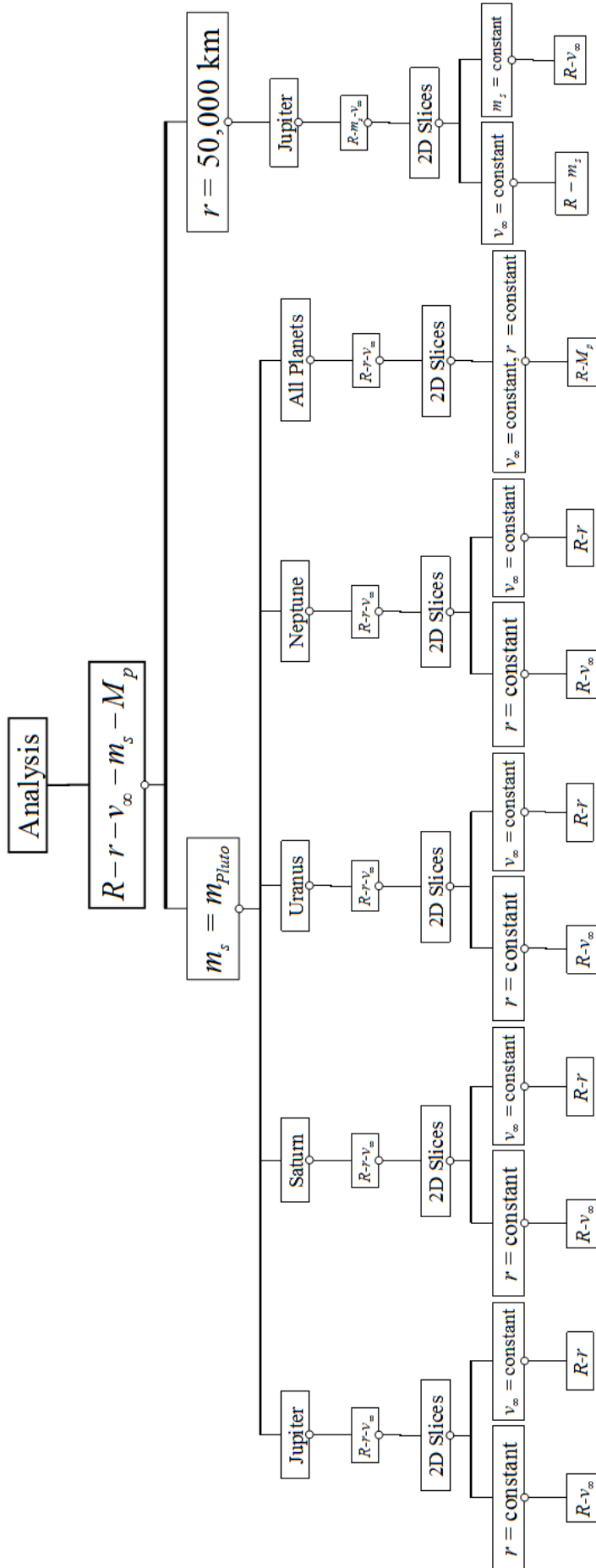
Figure 1. This map shows how the two dimensional slices of the data are created.
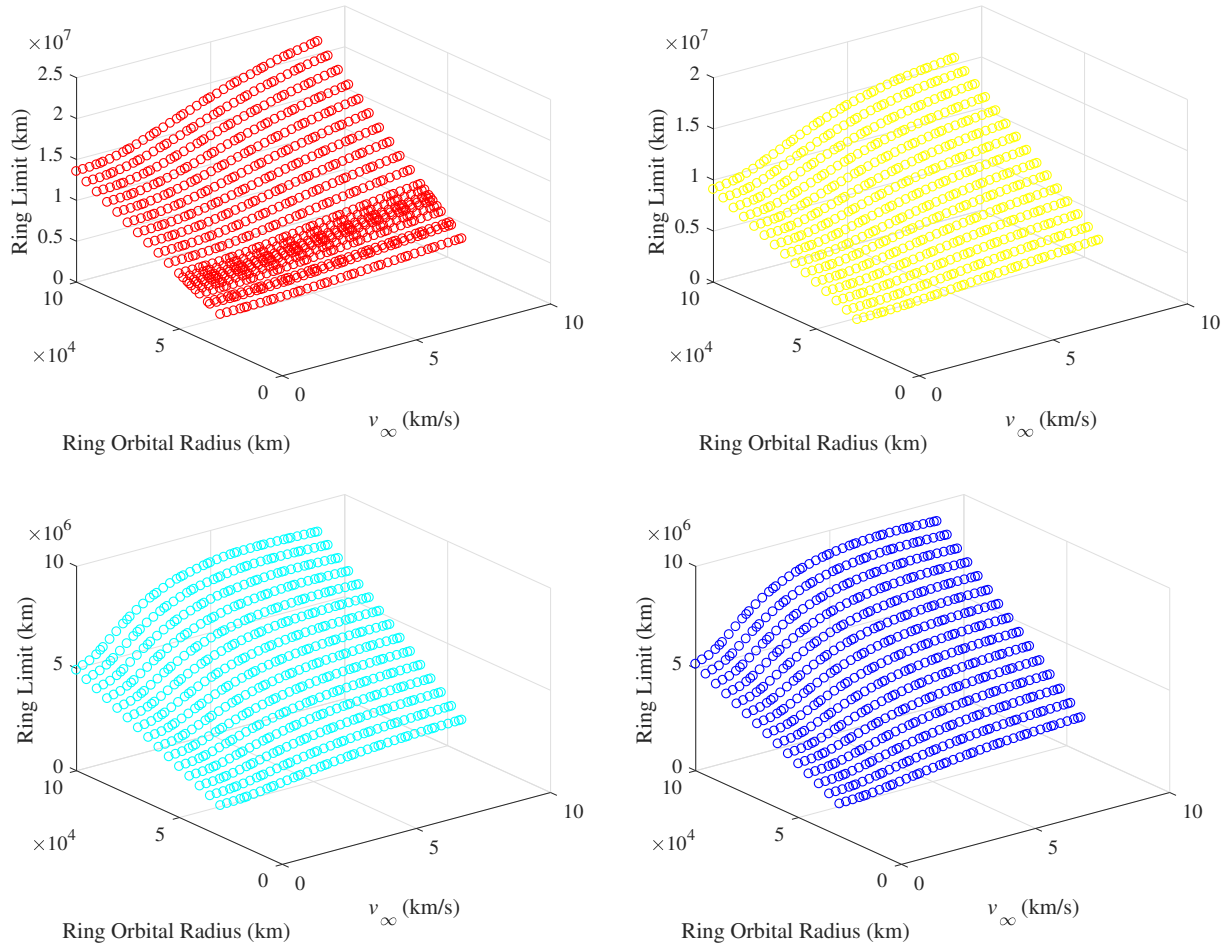
Figure 2. Plots of our data in $R - r - v_\infty$ space for each planet for close encounters with a Pluto-like body. Jupiter's graph is to the upper left, Saturn's the upper right, Uranus' to the lower left and Neptune's to the lower right. The color scheme Jupiter - red, Saturn - yellow, Uranus - cyan, and Neptune - blue will be used here and in the next three figures.
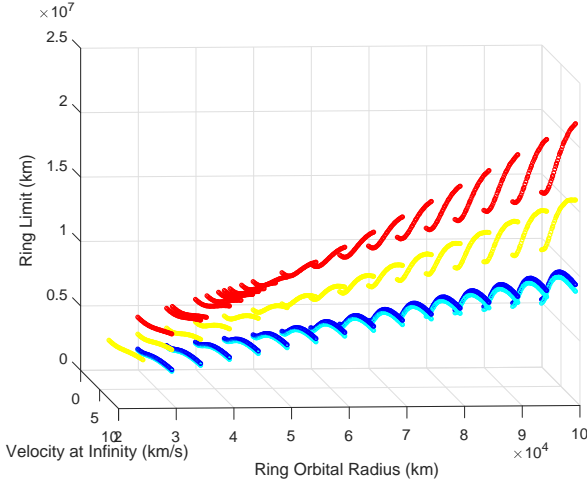
Figure 3. Plots of our data in $R - r - v_\infty$ space color coded by planet for close encounters with a Pluto-like body. The colors by planet are Jupiter - red, Saturn - yellow, Neptune - blue and Uranus - cyan.
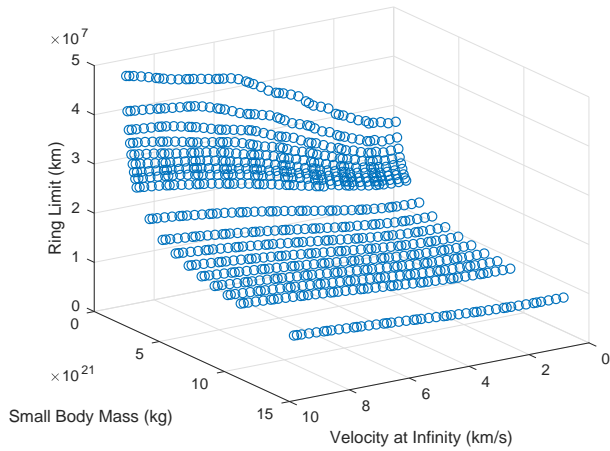
Figure 4. The plot of our data in $R - m_s - v_\infty$ space for a constant ring orbital radius of 50,000 km and planet mass equal to the mass of Jupiter.

values. The y intercepts of graphs of this type increase with the mass of the planet.

The plots for Uranus and Neptune seem to plateau at higher velocities while those of Jupiter and Saturn less so. We speculate that the plots of Jupiter and Saturn may also plateau but at higher velocities outside the range of this study.

5.2.2. *The Ring Limit Versus Ring Orbital Radius*

2D slices of $R - r - v_\infty$ space using a constant value of v_∞ for each slice show that R varies with r according to a power law of the form:
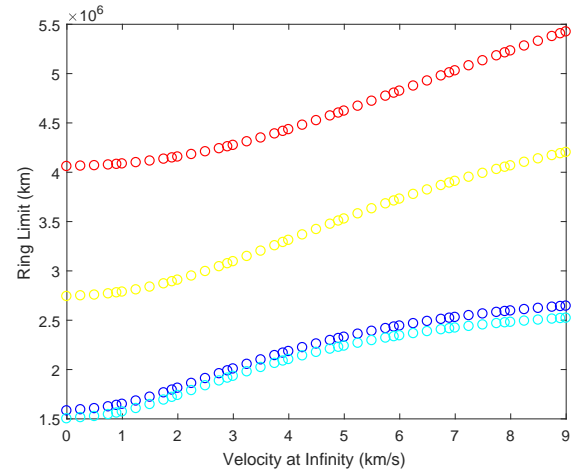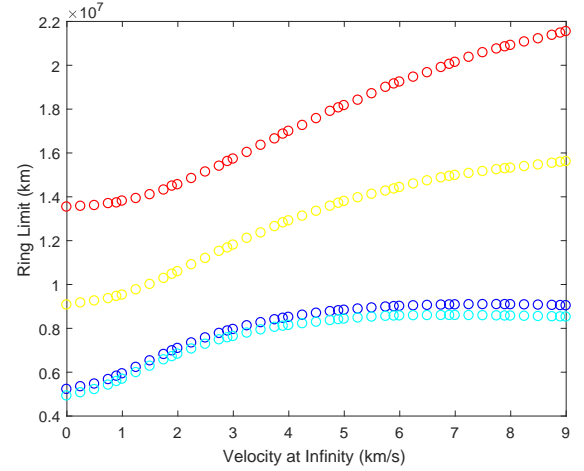
Figure 5. The ring limit as a function of velocity at infinity for a constant ring orbital radius of 100,000 km (top) and 30,000 km (bottom) for close encounters between a Pluto-like body and Jupiter (red), Saturn (yellow), Neptune (blue) and Uranus (cyan). Usually the ring limit increases with v_∞ but in the top graph R decreases with increasing v_∞ for values above 7 km/s for Uranus and 7.75 km/s for Neptune. In the bottom graph R increases with increasing v_∞ over all values. Thus, the mathematical relationship between R and v_∞ is too complex to fit into one form. The y intercepts of graphs of this type increase with the mass of the planet.

$$R \sim r^\alpha \qquad (15)$$

with the exponent α varying with the value of v_∞ used for the slice. Figure 6 shows the behavior of α with varying v_∞. Each value of α was found from a regression on twenty data points in $R - r$ space over a ring orbital radius range of 30,000 km - 100,000 km while holding the velocity at infinity constant. α increases with increasing v_∞ over a range of zero to 7.5 km/s and then decreases with increasing v_∞ over a range of 7.5 km/s to 9 km/s. α

values for close encounters between Jupiter and a Pluto-like body can be seen in Table A3.

For slices with v_∞ approaching zero (a parabolic orbit), α approaches 1.0. This means that for parabolic orbits, the ring limit varies linearly with r.

Figure 7 shows two examples of 2D slices of the ring limit versus ring orbital radius for close encounters between Jupiter and a Pluto-like body. The top slice is for a constant v_∞ of 9 km/s. The best-fit curve is shown and corresponds to an α value of 1.15. The square regression coefficient is 0.999.

The bottom slice is for a constant $v_\infty = 0.25$ km/s. The best-fit curve is shown and corresponds to an α value of 1.0007. The square regression coefficient is 0.9999.
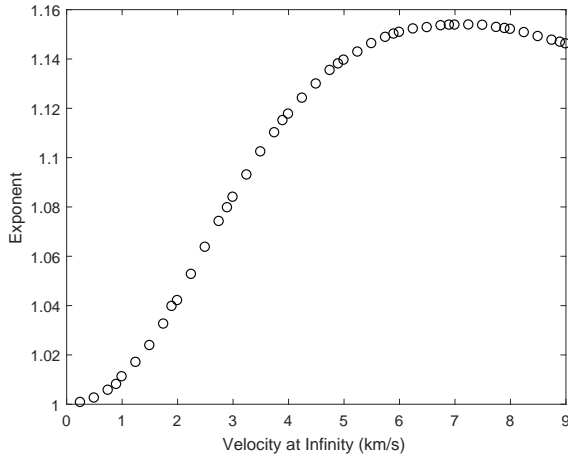
Figure 6. 2D slices of $R-r-v_\infty$ space using a constant value of v_∞ for each slice show that the ring limit varies with ring orbital radius according to a power law of the form $R \sim r^\alpha$ with the value of α varying with the value of v_∞ used for the slice. This graph shows the best-fit exponent, α, versus the constant value of v_∞ used for the slice for close encounters between Jupiter and a Pluto-like body. α increases with increasing v_∞ over a range of zero to 7.5 km/s and then decreases with increasing v_∞ over a range of 7.5 km/s to 9 km/s. Notice how as v_∞ approaches zero (a parabolic orbit), the best-fit exponent approaches 1.0. This means that for parabolic orbits, the ring limit varies linearly with r.

5.2.3. *The Ring Limit Versus Small Body Mass*

2D slices of $R-m_s-v_\infty$ space using a constant value of v_∞ for each slice show that R varies with m_s according to a power law of the form:

$$R \sim m_s^\beta \qquad (16)$$

One example is shown in Figure 8 for close encounters with Jupiter for a constant $v_\infty = 0.75$ km/s and ring
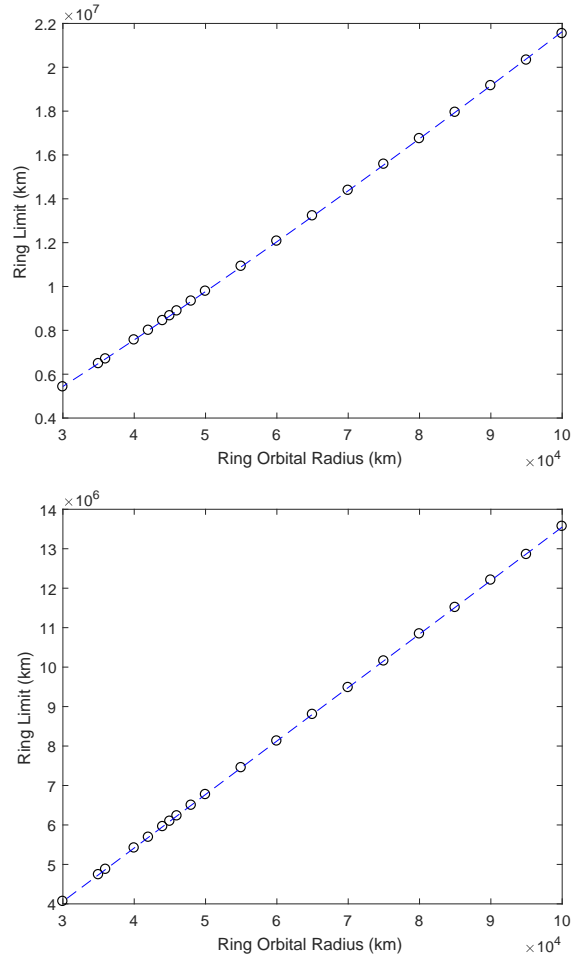
Figure 7. Top - ring limit versus ring orbital radius for a constant velocity at infinity of 9 km/s for close encounters between Jupiter and a Pluto-like body. Graphs of this type fit very well to a power law with the exponent on r approaching 1 as the velocity at infinity approaches zero (a parabolic orbit). In this graph, the best-fit exponent is 1.15, and the square regression coefficient is 0.999. The standard error is 0.002. Bottom - ring limit versus ring orbital radius for a constant velocity at infinity of 0.25 km/s for close encounters between Jupiter and a Pluto-like body. The exponent on r is 1.0007. The square regression coefficient is 0.9999. The standard error is 0.0005.

orbital radius = 50,000 km. In this example, β = -0.3340 and the square regression coefficient = 0.999.

For any particular 2D slice of this type, β depends on the value of v_∞ used for the slice. In our data, β varies between -0.39 to -0.33 with the value approaching -1/3 as the velocity at infinity approaches zero.

Figure 9 shows one example of how β varies with the velocity at infinity for close encounters with Jupiter using a constant ring orbital radius of 50,000 km. Each value of β was found using regression on eighteen data

points in $R - m_s$ space over a mass range of 2×10^{20} kg to the mass of Pluto (1.309×10^{22} kg) while holding the velocity at infinity constant. β decreases with v_∞ over a range from 0 km/s to about 5.5 km/s and increases with v_∞ over a range from 5.5 km/s to 9 km/s. Table A4 gives values of β for close encounters between Jupiter and small bodies each with a ring orbital radius of 50,000 km.

Figure 8. A 2D slice of ring limit versus small body mass for constant velocity at infinity = 0.75 km/s and constant ring orbital radius = 50,000 km for close encounters with Jupiter. The ring limit varies as a power law with the small body mass: $R \sim m_s^\beta$. In this example, β = -0.3340, and the square regression coefficient is 0.999. The standard error is 0.003.

5.2.4. *The Ring Limit Versus Velocity at Infinity Over a Range of Small Body Masses*

2D slices of $R - m_s - v_\infty$ space using a constant value of m_s show that no particular mathematical form can be used to describe how R varies with v_∞. Slices with the highest small body masses had more well defined plots compared to slices with the lowest masses.

Two examples are shown in Figure 10 for a constant small body mass of 2×10^{20} kg and 1.309×10^{22} kg (the mass of Pluto) for close encounters with Jupiter and ring orbital radius = 50,000 km.

The slice associated with the Pluto-like body is best fit to an exponential function with square regression coefficient of 0.993. The slice associated with the lower mass is best fit to a linear function and has a weaker fit with a square regression coefficient of 0.966.

5.3. *f, The Ring Limit Relative to the Tidal Disruption Distance*

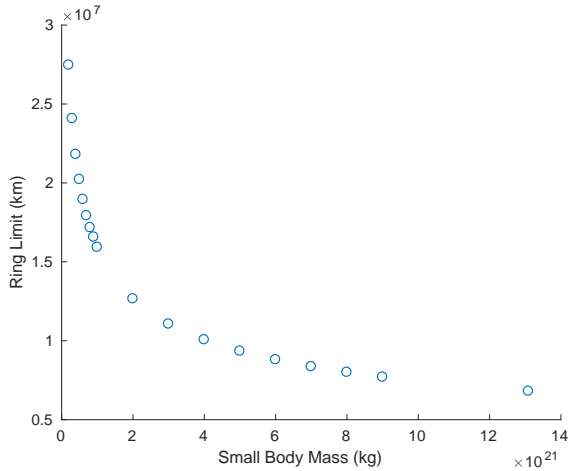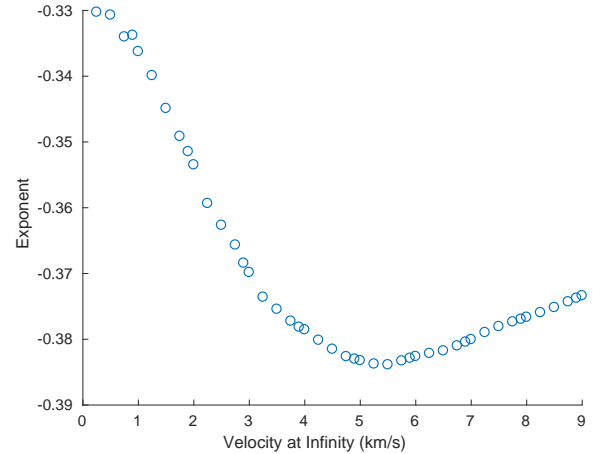**Figure 9.** For 2D slices of $R - m_s - v_\infty$ space using a constant value of v_∞ for each slice, the ring limit varies as a power law with small body mass in the form: $R \sim m_s^\beta$. Values for the best-fit exponent, β, vary with the value of the constant v_∞ used for the slice. This graph shows β versus the value of v_∞ used for the slice for close encounters with Jupiter. The ring orbital radius is held constant at 50,000 km. β decreases with v_∞ over a range from 0 km/s to about 5.5 km/s and increases with v_∞ over a range from 5.5 km/s to 9 km/s. The exponent approaches -1/3 as the velocity at infinity approaches zero.

5.3.1. *f Versus Velocity at Infinity*

Figure 11 shows twenty 2D slices of f versus v_∞ for twenty different values of constant r for close encounters between Jupiter and a Pluto-like body. Contours of constant ring orbital radius are color coded. Along a contour, f increases with v_∞. Two of the contours are shown in blue as a set of data points on a smooth curve.

The top contour is for a constant $r = 100,000$ km, and the bottom is for a constant $r = 30,000$ km. The higher the v_∞, the greater the range of f over all values of r. The largest value obtained by f is 2.84.

As v_∞ approaches zero, all contours converge onto nearly one line, making f nearly independent of r and linear with v_∞. The y intercept for all contours is approximately $f_{min} = 1.8$.

5.3.2. *f Versus Planet Mass*

Graphs analogous to Figure 11 for other planets have the same general shape but the average y intercept decreases with increasing planet mass as shown in Figure 12.

For each planet, an average y intercept was found by averaging up to 20 values of f each taken from a 2D slice of constant $v_\infty = 0$ in $R - r - v_\infty$ space for close encounters between that giant planet and a Pluto-like

Figure 11. Twenty 2D slices of f versus v_∞ for twenty different values of constant r per slice for close encounters between Jupiter and a Pluto-like body. Contours of constant ring orbital radius are color coded. Along a contour, f increases with v_∞. Two contours are shown in blue as a set of data points on a smooth curve. The top contour is for a constant $r = 100,000$ km, and the bottom is for a constant $r = 30,000$ km. The function f has a wider range for higher velocities but as v_∞ approaches zero, all contours converge onto nearly one line, making f nearly independent of r and linear with v_∞. The largest value obtained by f is 2.84. The y intercept for all contours is approximately 1.8.

Figure 10. Top - a plot of ring limit versus velocity at infinity for a constant ring orbital radius of 50,000 km and constant small body mass equal to the mass of Pluto for close encounters with Jupiter. The best fit is exponential with a square regression coefficient of 0.993. Bottom - an analogous plot for a constant small body mass of 2×10^{20} kg. Unlike the top plot, the bottom curve is less well fit and less smooth. The best-fit is linear with a square regression coefficient of 0.966.

body. It can be seen that the average y intercepts for the different planets all lie around 1.8.

5.3.3. *f Versus Ring Orbital Radius*

Figure 13 shows forty-six 2D slices of constant v_∞ for close encounters between Jupiter and a Pluto-like body. Contours of constant v_∞ are color coded. Along a contour, f generally increases with r. Two contours are shown in blue as a set of data points on a smooth curve. The top contour is a curve of constant $v_\infty = 9$ km/s, and the bottom is a curve of constant $v_\infty = 0$ km/s (parabolic orbits). The value of f along the top contour increases with increasing orbital radius, however,

the value of f along the bottom contour remains remarkably constant at a value around 1.8.

5.3.4. *f Versus Small Body Mass*

Figure 14 shows eighteen 2D slices of constant small body mass for close encounters with Jupiter. $r = 50,000$ km. Contours of constant v_∞ are color coded. Along a contour, f generally decreases with m_s. Two contours are shown in blue as a set of data points on a smooth curve. The top contour is a curve of constant $v_\infty = 9$ km/s, and the bottom is a curve of constant $v_\infty = 0$ km/s (parabolic orbits). The value of f along the bottom contour remains remarkably constant at a value around 1.8. The vertically aligned set of data points on the far right is for Pluto.

5.4. *Finding an Analytical Solution for the Ring Limit*

Figures 11 - 14 show that the lower bound of f is approximately equal to 1.8 tidal disruption distances and is nearly independent of the mass of the planet, the ring orbital radius and small body mass. Furthermore, Figure 11 also shows that the ring limit equals this lower
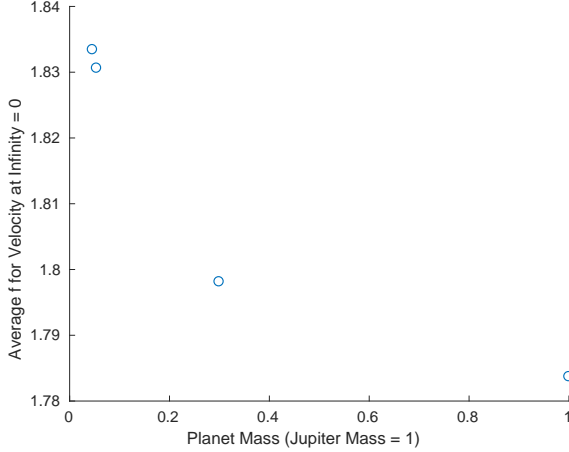
Figure 12. The average value of f for a constant $v_\infty = 0$ km/s (a parabolic orbit) for each giant planet for close encounters with a small body with the mass of Pluto. For each planet, an average f value was found by averaging all the values of f in a 2D slice of constant $v_\infty = 0$ in $R-r-v_\infty$ space. Ring orbital radii ranged from 25,000 km - 100,000 km. Up to 20 different ring orbital radii were used. For each planet, this average value of f corresponds to the lower bound of f and rounds off to 1.8 to two significant figures. The average value of f decreases with planet mass.

bound only for orbits with $v_\infty = 0$ (ergo for parabolic orbits only). We now define 1.8 tidal disruption distances as the approximate distance within which all encounters between a ringed small body and a giant planet are noticeable.

Thus, from equation (13), an analytical solution for the ring limit for parabolic orbits is:

$$R \simeq 1.8r \left(\frac{3M_p}{m_s} \right)^{\frac{1}{3}} \qquad (17)$$

For hyperbolic orbits, no one mathematical form for R could be found. However, analytical solutions for the ring limit could be found for specific cases. For example, a 2D slice of constant v_∞ of the plot of our data in $R - r - v_\infty$ space for the planet Jupiter in Figure 2 can be analysed using regression to obtain an analytical solution for R for close encounters between Jupiter and a Pluto-like body as a function of r over the range 30,000 km $\leq r \leq$ 100,000 km. The best fit solution for R in units of km for $v_\infty = 5$ km/s is:

$$R \simeq 36.3r^{1.1395} \qquad (18)$$

5.5. *Extrapolating the Data*
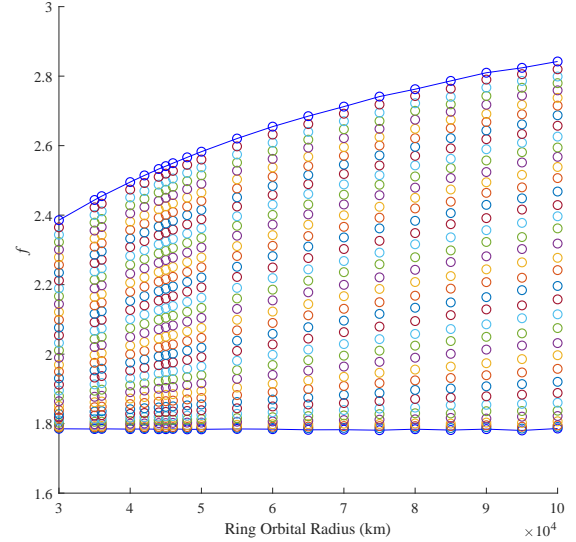
Figure 13. Forty-six 2D slices of constant v_∞ for close encounters between Jupiter and a Pluto-like body. Contours of constant v_∞ are color coded. Along a contour, f generally increases with r. Two contours are shown in blue as a set of data points on a smooth curve. The top contour is a curve of constant $v_\infty = 9$ km/s, and the bottom is a curve of constant $v_\infty = 0$ km/s (parabolic orbits). The value of f along the top contour increase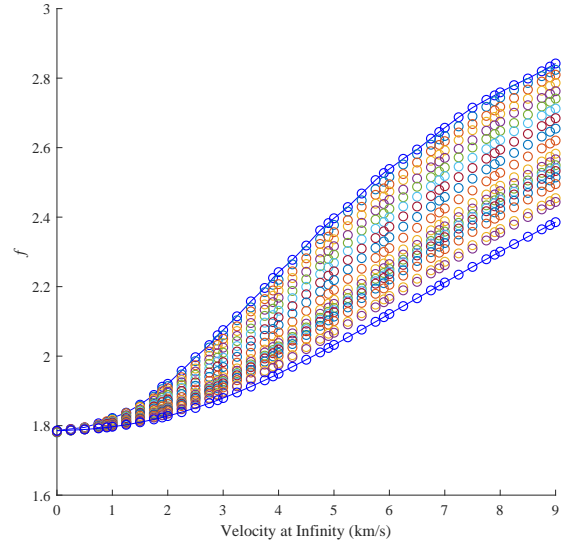s with increasing orbital radius, however, the value of f along the bottom contour remains remarkably constant at a value around 1.8.

Our data for the ring limits can be interpolated or extrapolated to determine ring limit values for close encounters not done in this study.

As an example, suppose you wanted to know the ring limit for a small body of mass 7.986×10^{18} kg with a ring orbital radius of 50,000 km and a velocity at infinity of 7.78 km/s for a close encounter with Jupiter. Call these the target mass, target velocity and target radius respectively. Call the ring limit for this body R_{target}. Here are the steps you would take:

- Using Table A2, find the ring limit for a Pluto-like body with a v_∞ value closest to the target v_∞. From the table, the closest v_∞ would be 7.75 km/s. Set the source mass, m_{source}, equal to the mass of Pluto.

- Use interpolation of our data in Table A2 to convert the ring limit for $v_\infty = 7.75$ km/s to a ring limit for $v_\infty = 7.78$ km/s. Call this the source ring limit, R_{source}.

- Using Table A4, find the value of the exponent on the small body mass, β, for $v_\infty = 7.75$ km/s. Use interpolation to find β for $v_\infty = 7.78$ km/s.

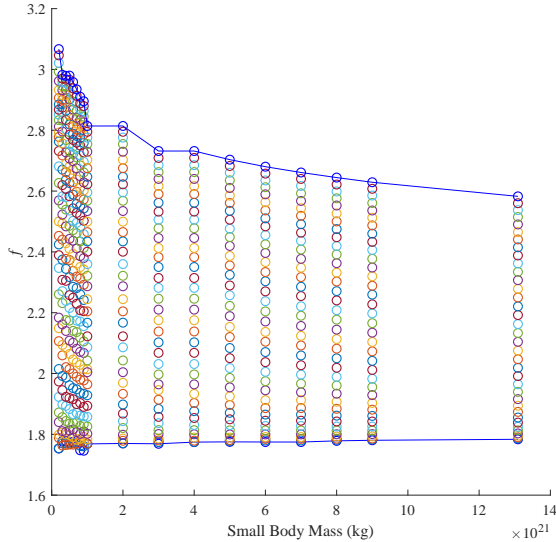**Figure 14.** f versus small body mass for eighteen 2D slices of constant small body mass for close encounters with Jupiter. $r = 50{,}000$ km. Contours of constant v_∞ are color coded. Along a contour, f generally decreases with m_s. Two contours are shown in blue as a set of data points on a smooth curve. The top contour is a curve of constant $v_\infty = 9$ km/s, and the bottom is a curve of constant $v_\infty = 0$ km/s (parabolic orbits). The value of f along the bottom contour remains remarkably constant at a value around 1.8. The vertically aligned set of data points on the far right is for Pluto.

- Use a proportion to find the ring limit for $m_s = 7.986 \times 10^{18}$ kg. $R_{target} = R_{source}\left(\frac{m_{target}}{m_{source}}\right)^\beta$

For close encounters with Saturn, Uranus or Neptune, Table A5, A6 or A7 can be used respectively instead of Table A2. We tested the β values to make sure that they were applicable to close encounters between small bodies and any giant planet - not just Jupiter.

We accomplished this by calculating ring limits for close encounters between the other three giant planets and selected small bodies of various masses and v_∞ using two different techniques. The first technique made use of the relation $R \sim M_p^\gamma$. The exponent γ was found using Table A1 for the v_∞ in question. A proportion was then used to convert ring limits for close encounters with Jupiter to ring limits for close encounters with each giant planet.

$$R_{planet} = R_{Jupiter}\left(\frac{M_p}{M_{Jupiter}}\right)^\gamma \qquad (19)$$

where R_{planet} is the ring limit for a close encoucnter between the planet and the small body in question, $R_{Jupiter}$ is the ring limit for a close encounter between Jupiter and the small body in question, M_p the mass of the other planet, and $M_{Jupiter}$ the mass of Jupiter.

The second technique made use of the relation $R \sim m_s^\beta$. Using the second technique, the ring limit was found from Table A5, A6 or A7 depending on the planet for the v_∞ in question. β was determined for the v_∞ in question using Table A4. A proportion was then used to convert ring limits for close encounters between the planet and Pluto to ring limits for close encounters between the planet and the small body in question.

$$R_{planet} = R_{Pluto}\left(\frac{m_s}{m_{Pluto}}\right)^\beta \qquad (20)$$

where R_{Pluto} is the ring limit for a close encounter between Pluto and the planet and m_{Pluto} is the mass of Pluto. We found good enough agreement between corresponding values found using the two techniques to warrant the use of β values to find approximate ring limits for close encounters for each of the giant planets.

To test the accuracy of our results, we used extrapolation to find ring limit values for close encounters between Jupiter and a Chariklo with a mass of 7.986×10^{18} kg and ring orbital radius of 50,000 km over the range $0 \le v_\infty \le 9$ km/s.

We compared our extrapolated ring limit values to d_{min} values reported by Araujo et al. (2016) for noticeable close encounters between giant planets and Chariklo. Araujo et al. (2016) used a mass of 7.986×10^{18} kg for Chariklo, and a ring orbital radius of 410 km. Each reported d_{min} value had a different velocity at infinity. Their system was non-planar and included the Sun, the four giant planets of the Solar system, Chariklo and 100 massless test particles for the outer ring (effectively the seven-body problem).

As their simulation was non-planar, the rings of Chariklo were not restricted to the plane of the hyperbolic or parabolic orbit about the planet as they were in our study. Since planar rings are more easily perturbed than non-planar rings, then for any noticeable close encounter with a given v_∞, the ring limit will be greater than or equal to the d_{min} value of the encounter.

This reflects the fact that given all other quantities constant, a small body with inclined rings must get closer to the planet than a small body with planar rings in order for the close encounter to have a noticeable effect because when the rings are inclined, only the planar component of the gravitational force perturbs the ec-

centicity of the ring particle orbits (Murray & Dermott 1999).

Given that f decreases with decreasing r if all other variables are constant, the ring limit for a Chariklo with a ring orbital radius of 410 km for any particular v_∞ value will have a smaller f than the corresponding extrapolated value at the same v_∞ found for $r = 50{,}000$ km. Thus, in this case, our extrapolated values form a ring limit upper bound curve in $d_{min} - v_\infty$ space rather than a curve of actual ring limits for a Chariklo with a ring orbital radius of 410 km. Even though 50,000 km and 410 km differ by an order of magnitude, the method was reasonable because as Figure 11 shows, f maintains the same order of magnitude even over order of magnitude variations in r and in fact becomes independent of r as v_∞ approaches zero.

The results for Jupiter are shown in Figure 15. The set of our extrapolated data points shown in gray forms a ring limit upper bound curve. d_{min} values reported by Araujo et al. (2016) are shown in red. To cover the full velocity range of these d_{min} values, we extrapolated our upper bound curve to extend the range to $v_\infty = 11$ km/s.

Nineteen out of twenty d_{min} values lie within the ring limit upper bound curve. The one exception lies at ($v_\infty = 1.25$ km/s, $d_{min} = 2.81$ R_{td}). At this time we cannot explain this discrepancy. Another peculiar value lies at ($v_\infty = 3.17$ km/s, $d_{min} = 2.61$ R_{td}). Though seemingly on our curve, it is actually 0.02 R_{td} below it. Over all planets, we find that 26 out of 27 d_{min} values reported by Araujo et al. (2016) lie within their respective ring limit upper bound curve.

We present three different ways to use the ring limit upper bound curve in $d_{min} - v_\infty$ space:

- Include velocity effects and set the ring limit equal to the curve so that the ring limit varies with v_∞ as has just been shown. This curve would be different for each planet.

- Ignore velocity effects and set the ring limit equal to the maximum value of the curve over the v_∞ range in question. This maximum value would vary with the planet mass.

- Ignore velocity effects and set the ring limit equal to a constant lower bound value of 1.8 tidal disruption distances for each planet

Each method has its own advantages and disadvantages. Including velocity effects is the most accurate method but is more complicated as each value of velocity at infinity has its own unique ring limit upper bound. This makes computations of close encounter severity more intensive and may require interpolation or extrapolation.

Setting the ring limit equal to a maximum curve value for each planet is simpler but may cause some close encounters to be classified as moderate when actually they are not noticeable. As an example of using this method, consider Figure 15. The figure shows that over the range $0 \leq v_\infty \leq 9$ km/s the ring limit upper bound curve reaches a maximum value of about 3.5 R_{td}. Therefore, using this method, the ring limit would be set to a constant maximum value of $R = 3.5$ R_{td} (or $f_{max} = 3.5$) for close encounters with Jupiter. This technique would have to be repeated to obtain the maximum values for the other giant planets.

Using the second method would ensure that all close encounters subject to the condition $d_{min} > R$ are not noticeable. However, notice in the figure that as v_∞ approaches zero there is a region that lies below 3.5 R_{td} but above the ring limit upper bound curve. Using this method, close encounters with d_{min} values in this region would be mistakenly classified as moderate.

Also shown in Figure 15 are Δe_{max} values for selected close encounters. It can be seen that using our scale, even a close encounter of moderate severity can cause the change in eccentricity of a ring particle to exceed 0.5. With no correction, it would then possibly only take two moderate close encounters to remove a ring particle from its orbit entirely. Though this may not result in the entire loss of a ring, the cumulative effect of multiple moderate encounters may not be negligible and may result in the loss of ring particles.

Using extrapolation, we also found f_{max} for close encounters between Chariklo and the other giant planets. The results were $f_{max} = 3.9$ for Saturn, $f_{max} = 4.4$ for Uranus and $f_{max} = 4.4$ for Neptune.

To test these values, we compared them to d_{min} values for noticeable close encounters between Chariklo and Saturn or Uranus reported by Araujo et al. (2016). All of these d_{min} values fell within their respective f_{max} value as can be seen in Table A8. f_{max} values for close encounters between each giant planet and a Chiron or Haumea with $r = 50{,}000$ km were also found and are shown along with Chariklo's values in Table A9.

Using the third method would ensure that all close encounters subject to the condition $d_{min} < R$ would be noticeable. The drawback with this method is that some noticeable close encounters with d_{min} above 1.8 R_{td} but below the ring limit upper bound curve would be mistakenly counted as being not noticeable.

Using the third method, the ring limit was set to a constant 1.8 tidal disruption distances. We compared
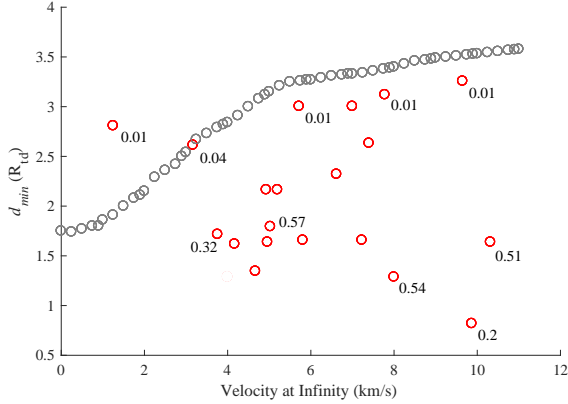
Figure 15. The d_{min} values reported by Araujo et al. (2016) and ring limit upper bound curve vs velocity at infinity for close encounters between Chariklo and Jupiter. Our extrapolated ring limit upper bound values are shown in gray for a Chariklo with a ring orbital radius of 50,000 km. The d_{min} values are shown in red for a Chariklo with a ring orbital radius of 410 km. All of the close encounters are noticeable ($\Delta e_{max} \geq 0.01$) with Δe_{max} ranging from 0.01 to 0.57. Δe_{max} values are shown for selected data points. Only one d_{min} value ($v_\infty = 1.25$ km/s, $d_{min} = 2.81$ R_{td}) lies beyond its ring limit upper bound. At this time we cannot explain this discrepancy.

this ring limit lower bound to the 27 d_{min} values reported by Araujo et al. (2016).

Figure 16 shows those d_{min} values within 1.8 R_{td}. d_{min} values for Jupiter are in red, and the one value for Saturn in yellow. Only one close encounter was severe, and there were no extreme encounters. Only 11 d_{min} values lied within 1.8 R_{td}. This means that out of the reported 27 noticeable close encounters, only 11 would be counted as noticeable using this method.

Our improved determination of the ring limit using any method showed that the ring limit was far below our initial estimate of 10 tidal disruption distances for every planet. This makes moderate close encounters less likely than the frequencies found using our previous close encounter severity scale on integrations of Chariklo and Chiron. Regardless of which method is used, the result is a more accurate measure of the value of the ring limit.

6. CONCLUSIONS

The field of ringed small bodies in the Solar system is only a few years old and started with the unexpected discovery of two narrow rings around the Centaur Chariklo. Since then, the field has been slowly growing with the discovery of rings around the dwarf planet Haumea and the potential of rings around the Centaur Chiron.

Close encounters with planets are an important part of the history of ringed small bodies as they have conse-
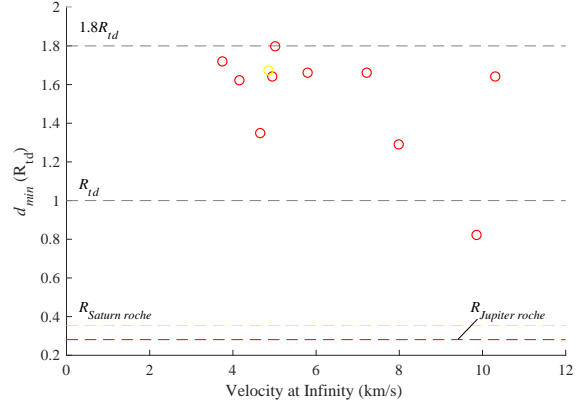
Figure 16. The d_{min} values reported by Araujo et al. (2016) within 1.8 tidal disruption distances for close encounters between Chariklo and Jupiter or Saturn. d_{min} values for close encounters with Jupiter are shown in red and those with Saturn are shown in yellow. All of the close encounters are noticeable ($\Delta e_{max} \geq 0.01$) with Δe_{max} ranging from 0.2 to 0.57. The dashed lines from top to bottom are 1.8 R_{td}, R_{td}, the Roche limit of Saturn, and the Roche limit of Jupiter. Out of 27 noticeable close encounters reported by Araujo et al. (2016), only 11 of these would be counted as noticeable if the ring limit is set to 1.8 tidal disruption distances.

quences for ring origin theories and ring longevity. The severity of such an encounter depends on the mass of the small body, the mass of the planet, the inclination of the rings, the relative velocity of the small body at infinity, the initial ring orbital radius and the minimum separation distance, d_{min} (or encounter distance).

In our previous works, we studied close encounters of Charklo and Chiron with the giant planets using numerical integration. The severity of each close encounter was found using a close encounter severity scale which we developed. In this scale, d_{min} is compared to the critical distances Hill radius, tidal disruption distance, Roche Limit and "ring limit", R.

The ring limit separates "non-noticeable" encounters from "noticeable" encounters. Encounters for which d_{min} is larger than the tidal disruption distance but less than the ring limit are classified as moderate encounters. Though one moderate encounter may not be strong enough to completely remove a ring, the effect of multiple moderate close encounters may result in the loss of ring particles.

We define the ring limit as the d_{min} value associated with a close encounter for which the effect on the ring is just "noticeable" for a small body in a parabolic or hyperbolic orbit about the planet in the three-body planar problem. The effect is just noticeable if the maximum change in eccentricity of the orbit of any ring particle is 0.01.

Unlike the other critical distances, the ring limit is a relatively new parameter which currently has no simple analytical expression. In our previous close encounter severity scale, the ring limit was set to a constant value of 10 tidal disruption distances for any giant planet. However, this estimate is crude and ignores the effects of the velocity at infinity. In this work, we seek to improve our close encounter severity scale by refining our expression for the ring limit so that the effects of small body mass, m_s, planet mass, M_p, velocity at infinity, v_∞, and ring orbital radius, r, are fully accounted for.

Using the technique of numerical integration, close encounters between hypothetical one-ringed bodies with each of the four giant planets are simulated using varying values of small body mass, ring orbital radius and velocity at infinity.

We investigate the relationship between the ring limit and each of the variables m_s, r, v_∞ and the planet mass by plotting our data in three dimensional $R - r - v_\infty$ and $R - m_s - v_\infty$ space and examining 2D slices of each with a third quantity held constant in the slice.

Regression is used on a slice to determine the relationship between the ring limit and a single quantity. To find the planet mass dependence, an intersection of two slices - one of constant r and one of constant v_∞ is used. We find that the ring limit varies as a power law with M_p, m_s and r in the forms $R \sim M_p^\gamma$, $R \sim m_s^\beta$ and $R \sim r^\alpha$ with the exponents α, β and γ each being a function of v_∞ and other variables. The variation of R with v_∞ did not fit any one mathematical form. The ring limit increases with increasing r and M_p but decreases with increasing m_s.

For each planet, we show that the ring limit has a lower bound of approximately 1.8 tidal disruption distances (or $f_{min} = 1.8$) regardless of the mass of the small body or ring orbital radius. We find that f_{min} decreases with increasing planet mass, but we consider this dependence to be small.

This means that if the encounter distance between a one-ringed small body and a planet is within $\approx$1.8 tidal disruption distances then the close encounter always has a noticeable effect on the ring.

We introduce this lower bound distance as a new critical distance for close encounters between ringed small bodies and giant planets. The ring limit equals this critical distance when the small body is in a parabolic orbit about the planet (and thus $v_\infty = 0$ by definition).

Using this critical distance, an analytical solution of the ring limit for parabolic orbits is found and is approximately

$$R \simeq 1.8r\left(\frac{3M_p}{m_s}\right)^{\frac{1}{3}} \qquad (21)$$

We are unable to find a general analytical solution for R that fits all hyperbolic orbits. However, we show that analytical solutions for R can be found for specific cases.

We test our results by extrapolating our ring limit values to those for close encounters between the giant planets and a Chariklo with a ring orbital radius of $r = 50{,}000$ km and compare them to d_{min} values reported by Araujo et al. (2016) for Chariklo-planet encounters in the seven-body non-planar problem (Sun, Chariklo, four giant planets, ring particle).

We successfully show that our ring limit values can be extrapolated to find a ring limit upper bound curve in $d_{min} - v_\infty$ space for close encounters between a giant planet and Chariklo. We suggest three different uses for this curve: 1) use it as is and set the ring limit equal to the curve 2) set the ring limit equal to the maximum value of the curve over the v_∞ range in question ($R = f_{max}$) and 3) set the ring limit equal to a constant lower bound value of 1.8 tidal disruption distances ($R = f_{min}$).

The advantage of the first method is its accuracy in determining the ring limit which varies with v_∞. The drawback is that it is more complicated to use and may involve interpolation or extrapolation. Using the first method, we find that 26 out of 27 d_{min} values for noticeable encounters reported by Araujo et al. (2016) lie within their respective ring limit upper bound curve. We are unable to explain the one discrepancy.

The second method is simpler than the first method as the ring limit is set to a value which does not vary with v_∞ but does vary with the planet. The drawback is that some close encounters of low severity lying beyond the ring limit upper bound curve but within f_{max} would be mistakenly classified as moderate encounters.

Using the second method, we use extrapolation to find f_{max} values for close encounters between each giant planet and Chariklo, Chiron and Haumea. For Chariklo, the results are $f_{max} = 3.5$ for Jupiter, $f_{max} = 3.9$ for Saturn, $f_{max} = 4.4$ for Uranus and $f_{max} = 4.4$ for Neptune. These values are much more accurate than the constant distance of 10 tidal disruption distances used for R in our previous studies. When using this method, all 27 d_{min} values for noticeable encounters reported by Araujo et al. (2016) lie within their respective ring limit.

Using the third method, we set the ring limit equal to a constant lower bound of 1.8 R_{td}. The advantage of this method is that any close encounter occuring within the ring limit would be noticeable. The drawback of this

method is that some moderate close encounters occuring beyond 1.8 R_{td} but within the ring limit upper bound curve would be mistakenly classified as non-noticeable encounters. As an example, we find that out of the 27 noticeable close encounters reported by Araujo et al. (2016), only 11 of these would be counted as noticeable with this method.

In the future, it would be ideal to run further simulations to extend the phase covered by our "standard" simulations, so that any extrapolations can begin closer to the desired outcome. Such work may also help to resolve the uncertainties in the form of the relationship between the ring limit and the various variables that can influence the final answer.

In particular, it would be interesting to examine more scenarios for which v_∞ was greater than the 9 km/s value used in this work, to see whether the ring limit curves for Jupiter and Saturn exhibit the same behaviour as for Uranus and Neptune.

As of this writing, it is not known if rings around small bodies are ubiquitous or rare. That may change in the near future with the release of the catalogue of stellar positions obtained by Gaia. Then, the location of the stars in the sky will become much more precisely known, which will in turn reduce the uncertainty in the path that stellar occultation event shadows will take over Earth. That will allow more observations to be made, and since all small body rings thus far have been discovered by stellar occultation, more rings may be found. We hope that this work has laid a foundation which will be built upon and applied to other ringed bodies currently awaiting discovery.

REFERENCES

Agnor, Craig B., & Hamilton, Douglas P. 2006, Nature, 441, 192

Altenhoff, W. J., Menten, K. M., & Bertoldi, F. 2001, A&A, 366, L9

Araujo, R. A. N., Sfair, R., & Winter, O. C. 2016, ApJ, 824, article id. 80

Araujo, R. A. N., Winter, O. C., Prado, A. F. B. A., & Vieira Martins, R. 2008, MNRAS, 391, 675

Bailey, B. L., & Malhotra, R. 2009, Icarus, 203, 155

Bate, R. R., Mueller, D. D., & White, J. E. 1971, Fundamentals of astrodynamics., by Bate, R. R.; Mueller, D. D.; White, J. E.. New York, NY (USA): Dover Publications, 12 + 455 p.,

Benson, A. J., Cannella, C., & Cole, S. 2016, Computational Astrophysics and Cosmology, 3, 3

Braga-Ribas, F., et al. 2014, Nature, 508(7494), 72

Brasser, R., Schwamb, M. E., Lykawka, P. S., & Gomes, R. S. 2012, MNRAS, 420, 3396

Brown, M. E., Barkume, K. M., Ragozzine, D., & Schaller, E. L. 2007, Nature, 446, 294

Brown, M. E., & Koresko, C. C. 1998, ApJ, 505, 65

Campins, H., & Fernández, Y. 2000, Earth, Moon & Planets, 89(1), 117134

Di Sisto, R. P., & Brunini, A. 2007, Icarus, 190, 224

El Moutamid, Maryame, Kral, Quentin, Sicardy, Bruno, Charnoz, Sebastien, Roques, Françoise, Nicholson, Philip D., & Burns, Joseph A. 2014, American Astronomical Society, DDA meeting #45, #402.05

Emel'yanenko, V. V., Asher, D. J., & Bailey, M. E. 2005, MNRAS, 361, 1345

Fouchard, M., Rickman, H., Froeschlé, Ch., & Valsecchi, G. B. 2014, Icarus, 231, 99

Groussin, O., Lamy, P., & Jorda, L. 2004, A&A, 413, 1163

Horner, J., & Lykawka, P. S. 2010a, MNRAS, 405, 49

Horner, J., & Lykawka, P. S. 2010b, MNRAS, 402, 13

Horner, J., & Evans, N. Wyn 2006, MNRAS: Letters, 367, L20

Horner, J., Evans, N. W., & Bailey, M. E. 2004a, MNRAS, 355, 798

Horner, J., Evans, N. W., & Bailey, M. E. 2004b, MNRAS, 354, 798

Horner, J., & Jones, B. W. 2010, Astronomy and Geophysics, 51, 6.16

Horner, J., Lykawka, P. S., Bannister, M. T., & Francis, P. 2012a, MNRAS, 422, 2145

Horner, J., Müller, T. G., & Lykawka, P. S. 2012b, MNRAS, 423, 2587

Horner, J., & Wittenmyer, R. 2018, American Astronomical Society Meeting Abstracts, 231, #128.04

Hyodo, Ryuki, Charnoz, Sébastien, Genda, Hidenori, & Ohtsuki, Keiji 2016, ApJL, 828, L8

Jeans, J. H. 1928, Cambridge [Eng.] The University press, 1928.,

Jeffreys, H. 1947, MNRAS, 107, 260

Jewitt, D., & Kalas, P. 1998, ApJ, 499, L103

Kowal, C.T., Liller, W., & Marsden, B.G. 1979, IAU Symp. 81: Dynamics of the Solar System, 81, 245

Lacerda, P., & Jewitt, D. C. 2007, AJ, 133, 1393

Levison, H. F., & Duncan, M. J. 1997, Icarus, 127, 13

Lykawka, P. S., Horner, J., Mukai, T., & Nakamura, A. M. 2012, MNRAS, 421, 1331

Meech, K. J., & Svoren, J. 2004, Comets II, 317

Murray, C.D., & Dermott, S. F. 1999, Solar System Dynamics (Cambridge University Press)

Ortiz, J. L., Duffard, R., Pinilla-Alonso, N., Alvarez-Candal, A., Santos-Sanz, P., Morales, N., Fernández-Valenzuela, E., Licandro, J., Campo Bagatin, A., & Thirouin, A. 2015, A&A, 576, id.A18

Ortiz, J. L., Santos-Sanz, P., Sicardy, B., et al. 2017, Nature, 550, 219

Pan, Margaret, & Wu, Yanqin 2016, AJ, 821, article id. 18

Philpott, C. M., Hamilton, D. P., & Agnor, C. B. 2010, Icarus, 208, 824

Rabinowitz, D. L., Barkume, K., Brown, M. E., et al. 2006, ApJ, 639, 1238

Ragozzine, D., & Brown, M. E. 2009, AJ, 137, 4766

Rawal, J. J., & Nikouravan, B. 2011, International Journal of Fundamental Physical Sciences (IJFPS), Vol. 1, No. 1, p. 6-10, 1, 6

Rein, H., & Liu, S.-F. 2012, A&A, 537, A128

Rein, H., & Spiegel, D. S. 2015, MNRAS, 446, 1424

Scotti, J. V., & Williams, G. V. 1997, Minor Planet Electronic Circulars, 1997-Y24,

Sheppard, S., Jewitt, D., Trujillo, C., Brown, M., & Ashley, M. 2000, AJ, 120, 2687

Sicardy, B., El Moutamid, M., Quillen, A. C., et al. 2016, arXiv:1612.03321

Sykes, M. V., & Walker, R. G. 1991, Science, 251, 777

Tiscareno, M., & Malhotra, R. 2003, AJ, 126(6), 3122

Volk, Kathryn, & Malhotra, Renu 2008, ApJ, 687, 714

Wang, L., Spurzem, R., Aarseth, S., et al. 2015, MNRAS, 450, 4070

Wood, J., Horner, J., Hinse, T. C., & Marsden, S. C. 2017, AJ, 153, 245

Wood, J., Horner, J., Hinse, T. C., & Marsden, S. C. 2018, AJ, 155, 2

APPENDIX

Table A1. The ring limit varies with the planet mass as a power law of the form $R \sim M_p^\gamma$. This table gives values of γ as a function of velocity at infinity for close encounters between any giant planet and a small body with a mass equal to the mass of Pluto with a ring orbital radius of 50,000 km. Each value of γ was found from a regression on four data points in $R - M_p$ space while holding the velocity at infinity constant.

v_∞ (km/s)	γ	v_∞ (km/s)	γ
9	0.2699	4.5	0.2347
8.9	0.2689	4.25	0.2346
8.75	0.2674	4	0.2349
8.5	0.265	3.9	0.2352
8.25	0.2627	3.75	0.2357
8	0.2602	3.5	0.2374
7.9	0.2592	3.25	0.2395
7.75	0.2577	3	0.2427
7.5	0.2554	2.9	0.2442
7.25	0.2531	2.75	0.2469
7	0.2508	2.5	0.2521
6.9	0.2499	2.25	0.2584
6.75	0.2486	2	0.2658
6.5	0.2464	1.9	0.269
6.25	0.2443	1.75	0.2741
6	0.2423	1.5	0.2834
5.9	0.2416	1.25	0.293
5.75	0.2405	1	0.302
5.5	0.2389	0.9	0.3054
5.25	0.2375	0.75	0.3099
5	0.2361	0.5	0.3159
4.9	0.2358	0.25	0.3194
4.75	0.2353	0	0.323

WOOD ET AL.

Table A2. Ring limit values for close encounters between Jupiter and a small body with a ring orbital radius of 50,000 km and mass equal to the mass of Pluto.

v_∞ (km/s)	R (km)	f	v_∞ (km/s)	R (km)	f
9	9784298	2.5826	4.5	7972237	2.1043
8.9	9750201	2.5736	4.25	7862748	2.0754
8.75	9698677	2.5600	4	7754395	2.0468
8.5	9613056	2.5374	3.9	7709690	2.0350
8.25	9527056	2.5147	3.75	7648316	2.0188
8	9434615	2.4903	3.5	7544889	1.9915
7.9	9397109	2.4804	3.25	7442977	1.9646
7.75	9338765	2.4650	3	7347884	1.9395
7.5	9247461	2.4409	2.9	7311135	1.9298
7.25	9149338	2.4150	2.75	7258096	1.9158
7	9047805	2.3882	2.5	7175505	1.8940
6.9	9009162	2.3780	2.25	7098598	1.8737
6.75	8948545	2.3620	2	7028510	1.8552
6.5	8843223	2.3342	1.9	7003505	1.8486
6.25	8740175	2.3070	1.75	6965241	1.8385
6	8631444	2.2783	1.5	6913338	1.8248
5.9	8587118	2.2666	1.25	6868633	1.8130
5.75	8524607	2.2501	1	6830748	1.8030
5.5	8413223	2.2207	0.9	6819003	1.7999
5.25	8305250	2.1922	0.75	6802334	1.7955
5	8192351	2.1624	0.5	6782254	1.7902
4.9	8149541	2.1511	0.25	6769752	1.7869
4.75	8080968	2.1330	0	6757250	1.7836

Table A3. The ring limit varies with the ring orbital radius as a power law of the form $R \sim r^{\alpha}$. This table gives values of α as a function of velocity at infinity for close encounters between Jupiter and a small body with a mass equal to the mass of Pluto. Each value of α was found from a regression on twenty data points in $R - r$ space over a ring orbital radius range of 30,000 km - 100,000 km while holding the velocity at infinity constant.

v_{∞} (km/s)	α	v_{∞} (km/s)	α
9	1.1461	4.5	1.1298
8.9	1.1468	4.25	1.1241
8.75	1.1476	4	1.1176
8.5	1.1491	3.9	1.115
8.25	1.1507	3.75	1.1101
8	1.152	3.5	1.1023
7.9	1.1524	3.25	1.093
7.75	1.1528	3	1.0839
7.5	1.1536	2.9	1.0797
7.25	1.1538	2.75	1.0741
7	1.1537	2.5	1.0636
6.9	1.1537	2.25	1.0527
6.75	1.1535	2	1.042
6.5	1.1527	1.9	1.0397
6.25	1.1522	1.75	1.0325
6	1.1508	1.5	1.0238
5.9	1.1501	1.25	1.017
5.75	1.1488	1	1.0111
5.5	1.1462	0.9	1.008
5.25	1.1428	0.75	1.0057
5	1.1395	0.5	1.0025
4.9	1.138	0.25	1.0007
4.75	1.1353	0	1.0000

Table A4. The ring limit varies with the small body mass as a power law of the form $R \sim m_s^\beta$. This table gives values of β as a function of velocity at infinity for close encounters between Jupiter and a small body with a ring orbital radius of 50,000 km. Each value of β was found using regression on eighteen data points in $R - m_s$ space over a mass range of 2×10^{20} kg to the mass of Pluto (1.309×10^{22} kg) while holding the velocity at infinity constant.

v_∞ (km/s)	β	v_∞ (km/s)	β
9	-0.3734	4.5	-0.3815
8.9	-0.3738	4.25	-0.3801
8.75	-0.3743	4	-0.3785
8.5	-0.3752	3.9	-0.3782
8.25	-0.3759	3.75	-0.3772
8	-0.3767	3.5	-0.3754
7.9	-0.377	3.25	-0.3736
7.75	-0.3774	3	-0.3698
7.5	-0.3781	2.9	-0.3684
7.25	-0.379	2.75	-0.3657
7	-0.38	2.5	-0.3627
6.9	-0.3804	2.25	-0.3594
6.75	-0.381	2	-0.3535
6.5	-0.3818	1.9	-0.3515
6.25	-0.3822	1.75	-0.3492
6	-0.3826	1.5	-0.3449
5.9	-0.3829	1.25	-0.3399
5.75	-0.3833	1	-0.3363
5.5	-0.3839	0.9	-0.3338
5.25	-0.3838	0.75	-0.334
5	-0.3832	0.5	-0.3307
4.9	-0.383	0.25	-0.3303
4.75	-0.3826	0	-0.3333

Table A5. Ring limit values for close encounters between Saturn and a small body with a ring orbital radius of 50,000 km and mass equal to the mass of Pluto.

v_∞ (km/s)	R (km)	f	v_∞ (km/s)	R (km)	f
9	7397991.29	2.9189	4.5	6094491.026	2.4046
8.9	7379235.891	2.9115	4.25	5991843.232	2.3641
8.75	7351609.694	2.9006	4	5881084.994	2.3204
8.5	7305228.098	2.8823	3.9	5838758.62	2.3037
8.25	7254791.28	2.8624	3.75	5770073.305	2.2766
8	7201059.595	2.8412	3.5	5658808.165	2.2327
7.9	7177742.072	2.832	3.25	5544248.157	2.1875
7.75	7142258.884	2.818	3	5429181.247	2.1421
7.5	7080163.304	2.7935	2.9	5381278.943	2.1232
7.25	7018828.079	2.7693	2.75	5314874.691	2.097
7	6954704.889	2.744	2.5	5200821.586	2.052
6.9	6927332.144	2.7332	2.25	5094625.473	2.0101
6.75	6884498.866	2.7163	2	4990710.421	1.9691
6.5	6809223.817	2.6866	1.9	4950918.56	1.9534
6.25	6733695.316	2.6568	1.75	4896933.424	1.9321
6	6655885.754	2.6261	1.5	4811520.321	1.8984
5.9	6622176.725	2.6128	1.25	4739540.139	1.87
5.75	6569458.845	2.592	1	4678711.817	1.846
5.5	6482271.583	2.5576	0.9	4659956.417	1.8386
5.25	6393056.71	2.5224	0.75	4632330.221	1.8277
5	6295224.491	2.4838	0.5	4600141.9	1.815
4.9	6256953.338	2.4687	0.25	4580626.146	1.8073
4.75	6199419.883	2.446	0	4561110.393	1.7996

Table A6. Ring limit values for close encounters between Uranus and a small body with a ring orbital radius of 50,000 km and mass equal to the mass of Pluto.

v_∞ (km/s)	R (km)	f	v_∞ (km/s)	R (km)	f
9	4287793.84	3.1648	4.5	3873619.618	2.8591
8.9	4285761.582	3.1633	4.25	3820916.389	2.8202
8.75	4282239.001	3.1607	4	3760355.094	2.7755
8.5	4276548.678	3.1565	3.9	3735697.028	2.7573
8.25	4268419.645	3.1505	3.75	3697490.574	2.7291
8	4259477.709	3.1439	3.5	3626090.569	2.6764
7.9	4255819.644	3.1412	3.25	3551845.403	2.6216
7.75	4249180.934	3.1363	3	3469471.204	2.5608
7.5	4235226.094	3.126	2.9	3435600.234	2.5358
7.25	4219780.932	3.1146	2.75	3381000.23	2.4955
7	4201897.06	3.1014	2.5	3287516.353	2.4265
6.9	4194038.995	3.0956	2.25	3189290.539	2.354
6.75	4181980.929	3.0867	2	3086187.307	2.2779
6.5	4160709.96	3.071	1.9	3044458.271	2.2471
6.25	4137406.733	3.0538	1.75	2981051.816	2.2003
6	4110309.957	3.0338	1.5	2875780.841	2.1226
5.9	4097980.924	3.0247	1.25	2775658.253	2.0487
5.75	4079284.148	3.0109	1	2685290.505	1.982
5.5	4044735.759	2.9854	0.9	2653316.309	1.9584
5.25	4008561.563	2.9587	0.75	2610367.919	1.9267
5	3969000.27	2.9295	0.5	2556038.883	1.8866
4.9	3950980.914	2.9162	0.25	2524471.139	1.8633
4.75	3922800.267	2.8954	0	2492903.395	1.84

Table A7. Ring limit values for close encounters between Neptune and a small body with a ring orbital radius of 50,000 km and mass equal to the mass of Pluto.

v_∞ (km/s)	R (km)	f	v_∞ (km/s)	R (km)	f
9	4518021.816	3.156	4.5	4035727.282	2.8191
8.9	4515015.527	3.1539	4.25	3976603.612	2.7778
8.75	4510148.203	3.1505	4	3913185.245	2.7335
8.5	4500986.182	3.1441	3.9	3885842.337	2.7144
8.25	4490106.282	3.1365	3.75	3844183.771	2.6853
8	4477079.032	3.1274	3.5	3769456.034	2.6331
7.9	4471352.769	3.1234	3.25	3689002.033	2.5769
7.75	4462190.748	3.117	3	3602964.926	2.5168
7.5	4446014.053	3.1057	2.9	3566603.153	2.4914
7.25	4427690.011	3.0929	2.75	3510915.242	2.4525
7	4407075.462	3.0785	2.5	3414141.39	2.3849
6.9	4398056.598	3.0722	2.25	3312643.372	2.314
6.75	4383597.783	3.0621	2	3207566.439	2.2406
6.5	4357972.754	3.0442	1.9	3165048.933	2.2109
6.25	4330057.22	3.0247	1.75	3101487.409	2.1665
6	4298419.615	3.0026	1.5	2997126.259	2.0936
5.9	4284962.896	2.9932	1.25	2898348.215	2.0246
5.75	4263775.721	2.9784	1	2811022.699	1.9636
5.5	4226411.852	2.9523	0.9	2780387.19	1.9422
5.25	4184466.973	2.923	0.75	2740017.033	1.914
5	4139372.649	2.8915	0.5	2688766.975	1.8782
4.9	4120189.667	2.8781	0.25	2657988.31	1.8567
4.75	4089554.157	2.8567	0	2627209.644	1.8352

Table A8. The d_{min} values reported by Araujo et al. (2016) for close encounters between Chariklo and the planets Jupiter, Saturn and Uranus. All of the close encounters are noticeable ($\Delta e_{max} \geq 0.01$) with Δe_{max} ranging from 0.01 to 0.57.

Planet	d_{min} (R$_{td}$)	v_∞ (km/s)	Δe_{max}
Jupiter			
	0.82	9.87	0.2
	1.29	8	0.54
	1.35	4.67	0.28
	1.62	4.17	0.4
	1.64	4.96	0.33
	1.64	10.32	0.51
	1.66	5.81	0.45
	1.66	7.23	0.2
	1.72	3.76	0.32
	1.79	5.03	0.57
	2.16	4.93	0.03
	2.16	5.2	0.19
	2.32	6.62	0.1
	2.61	3.17	0.04
	2.63	7.4	0.02
	2.81	1.25	0.01
	3	7	0.02
	3	5.72	0.01
	3.12	7.78	0.01
	3.26	9.65	0.01
Saturn			
	1.67	4.87	0.34
	1.82	3.12	0.53
	1.94	2.68	0.3
	2.02	4.42	0.07
	2.29	5.29	0.06
	2.56	3.63	0.031
Uranus			
	2.11	3.00	0.11

Table A9. Ring limit upper bound maximum values over the range $0 \leq v_\infty \leq 9$ km/s for each giant planet for close encounters between each planet and Chiron, Chariklo, or Haumea. The masses used for Chiron, Chariklo, or Haumea were 3.05×10^{18} kg, 7.986×10^{18} kg, and 4.006×10^{21} kg respectively. Using this method, close encounters between one of these bodies and a giant planet could be studied by ignoring velocity effects and setting the ring limit equal to a constant maximum value. Then, close encounters with d_{min} values below this maximum value but larger than the tidal disruption distance would be considered moderate close encounters.

Body	Planet	f_{max}
Chiron		
	Jupiter	3.6
	Saturn	4.1
	Uranus	4.6
	Neptune	4.6
Chariklo		
	Jupiter	3.5
	Saturn	3.9
	Uranus	4.4
	Neptune	4.4
Haumea		
	Jupiter	2.7
	Saturn	3.1
	Uranus	3.3
	Neptune	3.3

5   Conclusions

The recent discovery of rings or ring-like structures around three small bodies of the Solar system has given birth to a new subfield of Solar system astronomy - the study of ringed small bodies. Two of these bodies are classified as Centaurs and move on dynamically unstable orbits. Studying their orbital evolution and, in particular, close encounter history can shed light on the survivability of their rings over the short and long term. Here, we present our conclusions on the results of our three previously done studies combined (chapters 2, 3 and 4) that investigate these newly discovered ring systems.

5.1   Chariklo and Chiron

Chariklo and Chiron represent the only two Centaurs known to have rings or ring-like structures. Though we can state that the orbital radii of any rings around either body have the same order of magnitude $\sim 10^2$ km we cannot say at this time if Chariklo and Chiron represent typical examples of ringed Centaurs in regards to the survivability of their rings or in regards to other properties (orbital radius, orbital eccentricity, etc.).

In this work, Chariklo and Chiron were studied using the technique of numerical integration to determine the chaoticity of their orbits and if their rings could predate their entrance into the Centaur region. To determine the latter, the likelihood that these bodies have had a close encounter with a giant planet severe enough to badly damage or even destroy any ring structure around the body must be determined.

Our results showed that both Chiron and Chariklo exist in highly chaotic orbits with the orbit of Chariklo showing a degree of stable chaos that the orbit of Chiron does not. Integrations of Chiron clones showed that Chiron is most likely a random-walk Centaur. This means that Chiron likely spends less time in mean motion resonances which can extend the dynamical lifetime of the object.

Chiron's orbit is indeed less stable than Chariklo's as exemplified by its lower half-life against backwards removal from the Centaur region of 0.7 Myr compared to Chariklo's 3 Myr. Our results showed that clones initially in planet crossing orbits had dynamical lifetimes as much as two orders of magnitude shorter than the longest lifetimes exhibited by the longest-lived clones.

Furthermore, the integrations showed that both bodies originated from somewhere beyond the orbit of Neptune where they would have been classified as Trans-Neptunian Objects or TNOs. Chiron likely entered the Centaur region within the last 8.5 Myr and Chariklo within the last 20 Myr.

To determine if rings around either of these bodies could have survived their journey through the Centaur region up to now, the close encounters of clones of these two objects with the four giant planets were examined to determine the probability of ring survival in the highly chaotic Centaur region.

To facilitate this, a scale to measure the relative severity of a close encounter between a ringed small body and a planet was developed and used in our first two papers without the ring particles themselves ever being simulated.

This scale was based entirely on the minimum distance obtained between the small body and planet (the close encounter distance) during the encounter. As such, it was not necessary to simulate the ring particles themselves as only the close encounter distance was needed.

In this scale, the close encounter distance is compared to the well known critical distances Hill radius, tidal disruption distance and Roche limit as well as a brand new parameter which we call the "ring limit".

We defined the ring limit as the value of the minimum approach distance for close encounters between a planet and a ringed small body in a hyperbolic or parabolic orbit about the planet in the three-body planar problem for which the effect on the ring is just noticeable.

The effect was considered noticeable if the close encounter changed the orbital eccentricity of the orbit of any ring particle by 0.01 or more. In the first version of our scale, we set the ring limit equal to a constant value of 10 tidal disruption distances based on previous work by Araujo et al. (2016). This simplistic approach ignored velocity effects.

By comparing the close encounter distance to the previously mentioned critical distances and ring limit, the severity of a close encounter was ranked as very low, low, moderate, severe or extreme. Close encounters of moderate or higher severity were noticeable.

Severe encounters were those which could destroy the rings. Extreme encounters were those which could result in the destruction of the rings and the small body itself due to tidal forces.

We showed that it is very unlikely that a single close encounter could have removed or have even severely damaged any ring system around either Chariklo or Chiron as 99% of close encounters experienced by clones of these two objects were of moderate or lower severity. Though it is interesting that this same result was found for both Chariklo and Chiron, we cannot state that this result will be the same for any ringed Centaurs found in the future as we only have a sample size of two. But if extreme encounters are the exception then the destruction of comet Shoemaker-Levy 9 by Jupiter in 1994 was a truly rare event for a body of that size (Jessup et al., 2000).

The paucity of severe and extreme encounters displayed by clones of these objects means that any ring system around either body could have formed while the body was a TNO before it entered the Centaur region provided that ring dispersal by other means did not occur. This idea is bolstered by the discovery of rings around the Trans-Neptunian Object Haumea.

5.2 Ring Origins

At this time, the population size of ringed small bodies is too small to make a prediction as to which of the proposed ring formation mechanisms is the dominant one. Each ringed body is unique, and it can only be said that we see inklings of possible formation mechanisms in each body.

For example, Chiron has displayed activity but neither Chariklo nor Haumea has ever known to be active. Haumea is a member of a collisional family while

Chariklo and Chiron are not. Chariklo and Chiron move on planet-crossing orbits while Haumea does not.

Thus, while we see small hints of possible ring formation by activity, collisions and tidal disruption, none of these hints provide conclusive proof of a dominant formation mechanism. One or multiple mechanisms may be involved in the creation of small body rings, and any ring formation scenario is certainly possible for any of these three bodies. It will take more discoveries to know for sure.

We can however conclude that ring creation by tidal disruption of Chiron or Chariklo seems unlikely given that our results showed that close encounters within the Roche limit were extremely rare.

5.3 Measuring Close Encounter Severity

The ring limit, R, was better defined in our third paper in which ring particles around hypothetical small bodies were actually simulated during close encounters with each of the four giant planets with the small body in a parabolic or hyperbolic orbit about the planet.

As in our first two papers, the ring limit was defined as that minimum separation distance, d_{min}, of a close encounter for which the effect on the ring was just noticeable when the small body was in a hyperbolic or parabolic orbit about the planet in the planar three-body problem. As in our first two papers, we sought to approximate an upper bound of the ring limit so that if $d_{min} < R$ then the encounter was considered noticeable and was considered non-noticeable otherwise.

We again defined the encounter as being just noticeable if the maximum change in eccentricity of the orbit of any ring particle equaled 0.01.

The simulations led to the determination of the ring limit over a range of ring orbital radii spanning an order of magnitude and a small body mass range spanning two orders of magnitude.

It was discovered that the ring limit was a complex function of ring orbital radius, small body mass, planet mass, velocity at infinity, v_∞, and ring inclination. Though we did not study rings inclined to the orbital plane, it had already been previously established that inclined rings are harder to perturb than planar rings (Murray & Dermott, 1999).

We found that the ring limit increased with ring orbital radius and planet mass as a power law ($R \sim r^\alpha$ and $R \sim M_p^\gamma$) and decreased with small body mass as a power law ($R \sim m_s^\beta$). The exponents α, β and γ were themselves a function of the velocity at infinity and other variables. The variation of the ring limit with velocity at infinity could not be fit to any one particular form.

We discovered that the ring limit had a lower bound of approximately 1.8 tidal disruption distances and that this lower bound was virtually independent of the ring orbital radius and small body mass. The mass of the planet had a small effect which was negligible to two significant figures. The ring limit equaled this lower bound when the small body was in a parabolic orbit (for which $v_\infty = 0$ by definition). We introduced the lower bound as a new critical distance. If a close encounter between a one-ringed small body and a planet

107

occurs within a distance of approximately 1.8 tidal disruption distances then the close encounter is always noticeable.

When our ring limit values were extrapolated for Chariklo-planet encounters, they formed a ring limit upper bound curve in $d_{min} - v_{\infty}$ space rather than a curve of actual ring limit values. This occurred because of our choice of ring orbital radius of 50,000 km which was an order of magnitude larger than the ring orbital radius of the outer ring of Chariklo.

This was by design so that our extrapolated values would apply to a very large range of ring orbital radii so that our results could be used to study close encounters of ringed small bodies that have yet to be discovered. This was reasonable as we found that the ring limit expressed in units of tidal disruption distances maintained the same order of magnitude even over order of magnitude changes in ring orbital radius. We presented three different ways to use the ring limit upper bound curve in $d_{min} - v_{\infty}$ space:

- include velocity effects and set the ring limit equal to the curve so that the ring limit varies with v_{∞}. This curve would be different for each planet.

- ignore velocity effects, use the curve to determine a maximum value for the ring limit upper bound over the velocity at infinity range in question and set the ring limit equal to this value. This maximum value would vary with the planet mass.

- ignore velocity effects and set the ring limit equal to a constant lower bound value of 1.8 tidal disruption distances for each planet

Each method has its own advantages and disadvantages. Including velocity effects is the most accurate method but is more complicated as each value of velocity at infinity has its own unique ring limit upper bound. This makes computations of close encounter severity more intensive and may require interpolation or extrapolation.

Setting the ring limit equal to a constant maximum value is simpler but may cause some close encounters to be classified as moderate when actually they are not noticeable. This can occur because when the ring limit is defined in this way, it is possible for a close encounter distance to be larger than its corresponding value of the ring limit upper bound curve (and therefore be non-noticeable) but be smaller than the maximum value of the curve.

If the ring limit is set equal to the lower bound value of 1.8 tidal disruption distances then this would avoid this error, however, this would introduce a new problem in that a close encounter distance could be larger than this lower bound but be smaller than its corresponding value of the ring limit upper bound curve (and thus be noticeable). This would mean that some noticeable close encounters would mistakenly be classified as non-noticeable.

To test each of the three methods, we extrapolated our results to find the ring limit upper bound curve for noticeable close encounters between Jupiter and Chariklo. We found that if velocity effects were included, then 19 out of 20

published d_{min} values were smaller than their corresponding ring limit values on the curve as expected.

Using the second method, we found maximum ring limit values for close encounters between Chariklo and each giant planet over the range $0 \leq v_\infty \leq 9$ km/s and set the ring limit equal to each value for each planet. Then we compared these ring limit values to previously published d_{min} values for close encounters between Chariklo and Jupiter, Saturn and Uranus (there were no published values for Neptune).

The results were $R = 3.5$ R_{td} for Jupiter, $R = 3.9$ R_{td} for Saturn, $R = 4.4$ R_{td} for Uranus and $R = 4.4$ R_{td} for Neptune. With this second method, we found that all 27 previously published close encounter distances lay within their respective ring limit in agreement with our results.

Our improved determination of the ring limit using this method showed that the ring limit was far below our initial estimate of 10 tidal disruption distances for every planet. This makes moderate close encounters less likely than the frequencies found using our previous close encounter severity scale on integrations of Chariklo and Chiron.

Finally, we set the ring limit equal to a constant value of the ring limit lower bound of 1.8 tidal disruption distances. We found that with this method only 11 of the previously reported 27 noticeable close encounters would be classified as noticeable.

An analytical solution for the ring limit could be found only for parabolic orbits and special cases for hyperbolic orbits. In general, the ring limit increased with the ring orbital radius as a power law but decreased with the mass of the small body as a power law. No single relationship between the ring limit and velocity at infinity of the small body could be found.

5.4   The Future

There are major questions which are in need of answering for this very young field. Are rings around small bodies commonplace or rare? How stable are rings around small bodies? Do shepherd moons exist around Chariklo? Were all small body rings created in the same way or were multiple ring creation scenarios responsible?

It is hoped that this pioneering work has laid a foundation for the study of any rings that are found around small bodies in the future by demonstrating practical techniques, providing a severity scale for close encounters and providing data which can be extrapolated to determine ring limits for close encounters between giant planets and other ringed small bodies. Our own work here itself could be built upon by simulating close encounters for small bodies outside the mass range used in this work. It our hope that future research will corroborate our results. Our work may also have applications in other fields such as the study of circumstellar disks and planetary systems which have encounters with other stars.

Our knowledge in this field could grow significantly with an increase in the number of probe missions to small bodies. A probe mission to Chariklo could

determine if it has shepherd moons to help stabilize its rings as has been proposed (El Moutamid et al., 2014; Ortiz et al., 2015). It could also help determine if the gap between Chariklo's rings is caused by a moon in the gap, outside the gap, or by neither of these. If it is the former, then the gap would be formed in the same way that the moon Pan helps create Saturn's Encke gap (Porco et al., 2005).

If the latter, then a moon outside the gap would exist in an orbit in a mean motion resonance with a radial location inside the gap. In this scenario, the gap would have been created by sculpting. Of course the gap could be caused by neither of these mechanisms. A probe mission to Chiron could finally determine conclusively if the detected circum-nuclear material around this body is a ring, an arc, jets or something else entirely.

Now that we know that Haumea is the only known ringed dwarf planet with moons and is a member of a collisional family, this makes it an object of interest. And space probes are just now beginning to visit the Trans-Neptunian region. The New Horizons Space Probe[16] has visited the Trans-Neptunian Object Pluto and is set to rendezvous with the TNO (486958) 2014 MU69 in 2019. This author proposes that Haumea be selected as the next TNO to be visited by a probe.

Innovations by the SpaceX company are making probe missions more affordable. The company recently launched a car into space and demonstrated again the reusability of its booster rockets.

As costs go down, missions to the outer Solar system will become more affordable, which should lead to a significant enhancement of our knowledge of small bodies. Already, history is being made as the Dawn mission[17] uncovers secrets of Vesta and Ceres. And the future Lucy mission[18] will be the first space mission ever to Jupiter's Trojan asteroids.

Ground work will still play a significant role in the advancement of the field in two ways: observations and computer simulations. As the results from the Gaia space probe[19] are revealed, the location of stars in our galaxy will become better known. This will reduce the uncertainty in the paths that shadows take across the Earth during an occultation event. This in turn may lead to more observations of stellar occultations and to the discovery of more ringed small bodies.

Thus, we may be on the verge of tremendous growth in this field. In fact, given that the number of Centaurs with diameters larger than 1 km is believed to exceed 44,000, there could exist a large undiscovered population of ringed Centaurs (Horner et al., 2004).

A reanalysis of the close encounters of the clones of Chariklo and Chiron using our improved close encounter severity scale is of interest. For Chariklo and Chiron, the boundary separating close encounters of low severity from close

---

[16]https://www.nasa.gov/mission_pages/newhorizons/main/index.html (accessed January 18, 2018)

[17]https://dawn.jpl.nasa.gov/ (accessed February 8, 2018)

[18]https://www.nasa.gov/content/goddard/lucy-the-first-mission-to-jupiter-s-trojans (accessed February 8, 2018)

[19]http://sci.esa.int/gaia/ (accessed January 18, 2018)

encounters of moderate severity has changed. A reanalysis would yield a more accurate count of the moderate and low severity close encounters.

More integrations of Chariklo and Chiron should be carried out to study ring stability. Of interest is whether or not rings can remain stable over time frames comparable to their Centaur lifetime. These integrations should involve the small body and a ring structure both with and without shepherd moons.

Also, integrations of initially non-circular rings could be done to determine a time frame within which stabilizing factors such as shepherd moons and self-gravitating rings can heal the damage done to the ring structure. Once this is known, our own integrations of Chariklo and Chiron could be reanalysed using our improved close encounter severity scale to determine likely time intervals between moderate or higher close encounters. Of interest is whether or not the rings can heal themselves via shepherd moons (El Moutamid et al., 2014) or self-gravitating rings (Rimlinger et al., 2017) before another destructive encounter occurs.

Integrations of actual collisions between small bodies could also be simulated using smooth particle hydrodynamics (Canup, 2005; Benz et al., 2008) to study ring formation. These would involve collisions with the small body itself with bodies of various masses and collisions between satellites about the small body. Admittedly, these integrations would be time intensive given the large number of separate particles involved.

Integrations of possible formation scenarios of the Haumea system including its ring are also of interest. The exact ring formation mechanism is far from clear. Haumea is a member of the only known Tran-Neptunian collisional family, but this does not necessarily mean that its rings were formed by a collision. Especially since the ring also lies within Haumea's Roche limit (Ortiz et al., 2017).

It is also interesting that the orbital radius of the ring around Haumea is an order of magnitude larger than those of Chariklo or Chiron. Though Haumea currently does not cross the orbit of any planet, the possibility that Haumea has crossed the orbits of planets in the past cannot be excluded.

The larger members of the Trojan populations of Jupiter and Neptune should also be checked for rings. This need not involve a probe necessarily but instead could be conducted using stellar occultations. Also, integrations of potential ring-bearing Trojans would make an interesting study.

Then the effect of other asteroids on rings could be studied. This is especially true in the Jupiter Trojan region where significantly more asteroids have been discovered. Though many thousands of Neptune Trojans could remain undiscovered (Sheppard & Trujillo, 2006; Lykawka et al., 2011).

For Jupiter Trojans, possible candidates include 624 Hektor, 911 Agamemnon, and 1437 Diomedes which have diameters comparable to those of Chariklo and Chiron[20]. For Neptune Trojans, possible candidates include 2001 QR322, 2011 HM102, 2006 RJ103, 2007 VL305, (316179) 2010 EN65, 2011 WG157, and 2013 KY18.

---

[20]https://ssd.jpl.nasa.gov/sbdb.cgi (accessed Feb. 5, 2018)

Whether by ground or space mission, our knowledge of ringed small bodies is sure to increase. As our knowledge of this young field grows, many more ringed small bodies may be found. One day, their number may rival that of the currently known Centaurs themselves. Then, perhaps questions involving the nature and origin of the rings will be answered.

The following references are for the first and last chapters only.

References

Altenhoff, W. J., Menten, K. M., & Bertoldi, F. 2001, A&A, 366, L9

Altwegg, K., Balsiger, H., Bar-Nun, A., Berthelier, J. J., Bieler, A., Bochsler, P., Briois, C., Calmonte, U., Combi, M., De Keyser, J., Eberhardt, P., Fiethe, B., Fuselier, S., Gasc, S., Gombosi, T. I., Hansen, K. C., Hässig, M., Jäckel, A., Kopp, E., Korth, A., LeRoy, L., Mall, U., Marty, B., Mousis, O., Neefs, E., Owen, T., Rème, H., Rubin, M., Sémon, T., Tzou, C.-Y., Waite, H., & Wurz, P. 2015, Science, 347, article id. 1261952

Araujo, R. A. N., Sfair, R., & Winter, O. C. 2016, ApJ, 824, article id. 80

Aron, J. 2013, New Scientist, 216(2911), 6

Bailey, B. L., & Malhotra, R. 2009, Icarus, 203, 155

Bate, R. R., Mueller, D. D., & White, J. E. 1971, Fundamentals of astrodynamics., by Bate, R. R.; Mueller, D. D.; White, J. E.. New York, NY (USA): Dover Publications, 12 + 455 p.,

Batygin, K., & Morbidelli, A. 2017, AJ, 154, 229

Bennett, Jeffrey O., Donahue, Megan O., Schneider, Nicholas, & Voit, Mark 2016, The Cosmic Perspective 8th ed. (Pearson College Division)

Benz, W., Anic, A., Horner, J., & Whitby, J. A. 2008, Mercury, Space Sciences Series of ISSI, Volume 26. ISBN 978-0-387-77538-8. Springer Science+Business Media, BV, 2008, p. 7, 7

Binzel, R. P. 2006, Minor Planet Bulletin, 33, 106

Braga-Ribas, F., Sicardy, B., Ortiz, J.∼L., et al. 2014, Nature, 508, 72

Brasser, R., Schwamb, M. E., Lykawka, P. S., & Gomes, R. S. 2012, MNRAS, 420, 3396

Brown, M. E. 2017, AAS/Division for Planetary Sciences Meeting Abstracts, 49, 405.06

Burbine, Thomas, H. 2017, Asteroids: Astronomical and Geological Bodies (Cambridge)

Burns, J. A., Showalter, M. R., Hamilton, D. P., et al. 1999, Science, 284, 1146

Bus, S. J., A'Hearn, M. F., Bowell, E., & Stern, S. A. 2001, Icarus, 150, 94

Bus, S. J., A'Hearn, M. F., Schleicher, D. G., & Bowell, E. 1991, Science, 251, 774

Bus, S. J., Bowell, E., & French, L. M. 1988, IAUC, 4684, 2

Bus, S. J., Bowell, E., Harris, A. W., & Hewitt, A. V. 1989, Icarus, 77, 223

Bus, S. J., Buie, M. W., Schleicher, D. G., et al. 1996, Icarus, 123, 478

Canup, R. M. 2005, Science, 307, 546

Capria, M. T., Coradini, A., De Sanctis, M. C., & Orosei, R. 2000, AJ, 119, 3112

Chambers, J. E. 1999, MNRAS, 304, 793

Cincotta, P. M., Giordano, C. M., & Simó, C. 2003, Physica D Nonlinear Phenomena, 182, 151

Cincotta, P. M., & Simó, C. 2000, A&A, 147, 205

Connors, M., Wiegert, P., & Veillet, C. 2011, Nature, 475, 481

Davies, J. K., & Barrera, L. H. 2004, The first decadal review of the Edgeworth-Kuiper Belt, edited by J.K. Davies and L.H. Barrera. Dordrecht: Kluwer Academic Publishers, 2004 Reprinted from: Earth, Moon, and Planets, vol. 92, nos. 1-4, 2003.,

de la Fuente Marcos, C., & de la Fuente Marcos, R. 2014, Ap&SS, 352, 409

de la Fuente Marcos, C. & de la Fuente Marcos, R. 2014, MNRAS, 439, 2970.

Di Sisto, R. P., & Brunini, A. 2007, Icarus, 190, 224

Dones, L., Brasser, R., Kaib, N., & Rickman, H. 2015, Space Sci. Rev., 197, 191

Dones, L., Levison, H. F., & Duncan, M. 1996, Completing the Inventory of the Solar System, 107, 233

Duffard, R., Lazzaro, D., Pinto, S., et al. 2002, Icarus, 160, 44

Duncan, M. J., Levison, H. F., & Budd, S. M. 1995, AJ, 110, 3073

Duncan, M., Levison, H., & Dones, L. 2004, Comets II, 193

Duncan, M., Quinn, T., & Tremaine, S. 1987, AJ, 94, 1330

Duncan, M., Quinn, T., & Tremaine, S. 1988, ApJL, 328, L69

Elliot, J. L., Olkin, C. B., Dunham, E. W., et al. 1995, Nature, 373, 46

Ellis, K. M., & Murray, C. D. 2000, Icarus, 147, 129

El Moutamid, Maryame, Kral, Quentin, Sicardy, Bruno, Charnoz, Sebastien, Roques, Françoise, Nicholson, Philip D., & Burns, Joseph A. 2014, American Astronomical Society, DDA meeting #45, #402.05

Emel'yanenko, V. V., Asher, D. J., & Bailey, M. E. 2005, MNRAS, 361, 1345

Emel'yanenko, V. V., Asher, D. J., & Bailey, M. E. 2013, Earth Moon and Planets, 110, 105

Festou, M. C., Keller, H. U., & Weaver, H. A. 2004, Comets II,

Fornasier, S., Lazzaro, D., Alvarez-Candal, A., et al. 2014, A&A, 568, L11

Fornasier, S., Lellouch, E., Müller, T., et al. 2013, A&A, 555, A15

Fouchard, M., Rickman, H., Froeschlé, C., & Valsecchi, G. B. 2014,Icarus, 231, 110

Fraknoi, Andrew, Morrison, David, & Wolff, Sidney, C. 2016, Astronomy (Open-Stax)

French, R. G., McGhee, C. A., Dones, L., & Lissauer, J. J. 2003, Icarus, 162, 143

French, R. G., Nicholson, P. D., McGhee-French, C. A., et al. 2016, Icarus, 274, 131

Froeschle, C., & Morbidelli, A. 1994, Asteroids, Comets, Meteors 1993, 160, 189

Froeschle, C., & Scholl, H. 1986, A&A, 166, 326

Froeschle, C., & Scholl, H. 1989, Celestial Mechanics and Dynamical Astronomy, 46, 231

Gallardo, T. 2006, Icarus, 184, 29

Giordano, C. M., & Cincotta, P. M. 2004, A&A, 423, 745

Gleik, J. 1987, Chaos : Making a New Science (Penguin Publishing Group)

Gomes, R., Levison, H. F., Tsiganis, K., & Morbidelli, A. 2005, Nature, 435, 466

Gough, D. O. 1994, MNRAS, 269, L17

Goździewski, K., Bois, E., Maciejewski, A. J., & Kiseleva-Eggleton, L. 2001, A&A, 378, 569

Groussin, O., Lamy, P., & Jorda, L. 2004, A&A, 413, 1163

Gurfil, Pini, Seidelmann, Kenneth, P. 2016, Celestial Mechanics and Astrodynamics: Theory and Practice (Springer)

Guzzo, M. 2006, Icarus, 181, 475

Hahn, G., & Bailey, M. E. 1990, NATURE, 348, 132

Hairer, Ernst, Nørsett, Syvert P., & Wanner, Gerhard 1993, Solving Ordinary Differential Equations I, Vol. 8, (Springer)

Harris, W. M., Ballester, G. E., Barker, J., et al. 1994, Bulletin of the American Astronomical Society, 26, 05.26

Hartmann, W. K., Tholen, D. J., Cruikshank, D. P., Brown, R. H., & Morrison, D. 1988, BAAS, 20, 836

Hartmann, W. K., Tholen, D. J., Meech, K. J., & Cruikshank, D. P. 1990, Icarus, 83, 1

Hedman, M. M., Burns, J. A., Tiscareno, M. S., et al. 2007, Science, 317, 653

Heisler, J., & Tremaine, S. 1986, Icarus, 65, 13

Hill, G. W. 1878, Am. J. Math, 1, 5

Hills, J. G. 1981, AJ, 86, 1730

Hinse, T. C., Christou, A. A., Alvarellos, J. L. A., & Goździewski, K. 2010, MNRAS, 404, 837

Holman, M. J., & Wisdom, J. 1993, AJ, 105, 1987

Horner, J., Evans, N. W., & Bailey, M. E. 2004, MNRAS, 354, 798

Horner, J., Evans, N. W., & Bailey, M. E. 2004, MNRAS, 355, 321

Horner, J., Evans, N. W., Bailey, M. E., & Asher, D. J. 2003, MNRAS, 343, 1057

Horner, J., & Jones, B. W. 2010, Astronomy and Geophysics, 51, 6.16

Horner, J., & Lykawka, P. S. 2010, MNRAS, 402, 13

Horner, J. & Wyn Evans, N. 2006, MNRAS, 367, L20.

Hyodo, Ryuki, Charnoz, Sébastien, Genda, Hidenori, & Ohtsuki, Keiji 2016, ApJL, 828, L8

Jang-Condell, H. 2017, APJ, 835, 12

Jessup, K. L., Clarke, J. T., Ballester, G. E., & Hammel, H. B. 2000, Icarus, 146, 19

Jewitt, David 2009, AJ, 137, 4296

Jewitt, D., & Luu, J. 1996, Completing the Inventory of the Solar System, 107, 255

Kirkwood D., 1867, Meteoric Astronomy. J. B. Lippincott, Philadelphia

Kowal, C. T., Liller, W., & Marsden, B. G. 1979, Dynamics of the Solar System, 81, 245

Kozai, Y. 1962, AJ, 67, 591

Laskar, J., & Boué, G. 2010, A&A, 522, A60

Lacerda, P., Jewitt, D., & Peixinho, N. 2008, Asteroids, Comets, Meteors 2008, 1405, 8007

Lazzaro, D., Florczak, M. A., Angeli, C. A., et al. 1997, Planet. Space Sci., 45, 1607

Lazzaro, D., Florczak, M. A., Betzler, A., et al. 1996, Planet. Space Sci., 44, 1547

Lellouch, E., Kiss, C., Santos-Sanz, P., et al. 2010, A&A, 518, L147

Levison, H. F. 1996, Completing the Inventory of the Solar System, 107, 173

Levison, H. F., & Duncan, M. J. 1993, ApJL, 406, L35

Levison, H. F., & Duncan, M. J. 1994, Icarus, 108, 18

Levison, H. F., & Duncan, M. J. 1997, Icarus, 127, 13

Levison, H. F., Duncan, M. J., Dones, L., & Gladman, B. J. 2006, Icarus, 184, 619

Lockwood, A. C., Brown, M. E., & Stansberry, J. 2014, Earth Moon and Planets, 111, 127

Loders, Katharina, & Fegley, Bruce 1998, Jupiter, Rings and Satellites. The Planetary Scientist's Companion (Oxford University Press)

Luu, J. X. 1993, PASP, 105, 946

Luu, J. X., & Jewitt, D. C. 1990, AJ, 100, 913

Lykawka, P. S., Horner, J., Jones, B. W., & Mukai, T. 2011, MNRAS, 412, 537

Lykawka, P. S., & Mukai, T. 2007, Icarus, 189, 213

Malhotra, R. 1994, Physica D Nonlinear Phenomena, 77, 289

Marquis de Laplace, P.-S. 1799, Traité de mécanique céleste (Paris: Duprat)

Marzari, F. & Scholl, H. 2000, Icarus, 146, 232.

Marzari, F., & Scholl, H. 2002, Icarus, 159, 328

Marzari, F., Tricarico, P. & Scholl, H. 2002, APJ, 579, 905.

Masaki, Y., Kitasato, Tsukuba, & Kinoshita, H. 2003,A&A, 403, 769

Meech, K. J., & Belton, M. J. S. 1990, AJ, 100, 1323

Meech, K. J., Buie, M. W., Samarasinha, N. H., Mueller, B. E. A., & Belton, M. J. S. 1997, AJ, 113, 844

Meech, K. J., & Svoren, J. 2004, Comets II, 317

Melita, M. D., Duffard, R., Ortiz, J. L., & Campo-Bagatin, A. 2017, A&A, 602, A27

Michikoshi, S., & Kokubo, E. 2017, ApJL, 837, L13

Moons, M., & Morbidelli, A. 1995, Icarus, 114, 33

Moons, M., Morbidelli, A., & Migliorini, F. 1998, Icarus, 135, 458

Murdin, P. 2000, Encyclopedia of Astronomy and Astrophysics, 5403

Murray, C.D., & Dermott, S. F. 1999, Solar system Dynamics (Cambridge University Press)

Murray-Clay, R. A., & Schlichting, H. E. 2011, ApJ, 730, 132

Napier, B., Asher, D., Bailey, M., & Steel, D. 2015, Astronomy and Geophysics, 56, 6.24

Nesvorný, D., & Dones, L. 2002, Icarus, 160, 271

Norton, O. R., & Chitwood, L. A. 2008, Field Guide to Meteors and Meteorites: , Patrick Moore's Practical Astronomy Series. (London: Springer-Verlag)

Oort, J. H. 1950, Bulletin of the Astronomical Institutes of the Netherlands, 11, 91

Ortiz, J. L., Duffard, R., Pinilla-Alonso, N., et al. 2015, Ap&SS, 576, A18

Ortiz, J. L., Santos-Sanz, P., Sicardy, B., et al. 2017, Nature, 550, 219

Pan, Margaret, & Wu, Yanqin 2016, AJ, 821, article id. 18

Perna, D., Dotto, E., Barucci, M. A., et al. 2009, A&A, 508, 451

Petit, J.-M., Morbidelli, A., & Chambers, J. 2001, Icarus, 153, 338

Philpott, C. M., Hamilton, D. P., & Agnor, C. B. 2010, Icarus, 208, 824

Planetary Laboratory, Purple Mountain Observatory, & Stellar Division of Peking Observatory 1978, Chinese Astronomy, 2, 341

Poincaré, H. 1902, BuAsI, 19, 289

Porco, C. C., Baker, E., Barbara, J., et al. 2005, Science, 307, 1226

Prialnik, D., Brosch, N., & Ianovici, D. 1995, MNRAS, 276, 1148

Quinn, T., Tremaine, S., & Duncan, M. 1990, ApJ, 355, 667

Rabinowitz, D. L., Barkume, K., Brown, M. E., et al. 2006, ApJ, 639, 1238

Rein, H., & Spiegel, D. S. 2015, MNRAS, 446, 1424

Rein, H., & Tamayo, D. 2015, MNRAS, 452, 376

Rimlinger, T., Hamilton, D. P., & Hahn, J. M. 2017, AAS/Division for Planetary Sciences Meeting Abstracts, 49, 501.03

Roche, E. 1849, Acad'emie des Sciences de Montpellier:M'emoires de la Section-des Sciences, 1, 243

Roig, F., Nesvorný, D., & Ferraz-Mello, S. 2002, MNRAS, 335, 417

Ryden, Barbara, S. 2016, Dynamics (The Ohio State University)

Scholl, H., Marzari, F., & Tricarico, P. 2005, Icarus, 175, 397

Schubart, J. 2007, Icarus, 188, 189

Serway, Raymond A., Faughn, Jerry S., Vuille, Chris, & Bennett, Charles A. 2006, College Physics (Thompson)

Sheppard, S. S., & Trujillo, C. A. 2006, Science, 313, 511

Shevchenko, Ivan, I. 2017, The Lidov-Kozai Effect - Applications in Exoplanet Research and Dynamical Astronomy (Springer International Publishing)

Sie, Z.-F., Lin, H.-W., & Ip, W.-H. 2015, AAS/Division for Planetary Sciences Meeting Abstracts #47, 47, 211.10

Silva, A. M., & Cellone, S. A. 2001, Planet. Space Sci., 49, 1325

Smirnov, E. A., & Shevchenko, I. I. 2013, Icarus, 222, 220

Soter, S. 2007, Scientific American, 296,

Spahn, F., Petit, J.-M., & Bendjoya, P. 1993, Celestial Mechanics and Dynamical Astronomy, 57, 391

Stern, S. A. 1989, PASP, 101, 126

Stern, S. A. 1995, S&T, 89, 32

Sykes, M. V., & Walker, R. G. 1991, Science, 251, 777

Thirouin, A., Sheppard, S. S., Noll, K. S., et al. 2016, AJ, 151, 148

Tiscareno, M. S., & Malhotra, R. 2003, AJ, 126, 3122

Tiscareno, M. S., & Malhotra, R. 2009, AJ, 138, 827

Volk, K., & Malhotra, R. 2008, ApJ, 687, 714-725

Weaver, H. A., & Lamy, P. L. 1997, Earth Moon and Planets, 79, 17

Wisdom, J. 1982, AJ, 87, 577

Whipple, A. L. 1995, Icarus, 115, 347

Wie, Bong 1998, Space Vehicle Dynamics and Control (AIAA)

Williams, J.G. 1969, Ph.D. dissertation,University of California, Los Angeles.

Wisdom, J. 1982, AJ, 87, 577

Wisdom, J. 1983, Icarus, 56, 51

Womack, M., & Stern, S. A. 1995, BAAS, 27, 33.07

Wood, J., Horner, J., Hinse, T. C., & Marsden, S. C. 2017, AJ, 153, 245

Wood, J., Horner, J., Hinse, T. C., & Marsden, S. C. 2018, AJ, 155, 2

Zeilik, Michael 2002, Astronomy: The Evolving Universe, 9th Edition (Cambridge University Press)